Design of Anode Catalyst-Ionomer Interfaces for Durable Anion-Exchange-Membrane Water Electrolyzers

by

Minkyoung Kwak

A dissertation accepted and approved in partial fulfillment of the

requirements for the degree of

Doctor of Philosophy

in Chemistry

Dissertation Committee:

David C. Johnson, Chair

Shannon W. Boettcher, Advisor

Carl K. Brozek, Core Member

Paul A. Kempler, Core Member

Paul D. Dalton, Institutional Representative

University of Oregon

Spring 2025

DISSERTATION ABSTRACT

Minkyoung Kwak

Doctor of Philosophy in Chemistry

Title: Design of Anode Catalyst-Ionomer Interfaces for Durable Anion-Exchange-Membrane Water Electrolyzers

Green hydrogen is a crucial energy source for sustainable society. Developing efficient and durable anion-exchange membrane water electrolyzers (AEMWEs) that operate with pure water is important to avoid the use of expensive precious metal group catalysts employed for proton-exchange-membrane water electrolyzers (PEWWEs) and to mitigate problems associated with supporting electrolytes that are used in alkaline water electrolyzers (AWEs) such as component corrosion and shunt currents through manifolds. However, the poor durability of anion-exchange-ionomers and membranes limits the advancement of this technology to meet commercialization standards.

To improve the durability of AEMWEs system, Chapter II provides simplified anode catalyst-ionomer interfaces as a model system to understand how catalyst layers interact with overlaid ionomers in constructed porous electrodes and how this interaction affects the electrochemical responses of AEMWE devices. This work investigates Co-based self-supported anodes, nanostructured catalyst layers directly grown on porous transport layers via a hydrothermal method, as opposed to conventional nanoparticle ink-based anodes. In Chapter III, passivated anode architectures are introduced with alkaline-stable, electronically insulating coatings at anode catalyst-ionomer interfaces. Those coatings, fabricated with an atomic layer deposition technique (ALD), effectively suppress electrochemical oxidation of ionomers in the anodes. Building on Chapter II and III, in Chapter IV, we further develop passivating coatings using a molecular layer deposition

(MLD) method to precisely tune the interfacial reactions at anodes, enhancing anode durability without significantly sacrificing the device performance.

These findings provide design principles for next-generation AEMWE anodes, emphasizing the interplay between porous electrode structures, ionomer incorporation, and passivation coatings. Understanding and engineering how passivation coatings modulate interfacial reactions will provide key insights for improving the performance and durability of AEMWEs with pure water feed. These advancements enable AEMWE technology to be closer to meeting commercialization standards and can be applied to other electrochemical devices.

This dissertation includes previously published and unpublished co-authored materials.

CURRICULUM VITAE

NAME OF AUTHOR: Minkyoung Kwak

GRADUATE AND UNDERGRADUATE SCHOOLS ATTENDED:

University of Oregon, Eugene
Yonsei University, Seoul, South Korea

DEGREES AWARDED:

Doctor of Philosophy, Chemistry, 2025, University of Oregon
Bachelor of Science, Chemistry, 2017, Yonsei University

AREAS OF SPECIAL INTEREST:

Membrane Electrolyzer Devices; Oxygen Evolution Reaction Catalysis, Interfacial Engineering

PROFESSIONAL EXPERIENCE:

Visiting Student Researcher, University of California, Berkeley, 2024 - 2025

Research Assistant, University of Oregon, 2020 - 2025

Teaching Assistant, University of Oregon, 2020 - 2024

Intern, Korea Institute of Science and Technology, 2018 - 2020

PUBLICATIONS:

Muhyuddin, M.; Santoro, C.; Osmieri, L.; Ficca, V. C. A.; Friedman, A.; Yassin, K.; Pagot, G.; Negro, E.; Konovalova, A.; Lindquist, G.; Twight, L.; **Kwak, M**.; Berretti, E.; Di Noto, V.; Jaouen, F.; Elbaz, L.; Dekel, D.; Mustarelli, P.; Boettcher, S. W.; Lavacchi, A.; Atanassov, P. Anion-Exchange-Membrane Electrolysis with Alkali-Free Water Feed. *Submitted, Chem. Rev.*

Hou, S.; Sekar, A.; Zhao, Y.; **Kwak, M**.; Oh, J.; Li, K. K.; Wu, P.; Hannagan, R. T.; Cartagena, V.; Ekennia, A. C.; Zachman, M. J.; Frechette, J.; Su, G. M.; Lakshmanan, B.; Jaramillo, T. F. and Boettcher, S. W. Durable, Pure Water Fed, Anion Exchange Membrane Electrolyzers through Interphase Engineering. *Submitted, Sci.*

Konovalova, A.; Goldman, A.; Shekhar, R.; Triplett, I.; Moutarlier, L.; **Kwak, M**.; Kempler, P. Pathways to Electrochemical Ironmaking at Scale Via the Direct Reduction of Fe_2O_3. *ACS Energy Lett*. **2025**, 10 (4), 1851-1857.

Zhai, T.; Wang, H.; Beaudoin, S.; Zhang, R.; **Kwak, M**.; Hou, S.; Guo, Z. and Boettcher, S. W. Perovskite Catalysts for Pure-Water-Fed Anion-Exchange-Membrane Electrolyzer Anodes: Co-Design of Electrically Conductive Nanoparticle Cores and Active Surfaces. *Accepted, J. Am. Chem. Soc.* **2025**.

Sarma, P. V.; Krama, B. V.; Chen, L.; Sasmal, S.; Weingartz, N. P.; Huang, J.; Mitchell, J. B.; **Kwak, M**.; Chen, L. X. and Boettcher, S. W. Local Electric Field Effects on Water Dissociation in Bipolar Membranes Studied Using Core–Shell Catalysts. *Chem. Mater*. **2024**, *36* (24), 11863-11872.

Kwak, M.; Ojha, K.; Shen, M.; Boettcher, S. W. Electrically Insulated Catalyst–Ionomer Anode Interfaces toward Durable Alkaline Membrane Electrolyzers. *ACS Energy Lett*. **2024**, *9* (3), 1025-1034.

ACKNOWLEDGMENTS

This work was supported by the U.S. Department of Energy's Office of Energy Efficiency and Renewable Energy (EERE) under the Fuel Cell Technologies Office (FCTO) under award DE-EE0008841 and by De Nora Tech, LLC. The work was conducted using shared instrumentation in the Center for Advanced Materials Characterization in Oregon (CAMCOR).

I express my sincere thanks to my advisor, Prof. Shannon W. Boettcher, for giving me the opportunity to learn various perspectives of electrochemistry and for advising my graduate studies. I learned a lot from his passionate scientific communication in the field, which inspired me to be an effective scientist. I would like to express my thanks to my committee members, including my advisor, Shannon, Prof. David C. Johnson, Prof. Carl K. Brozek, Prof. Paul A. Kempler, and Prof. Paul D. Dalton. I deeply appreciate their guidance and support throughout the years. Special thanks to Prof. Paul A. Kempler for teaching me electrochemical knowledge and techniques in an encouraging environment early in my PhD through the Oregon Center for Electrochemistry courses.

I am grateful to all of the Boettcher lab members for helping me acquire skills necessary to achieve a successful academic and personal life. Special thanks to Grace Lindquist and Raina Krivina for building the foundations of AEM work within the lab, enabling a quick start to my dissertation work, as well as for their great mentorship. Thanks to Kasinath Ojha, Shujin Hou, Tingting Zhai, and Anthony Ekennia for working together in the AEM team for many years, sharing lots of exciting results. To Ana Konovalova, Prasad Sarma, Meikun Shen, Jiawei Huang, James Mitchell, Sayantan Sasmal, Liam Twight, Lihaokun Chen, Aaron Kaufman, Kira Thurman, Olivia Traenkle, Nick D’Antona, Yang Zhao, Nicole Saguì, Manasa Rajeev, Raj Shekhar, and Felice Gallegos – thank you for your help, support, discussions, and the times we worked together

in the lab, as well as friendship. I am grateful to Arun Chakraborty, Andrew Pendergast, Gwan Hyun Choi, Emma Kaeli, Yuta Inoue, Wenbo Zhang, Jin Wook Yang, Dong Su Kim, Jeonghoon Lim, Duha Syar, Yifan Wu, Ethan Ng Shi, Catherine Wallace, Jihan Zhang, Yiwen Sun, Rika Sato, Nathan Stovall, Kelvin Li, Yunseok Kang, Bernard Wang, and Nikhil Jagota for their help and support my time at UC Berkeley.

I appreciate the collaborators who provided inspiring discussions and shared their knowledge, including Sharmistha Bhattacharjee, Ryan Hannagan, Luis Hagner, and Lara-Pauline.

I would like to express my great appreciation to the CAMCOR staff, especially Stephen Golledge, Jacqui Beran, Fuding Lin, Valerie Brogden, and Kurt Langworthy, for their assistance with materials characterization, and UO machine shop staff, Julian McAdams. I thank Finn Babbe at Lawrence Berkeley National Laboratory for training me on instrumentation. I also thank the UO Chemistry department staff, Christi Mabinuori, Helen Durany, Leah O'Brien, Janet Kneller, Laurie Schneider, Carissa Bosch, and the UCB staff, Nathalie Grogan, Jeff King, and others.

I appreciate my mentors, former colleagues, and friends in South Korea who have supported me since I first planned study abroad for my doctorate studies. I am grateful to Prof. Jinwoo Cheon and his lab at Yonsei University, getting me interested in scientific research and equipping me with essential lab skills. I extend special thanks to Prof. Youngsoo Kim, Prof. Hyun Seo Ahn, and Prof. Dongwon Yoo. I also appreciate the X-ray open lab team at Korea Institute of Science and Technology, including Dr. Sung Ok Won, for giving me opportunities to learn and explore X-ray techniques.

I appreciate my boyfriend, Kieran Spence, for sharing many fun memories over the years and supporting my personal and academic life in the U.S. Lastly, I deeply appreciate my family for supporting me in countless ways throughout my studies abroad in the U.S.

TABLE OF CONTENTS

LIST OF FIGURES

LIST OF TABLES

CHAPTER I

INTRODUCTION

Unpublished material written by myself.

For sustainable hydrogen production with green electricity, membrane water electrolyzer technologies have been developed. The two leading technologies are proton-exchange-membrane water electrolyzers (PEMWEs) and alkaline water electrolyzers (AWEs). The former uses a zero-gap configuration, precious group metal (PGM) catalysts to construct efficient and stable electrodes, perfluorosulfonic acid (PFSA) containing Nafion^{TM} membranes, and operates efficiently (1.7 – 1.8 V at 2 A cm^{-2}).[1-4] However, the reliance on scarce and expensive Ir-based oxygen-evolving catalysts at the anode could limit the technologies feasibility at large-scale (gigawatt level).[5,6] On the other hand, AWE systems allow for the use of cheaper and earth-abundant non-PGM-based catalysts. However, they require high-concentration and temperature KOH supporting electrolyte to reduce ohmic resistances, which necessitates the development of corrosion-resistant cell components and additional stack-level modifications to minimize shunt currents and improve tolerance to start-stop operation.[7-9]

As an alternative technology, anion-exchange-membrane water electrolyzers (AEMWEs) leverage benefits of both PEMWE and AWE, featuring a zero-gap cell assembly with pure water feed, and cost-effective catalysts and cell components.[10] Critical components in the AEMWE system include the AEM: a hydroxide conducting polymer which is sandwiched between the

electrodes to conduct OH^-, limits gas-crossover, and prevents short-circuiting, and the anion-exchange-ionomer (AEI): a dispersible version of the AEM which is integrated into the electrodes to ensure a high-degree of catalyst utilization. However, there are no ionomers and membranes that can withstand the alkaline environment and high oxidative potential near the anode catalyst.[11] This instability is especially critical when AEMWE devices are operated with in pure water feed because the ionomer is the sole source of ion transport.[12,13]

Despite significant work to develop efficient and durable catalysts, ionomers, and membranes for AEMWEs, durability remains as a major bottleneck preventing commercialization. Development and optimization have been carried out for these components individually, and there is a lack of dedicated research on catalyst-ionomer/membrane interactions, which is crucial for advancing AEMWE. Furthermore, most studies on the catalyst-ionomer interface have been conducted using nanoparticle (NP) ink-based electrodes,[14-17] which have complicated interfacial structures and make it challenging to understand the electronic and ionic processes driving gas evolution reactions in porous electrodes.

On the other hand, encapsulating active catalyst materials with functional metal oxide coatings has been widely adopted in electrochemical devices to prevent detrimental side reactions while maintaining desired electrochemical activities.[18-21] These surface passivation layers could be applied in AEMWE devices to suppress unavoidable ionomer oxidation, thereby enhancing durability without significantly compromising the device performance.

In this perspective, this dissertation aims to develop and provide a model anode design with a simplified anode catalyst-ionomer interface, further allowing for the incorporation of passivation coatings to enhance the lifetime of anodes. Various parameters of passivation coatings are screened and explored to modulate anodic interfacial reactions. Chapter II provides fundamental

understandings of microstructures of self-supported porous electrodes and examines the correlation between anode catalyst-ionomer interfacial structures and water oxidation kinetics in comparison with conventional NP ink-based anodes. Chapter III demonstrates passivated anodes, showing that deposition of nanoscale HfO_x thin films at anode catalyst-ionomer interfaces suppress ionomer oxidation in both Ir- and CoO_x-based anodes. Chapter IV further develops passivated anodes using molecular layer deposition to enhance ion-permeability and film flexibility as additional functionalities of passivation coatings.

Chapter I and V contain unpublished material written by myself. Chapter II is a co-authored unpublished work with Hou. S; Spence, K. J.; Debela, T.; and Boettcher, S. W. Chapter III is published as **Kwak, M**.; Ojha, K.; Shen, M.; and Boettcher, S. W. Electrically Insulated Catalyst–Ionomer Anode Interfaces toward Durable Alkaline Membrane Electrolyzers. ACS Energy Lett. 2024, *9* (3), 1025-1034. Chapter IV is a co-authored unpublished work with Bhattacharjee, S.; Strandwitz, N.; and Boettcher, S. W.

REFERENCES

(1) Ayers, K. E.; Anderson, E. B.; Capuano, C.; Carter, B.; Dalton, L.; Hanlon, G.; Manco, J.; Niedzwiecki, M. Research Advances towards Low Cost, High Efficiency PEM Electrolysis. *ECS Transactions* **2010**, *33* (1), 3-3.

(2) Carmo, M.; Fritz, D. L.; Mergel, J.; Stolten, D. A Comprehensive Review on PEM Water Electrolysis. *Int. J. Hydrogen Energy* **2013**, *38* (12), 4901-4934.

(3) Ayers, K. E.; Marina, O. A. State of the Art in Low-Temperature and High-Temperature Electrolysis. *MRS Bull.* **2024**, *49* (12), 1226-1234.

(4) Tao, L.; Lv, F.; Wang, D.; Luo, H.; Lin, F.; Gong, H.; Mi, H.; Wang, S.; Zhang, Q.; Gu, L.; et al. Mass-Efficient Catalyst Layer of Hierarchical Sub-Nanosheets on Nanowire for Practical Proton Exchange Membrane Electrolyzer. *Joule* **2024**, *8* (2), 450-460.

(5) Wang, C. R.; Stansberry, J. M.; Mukundan, R.; Chang, H.-M. J.; Kulkarni, D.; Park, A. M.; Plymill, A. B.; Firas, N. M.; Liu, C. P.; Lang, J. T.; et al. Proton Exchange Membrane (PEM) Water Electrolysis: Cell-Level Considerations for Gigawatt-Scale Deployment. *Chem. Rev.* **2025**, *125* (3), 1257-1302.

(6) Pham, C. V.; Escalera-López, D.; Mayrhofer, K.; Cherevko, S.; Thiele, S. Essentials of High Performance Water Electrolyzers – From Catalyst Layer Materials to Electrode Engineering. *Adv. Energy Mater.* **2021**, *11* (44), 2101998.

(7) Rodrigo; Mathy, H. G. K.; Lucas; Thijmen, V. N.; John; Matheus, T. Elucidating the Increased Ohmic Resistances in Zero-Gap Alkaline Water Electrolysis. *Electrochim. Acta* **2024**, *507*, 145161.
(8) Georgios, S.; Alejandro, I.-R.; Santeri, P.; Antti, K.; Vesa, R.; Pertti, K.; Jero, A. Influence of Shunt Currents in Industrial-Scale Alkaline Water Electrolyzer Plants. *Renewable Energy* **2024**, *225*, 120266.

(9) Aili, D.; Kraglund, M. R.; Rajappan, S. C.; Serhiichuk, D.; Xia, Y.; Deimede, V.; Kallitsis, J.; Bae, C.; Jannasch, P.; Henkensmeier, D.; et al. Electrode Separators for the Next-Generation Alkaline Water Electrolyzers. *ACS Energy Lett.* **2023**, *8* (4), 1900-1910.

(10) Li, D.; Motz, A. R.; Bae, C.; Fujimoto, C.; Yang, G.; Zhang, F. Y.; Ayers, K. E.; Kim, Y. S. Durability of Anion Exchange Membrane Water Electrolyzers. *Energy and Environmental Science* **2021**, *14* (6), 3393-3419.

(11) Lindquist, G. A.; Gaitor, J. C.; Thompson, W. L.; Brogden, V.; Noonan, K. J. T.; Boettcher, S. W. Oxidative Instability of Ionomers in Hydroxide-Exchange-Membrane Water Electrolyzers. *Energy Environ. Sci.* **2023**, 4373-4387.

(12) Krivina, R. A.; Lindquist, G. A.; Beaudoin, S. R.; Stovall, T. N.; Thompson, W. L.; Twight, L. P.; Marsh, D.; Grzyb, J.; Fabrizio, K.; Hutchison, J. E.; et al. Anode Catalysts in Anion-Exchange-Membrane Electrolysis without Supporting Electrolyte: Conductivity, Dynamics, and Ionomer Degradation. *Adv. Mater.* **2022**, *34* (35).

(13) Zhang, L.; Xu, Q.; Hu, Y.; Chen, L.; Jiang, H. Benchmarking the pH–Stability Relationship of Metal Oxide Anodes in Anion Exchange Membrane Water Electrolysis. *ACS Sustainable Chemistry & Engineering* **2023**, *11* (36), 13251-13259.

(14) Koch, S.; Heizmann, P. A.; Kilian, S. K.; Britton, B.; Holdcroft, S.; Breitwieser, M.; Vierrath, S. The Effect of Ionomer Content in Catalyst Layers in Anion-Exchange Membrane Water Electrolyzers Prepared with Reinforced Membranes (Aemion+™). *J. Mater. Chem. A* **2021**, *9* (28), 15744-15754.

(15) Volk, E. K.; Kreider, M. E.; Kwon, S.; Alia, S. M. Recent Progress in Understanding the Catalyst Layer in Anion Exchange Membrane Electrolyzers – Durability, Utilization, and Integration. *EES Catalysis* **2024**, *2* (1), 109-137.

(16) Park, Y. S.; Jang, M. J.; Jeong, J.-Y.; Lee, J.; Jeong, J.; Kim, C.; Yang, J.; Choi, S. M. Optimization of Ionomer Content in Anode Catalyst Layer for Improving Performance of Anion Exchange Membrane Water Electrolyzer. *International Journal of Energy Research* **2023**, *2023* (1), 3764096.

(17) Volk, E. K.; Clauser, A. L.; Kreider, M. E.; Soetrisno, D. D.; Khandavalli, S.; Sugar, J. D.; Kwon, S.; Alia, S. M. Role of the Ionomer in Supporting Electrolyte-Fed Anion Exchange Membrane Water Electrolyzers. *ACS Electrochemistry* **2025**, *1* (2), 239-248.

(18) Esposito, D. V. Membrane-Coated Electrocatalysts - An Alternative Approach to Achieving Stable and Tunable Electrocatalysis. American Chemical Society: 2018; Vol. 8, pp 457-465.
(19) Maeda, K.; Teramura, K.; Lu, D.; Saito, N.; Inoue, Y.; Domen, K. Noble-Metal/Cr_2O_3 Core/Shell Nanoparticles as a Cocatalyst for Photocatalytic Overall Water Splitting. *Angew. Chem. Int. Ed.* **2006**, *45* (46), 7806-7809.

(20) Vos, J. G.; Wezendonk, T. A.; Jeremiasse, A. W.; Koper, M. T. M. MnO_x/IrO_x as Selective Oxygen Evolution Electrocatalyst in Acidic Chloride Solution. *J. Am. Chem. Soc.* **2018**, *140* (32), 10270-10281.

(21) Chen, W.-M.; Hsieh, H.-Y.; Wu, D.-Z.; Tang, H.-Y.; Chang-Liao, K.-S.; Chi, P.-W.; Wu, P. M.; Wu, M.-K. Advanced TiO_2/Al_2O_3 Bilayer ALD Coatings for Improved Lithium-Rich Layered Oxide Electrodes. *ACS Appl. Mater. Interfaces* **2024**, *16* (10), 13029-13040.

CHAPTER II

ENGINEERING COBALT-BASED SELF-SUPPORTED ANODES FOR PURE-WATER-FED ANION-EXCHANGE-MEMBRANE ELECTROLYSIS

This chapter has been prepared with the intention of submission to *Advanced Materials* for publication, co-authored with Hou, S.; Spence, K. J.; Debela, T; Boettcher, S. W. M.K. and S.W.B. conceptualized and led the project. M.K. prepared samples, collected electrolyzer data, and characterized samples. S.H. and K.J.S. provided feedback on the experiments and data analysis. T.D. provided crystallographic information files. M.K. and S.W.B. wrote the original draft and all authors reviewed and edited the manuscript.

INTRODUCTION

Anion-exchange-membrane water electrolysis (AEMWE) is an emerging technology for H_2 production.[1] Ideally, AEMWE combines benefits from both proton-exchange membrane water electrolyzers (PEMWE) including a low-resistance, zero-gap membrane-electrode assembly and dynamic, pure-water operation, and liquid alkaline water electrolysis (AWE) that use of inexpensive materials for cell components (catalysts, flow fields, etc.).[1] AEMWE technology is limited by difficulty in designing high performance electrodes and their poor durability, mainly coming from ionomer/membrane instability.[2] Ionomers incorporated in anodes are oxidized during operation, limiting hydroxide transport, and this process is accelerated when the anodes are fed with pure water.[3-5]

In PEMWE, iridium-oxide-based catalysts have good performance of oxygen-evolution reaction (OER), and are the only materials currently used in commercial devices.[6-8] Iridium-oxide catalyst nanoparticle inks are prepared with mixtures of ionomer and solvent solutions from which the anode porous electrode layer is fabricated. This ink-based approach works well in part because iridium-oxide has high electrical conductivity (~ 10^4 $S \cdot cm^{-1}$)[9] so that the resistance of the particle network is sufficiently low despite being mixed with ionomer which reduces particle-particle contacts. Ir is a scarce and expensive, though, which limits the large-scale deployment of PEM water electrolyzers.[10] AEMWE can use non-precious group metals (non-PGMs) owing to the alkaline environment.[1,11] Non-PGM anodes in AEMWE devices also appear to outperform Ir-based anodes,[4,12] because IrO_2 has moderate OER activity in alkaline conditions.[4,12,13] However, the common non-PGM catalysts like those based on Co or Ni oxides are typically semiconducting and thus have insufficient electrical conductivity to build optimal porous electrodes using ink processing.

Engineering electrode geometry beyond the random assembles of nanoparticles and ionomer from inks can be used to improve electron and ion conduction pathways through the catalyst-ionomer network, as well as transport and gas removal from the porous electrode. Conventionally, catalyst nanoparticles are mixed with ionomers, sometimes with additional binders or conductive non-catalytic supports, in water-alcohol mixed solvents with an optimized catalyst to ionomer ratio, and the solutions are coated by spraying or other means onto PTLs or membranes.[3,14] This approach is useful from a manufacturing perspective,[14,15] but the ionomers partially cover the catalyst particles surface lowering electric conductivity within the catalyst layer.[16-18] Furthermore, ionomer and/or binder in anode catalyst layers used can be oxidized during operation.[4,5,16,17,19]

In self-supported electrodes where inorganic catalysts are deposited as continuous layers directly on the PTL, ionomers or binders are not required to continuously adhere the catalyst together. Nano-structuring, in principle, can also be judicially controlled to enhance electroactive surface area, increase catalyst loading, and control surface wetting and bubble removal; all useful for robust, high-current-density operation.[16,20] Simple nanostructure electrode fabrication, however, with the desired properties is not trivial. KOH-fed AEMWE cells have been demonstrated with self-supported anodes, mostly using NiFe-oxy(hydroxide)-based OER catalysts.[21-23] The addition of soluble KOH simplifies electrode design because the liquid electrolyte permeates pores of all sizes in the solid, which is not possible with a solid ionomer electrolyte and pure-water feed that is ultimately desired for AEMWE.[24] It is further challenging to adopt NiFe-based, and related, self-supported catalysts in pure-water systems because of their poor electrical conductivity when they are not transformed to the more-conductive oxyhydroxide forms due to limited OH^- accessibility.[25]

Here, Co-based anodes were grown directly on porous transport layers using a hydrothermal synthesis with controlled materials phase and nanostructure to study the link between electrode response, materials properties, and nanostructure. $Co(OH)_x$ and Co_3O_4 self-supported nanostructures were tested in pure water-fed AEMWE devices for the first time and compared to conventional nanoparticle ink-based anodes. To understand interactions and interfaces between the catalyst and ionomer within the porous anodes, the loadings of ionomer and infiltration into the porous self-supported electrode were systematically controlled. Electrode capacitances were measured in pure water and different concentrations of KOH supporting electrolytes to compare the electroactive surface areas. The cell polarization performance was correlated with electrochemical impedance spectroscopy and cyclic-voltammetry analysis,

illustrating the importance of catalyst-ionomer interface for durable AEMWE operation with pure water feed. This work provides the design principles and insights of catalyst-ionomer interfacial structures enabling next generation high-performing AEMWEs, with pure water and low concentration KOH feeds.

RESULTS AND DISCUSSION

Fabrication of Co-based Self-Supported Anodes

Figure 2.1 shows electronic and ionic processes occurring within catalyst layers supported on PTLs in different electrode geometries. In conventional nanoparticle (NP) ink-based electrode geometry, catalyst nanoparticles and ionomers are dispersed in the catalyst layer forming, ideally, percolating electron and hydroxide ion conduction pathways. The weight ratio in inks between catalyst nanoparticles and ionomers,[26,27] water to organic solvent (ethanol or isopropyl alcohol) ratio, and catalyst loading are optimized to maximize performance.[28] Despite this optimization, it is generally not possible to know or control the active electronic and ionic conduction pathways,[16,17] understand which one limits the performance, and determine whether or not more-optimal structures can be built with different approaches due to the complexity.[14] This geometry can possesses nano-scale gaps in ionic or electronic conductions from incomplete ionomer coverage on the particle surface or particles disconnected by ionomers. In self-supported electrodes, where catalyst materials are directly grown on PTLs without incorporation of ionomers or binders during the catalyst layer deposition step, the active catalyst layer establishes a micron-scale continuous electron conduction pathway through the layer, as would any ionomer added to fill the pores. Judicious nano-structuring increases the electroactive surface area and provides a mode to improve surface wetting and gas removal.[16,20] In this electrode geometry, for a pure water-fed AEMWE cell, an ionomer topcoat is critical, as OH^- accessible surface area is limited primarily

to the catalysts surface, where the ionomer topcoat interfaces with the catalyst layer and bulk membranes.[29,30] However, incorporation of an ionomer topcoat might not be critical for a KOH fed AEMWE cell. When the anode is flooded with KOH, most of the catalyst layer grown on the PTL would be utilized as active sites.

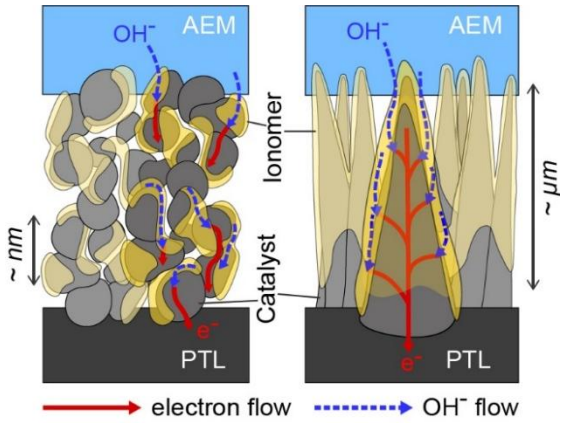

Figure 2.1 Scheme of membrane electrode assemblies with different porous electrode geometries

Geometry comparison between NP ink-based (left) vs. self-supported (right) anodes. Their electronic and ionic pathways are affected by the electrode microstructures forming triple-phase boundaries. The NP ink-based anode possesses regions of nanoparticles inter-disconnected and without ionomers covering the surface, while the self-supported anode retains micro-scale electronic and ionic conduction pathways.

Finally, precise engineering of the catalyst-ionomer interface is possible with self-supported catalysts. For example, the recently developed passivated electrode architecture[30] is an interfacial engineering approach to increase the lifetime of electrodes which synergizes well with self-supported catalysts due to their clearly defined catalyst-ionomer interface. This is important because, so far, no known ionomers are stable in the alkaline and oxidizing environment of the anode in AEMWE.[5] In addition to providing more defined interface, based on our previous work,[30] a self-supported CoO_x anode prepared with an e-beam evaporation of Co and subsequent thermal oxidation showed better performance than the conventional nanoparticle ink-based anode in pure water-fed AEMWE, despite the comparatively very low catalyst loading and surface area.

In this study, nanostructured Co-based OER catalysts were directly deposited on PTLs using a modified hydrothermal synthesis.[31-33] Cobalt nitrate salt and urea were dissolved in DI water in a glass jar with a PTL substrate submerged in the solution (Figures S1 and S2). When the glass jar was assembled and heated up to 100 °C in an oven, urea decomposed and hydrolyzed, releasing carbonate and hydroxide ions into the aqueous solution,[34] raising the pH and promoting direct growth of cobalt carbonate hydroxide, nominally $Co(OH)_x$, on the PTL as well as precipitation of the same material on the bottom of the glass jar (Figure 2.2a). The $Co(OH)_x$ deposited on the PTL can be used as an anode as is or as an oxide form via subsequent heat treatment. The precipitate was washed with deionized water three times using a centrifuge and used for powder sample characterization if needed.

The morphology and loading of synthesized $Co(OH)_x$ were controlled by modifying hydrothermal reaction times and conditions, which will be discussed later. Powder X-ray diffraction (PXRD) patterns were obtained from the precipitates before and after annealing. The as-synthesized sample diffraction pattern matched $Co_6(CO_3)_2(OH)_8 \cdot H_2O$ while after 300 °C annealing in air for 2 h spinel-phase Co_3O_4 was formed (Figure 2.2b). The changes in the Co 2p X-ray photoelectron spectrum (XPS) from predominantly Co^{2+} in the initial hydroxide form to both Co^{2+}/Co^{3+} in oxide form, from the binding energy of the main and satellite peaks, were consistent with this phase transformation (Figure 2.2c).[35] Lattice oxygen (530.2 eV) was observed in O 1s XP spectra after annealing, further confirming oxide formation. Scanning electron microscopy (SEM) images show nanoneedle-structured Co_3O_4 deposited on the Ni alloy PTL (Figure 2.2d). Cross-sectional focused-ion-beam (FIB) SEM images show ~5 μm thick Co-based catalyst layer on the PTL.

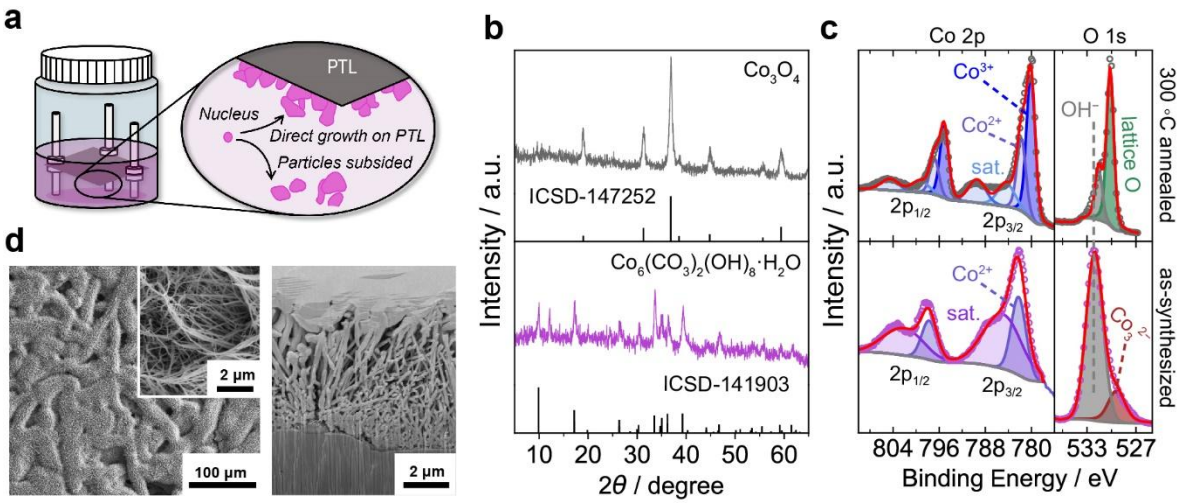

Figure 2.2 Scheme of hydrothermal synthesis and characterization of synthesized catalysts

(a) Hydrothermal synthesis schematic; catalysts were grown directly on PTL, with some additional solution phase growth as particles. **(b)** Powder X-ray diffraction patterns of as-synthesized and 300 °C annealed powders matching with $Co_6(CO_3)_2(OH)_8 \cdot H_2O$ and Co_3O_4, respectively. **(c)** XP spectra of as-synthesized and 300 °C annealed samples on Ni alloy PTL. After annealing, $Co(OH)_x(CO_3)_y$ transformed to Co_3O_4. **(d)** SEM images and cross-sectional image of prepared Co_3O_4 deposited on Ni alloy PTL showing nanoneedle structure of Co_3O_4 deposited on PTL. SEM images were obtained in Co_3O_4 form as $Co(OH)_x$ samples experienced a charging effect because of the insulating property, and there was no significant morphological difference observed between the Co_3O_4 and $Co(OH)_x$ samples.

Effect of Electrode Microstructure

To prepare baseline electrodes for comparison, Co_3O_4 catalyst nanoparticles were mixed with PiperION (PAP-TP-85) ionomer in an isopropyl alcohol (IPA) and deionized water mixture, sonicated, and resulting ink solutions were spray-coated on PTLs to create catalyst-ionomer mixed layers.[3,4] To understand the effect of catalyst microstructure, we compared the response of this conventional electrode with a self-supported catalyst layer directly grown on the Ni alloy PTL. The loadings of Co_3O_4 catalyst were 1.69 mg·cm^{-2} for the nanoparticle Co_3O_4 anode, and 1.51 mg·cm^{-2} for the self-supported Co_3O_4 anode. We deposited 1 mg·cm^{-2} (± 0.2 mg·cm^{-2}) of a PiperION topcoat on the self-supported Co_3O_4 anode, and bare Ni-alloy PTL control, to incorporate ionomers on the catalyst surface using dip-coating.[30,36] Figures S3 and S4 show

incorporated ionomer topcoats onto the Co_3O_4 catalyst layer surface. All anodes were assembled in AEMWE devices with Pt-black cathodes (loading of 2 $mg \cdot cm^{-2}$) and a 40-μm PiperION membrane and tested at 56 °C with pure-water feed.

Comparing the polarization curves (Figure 2.3a) for the AEMWE cells with self-supported Co_3O_4 on PTL, Co_3O_4 NP on PTL, and bare Ni alloy PTL as anodes shows that the self-supported Co_3O_4 anode outperformed the NP ink-based anode by approximately 120 mV and the bare Ni alloy anode by ~190 mV at a current density of 1 $A \cdot cm^{-2}$. Electrochemical impedance spectroscopy (EIS) data obtained at 50 $mA \cdot cm^{-2}$ indicates the high frequency resistance (HFR) for the ink-based anode (0.156 $\Omega \cdot cm^2$) compared to the self-supported anode (0.119 $\Omega \cdot cm^2$) and bare Ni alloy anode (0.130 $\Omega \cdot cm^2$). While the HFR does not include fully mixed ionic/electronic resistances in the porous electrode, due to the parallel equivalent capacitance,[37,38] it is indicative of better electrical interconnection between the catalyst layer and PTL for the self-supported Co_3O_4 than the nanoparticles. The self-supported Co_3O_4 anode also showed higher catalytic activity (Figure 2.3b), with lower charge transfer resistance (1.08 $\Omega \cdot cm^2$) than the other two samples (1.28 $\Omega \cdot cm^2$ for Co_3O_4 NP and 1.27 $\Omega \cdot cm^2$ for bare Ni alloy anodes, respectively, EIS fitting results are in Table A.1). This is consistent with lower voltage in *iR*-corrected overpotential vs. current density (Figure A.6) for the self-supported Co_3O_4 anode. The self-supported Co_3O_4 catalyst layer is not only advantageous to lower the catalyst layer resistance but also leads to better OER kinetics.

To better understand the above results, we measured the (pseudo)capacitive currents at voltages below 1.2 V for the different anodes. The self-supported anode had approximately four times larger capacitive currents than the ink-based anode at 1 V (Figure 2.3c). The bare Ni alloy PTL anode is also plotted as a control, but minimal capacitive current was observed. The shapes of the (pseudo)capacitive voltammograms were also different. The self-supported anode showed

significant capacitive current over the whole voltage window, with roughly linear capacitance increase as the voltage was scanned positive. The nanoparticle anode, however, only showed current on the positive sweep at voltages more positive than about 0.6 V. The shape of the positive edge of the charging box was also much less square. Both observations indicate substantial resistive limitations in accessing the bulk of the porous electrode for the nanoparticles compared to the self-supported catalysts. The electronic properties of the Co_3O_4 under electrochemical conditions are complicated, but generally Co_3O_4 is a semiconductor with relatively low electronic conductivity. The surface of Co_3O_4 is redox-active and likely includes cobalt oxyhydroxide-type phases, which are well known to be insulators as Co^{2+} and only electrically conductive when Co^{3+} is present.[39] The onset of substantial capacitive current at 0.6 V thus may be linked to the oxidation of surface Co species and reduction in interparticle resistances. The lack of the same onset in the self-supported Co_3O_4 electrode, along with the overall much higher (pseudo)capacitive current, are all consistent with improved electrical conductivity in the porous ionomer/catalyst electrode and thus a higher electroactive surface area.

The AEMWE device performance and above-mentioned metrics are well explained by cross-sectional images in Figure 2.3d. We observed inter-particle disconnections (electron transport limited) as well as catalysts without any ionomer (ion transport limited) for the nanoparticle Co_3O_4 anode. However, the self-supported Co_3O_4 has micron-length nanoneedles with ionomers covering most of the catalyst surface, which is similar to what we depict in Figure 2.1 of electrode microstructures.

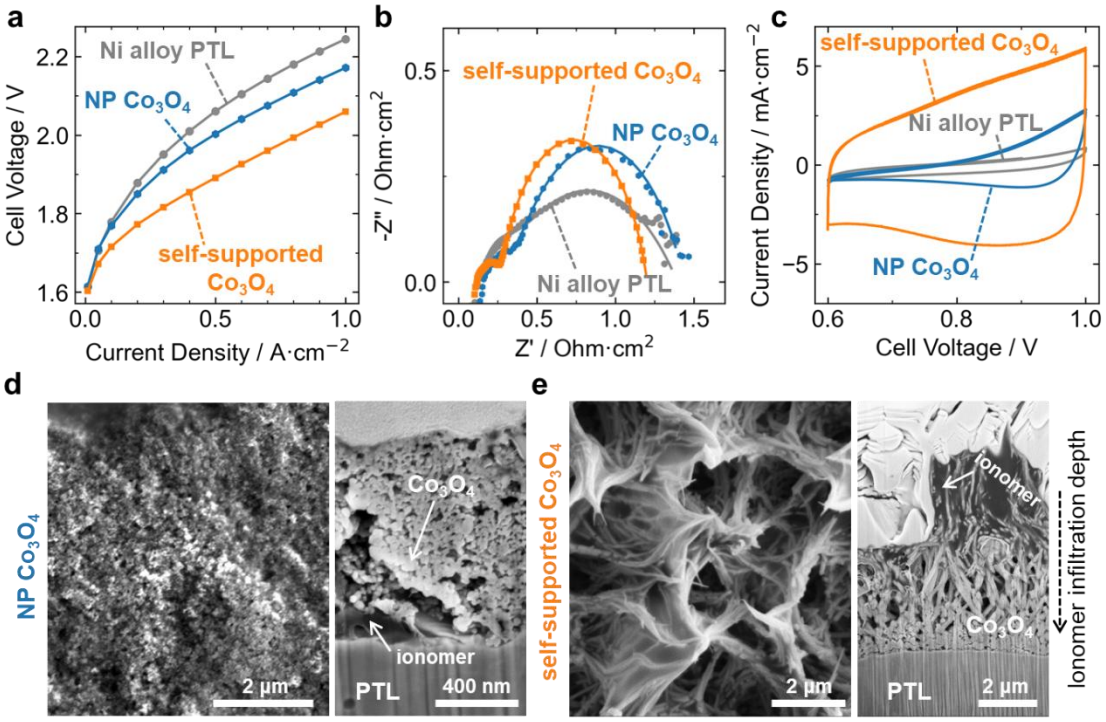

Figure 2.3 Electrode microstructures and corresponding electrochemical data of AEMWE devices

(a) Polarization curves of pure water-fed AEMWE cells at 56 °C with a self-supported Co_3O_4 on PTL, NP ink-based Co_3O_4 on PTL, and bare Ni alloy PTL. **(b)** EIS curves at a current density of 50 $mA \cdot cm^{-2}$ applied and **(c)** cyclic voltammograms at a scan rate of 100 $mV \cdot s^{-1}$ with a sweeping range of 0.6 to 1 V of individual samples in AEMWE cells. Top-view and cross-sectional SEM images of **(d)** NP Co_3O_4 anode and **(e)** self-supported Co_3O_4.

The catalyst and ionomer play important roles in the device, each providing pathways for electrons and ions, respectively, typically following a porous electrode model,[40] and their loadings affect the cell performance. For the catalyst, if the loading is too low, the electron and ion transport may be good, but the result is low catalytic surface area for the reaction. At loadings that are too high, the electronic and ionic resistance can negate the benefit of increased surface area, leading to a typical optimization tradeoff. As the catalyst electrical conductivity increases, the optimal loading is expected to increase as well.

Figure 2.4 shows the various catalyst morphologies and their device response for $Co(OH)_x$ or Co_3O_4 catalyst layers with various mass loadings. The catalyst loading was controlled by varying hydrothermal reaction times. The longer the reaction proceeds, the thicker the $Co(OH)_x$ deposited on the substrate, and thus also the equivalent Co_3O_4 layer after annealing. The catalyst loading was calculated from measuring the mass of the bare Ni alloy substrate before and after the hydrothermal reaction and annealing (300 °C) steps. The cobalt nitrate to urea ratio was also varied to control the growth of cobalt hydroxide layer. When less urea was used, the slower the growth of the catalyst, so a longer hydrothermal reaction was required to achieve similar catalyst loadings (Figure 2.4a). However, this slower growth of $Co(OH)_x$ catalyst led to better performance in AEMWE device (Figure 2.4b, comparing hydroxide form data of Conditions 2 and 3), presumably from different catalyst packing density or nano-structuring. Interestingly, variations in the cobalt nitrate-to-urea ratio not only influenced the growth of the catalyst but also altered its nanostructure (Figure A.7). With a higher concentration of urea in the precursor solution, the catalyst was formed as nanosheets with higher loadings. Conversely, when less urea was used, the catalyst layer grew as nanoneedle structures with a slower growth rate. The growth of cobalt carbonate hydroxide during hydrothermal synthesis involves competition between cobalt-hydroxide and cobalt-carbonate formations, governed by the relative concentrations of hydroxide and carbonate ions and local pH. We speculate that when there is lower concentration of carbonate ions, such as Condition 3, hydroxides bind to cobalt ions, lowering the local pH, further impeding cobalt-carbonate formation.[41] As the reaction proceeds, the catalyst would preferentially grow along the z-direction, leading to nanoneedle structures. A recent calculation-based study[42] suggests that in as-synthesized cobalt carbonate hydroxide, a balance exists between the cobalt carbonate hydroxide phase, which ensures the structural rigidity, and the cobalt hydroxide phase, which gives a higher activity toward

OER. Further, the one-dimensional (1D) growth of nanoneedles reduces the cobalt carbonate hydroxide phase and increases the $Co(OH)_2$ phase, resulting in a higher active surface area. This aligns with our results, showing that using less urea during synthesis generates less carbonate ions, favors 1D growth, and ultimately enhances the catalytic performance.

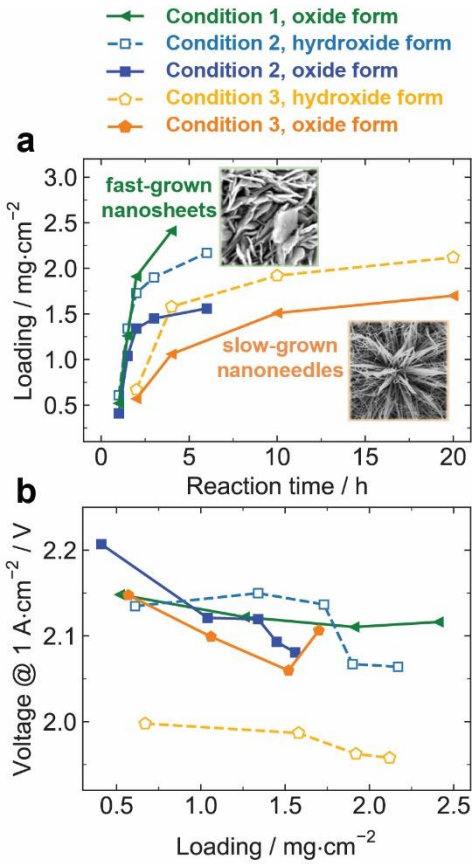

Figure 2.4 Evaluation of hydrothermal synthesis parameters

(a) Reaction-time-dependent catalyst loadings with different cobalt nitrate-to-urea ratios in hydroxide and oxide forms and **(b)** corresponding AEMWE cell voltage at 1 A·cm^{-2}. Condition 1; 27 mmol of cobalt nitrate hexahydrate and 15 mmol urea used. Condition 2; 35 mmol of cobalt nitrate hexahydrate and 15 mmol urea used. Condition 3; 35 mmol of cobalt nitrate hexahydrate and 7.5 mmol urea used. In general, a higher Co precursor to urea ratio leads to slower growth of materials on the substrates and better AEMWE cell performance.

The self-supported Co_3O_4 anode shown in Figure 2.3 and the following data of self-supported $Co(OH)_x$ and Co_3O_4 anodes were prepared as "optimized anodes" using 10 hours of

hydrothermal synthesis (Condition 3). Data of Figure A.24 and A.25 was obtained during the initial optimization thus following Condition 1 with 4 hours of hydrothermal synthesis. Ionomer loading dependent cell performance will be discussed below.

Activation and Degradation of $Co(OH)_x$ and Co_3O_4 Anodes

The phase of OER catalysts and their corresponding electrical conductivities can affect the AEMWE cell activation and durability as they might govern the catalyst layer resistance[28] and surface reconstruction or activation of Co-based catalyst to oxy(hydroxide) form.[43,44] Here, self-supported $Co(OH)_x$ and Co_3O_4 coated anodes with 1 mg·cm^{-2} of PiperION topcoat were compared to understand the activation and degradation of Co-based anodes in the AEMWE device. The self-supported $Co(OH)_x$ shows better performance than the self-supported Co_3O_4, with a difference in the cell voltage of 90 mV at 1 A·cm^{-2} (Figure 2.5a). *iR*-free overpotential vs. current density plots in Figure 2.5 show that Tafel slopes of $Co(OH)_x$ and Co_3O_4 are rather similar, although $Co(OH)_x$ exhibits lower current density at the plotted overpotential range. For example, at η = 300 mV, the current density of $Co(OH)_x$ is 6.3 mA·cm^{-2}, whereas that of Co_3O_4 is 2.1 mA·cm^{-2}. Further, at higher current density (> 0.3 A·cm^{-2}, marked as red in the plot), Co_3O_4 sample shows greater residual overpotential (i.e., ionic resistance, mass transport) compared to $Co(OH)_x$.

To investigate different performance outcomes between $Co(OH)_x$ and Co_3O_4, an AEMWE cell was assembled freshly, and instead of running the normal break-in procedure, which is stepping up the current density to 1 A·cm^{-2} with 100 mA·cm^{-2} intervals, 50 cycles of CV were performed followed by a constant current density hold at 0.5 A·cm^{-2} for 10 min as a chronopotentiometry (CP) step (Figure A.8a). The CV and CP steps were repeated 20 times in a loop. The CV measurements were conducted to monitor the changes in capacitive currents, which can be interpreted as electrochemically active surface area. The CP steps were intended to activate

the catalyst surface by applying oxidative potential to the anode catalysts, followed by possible degradation. Figure 2.5c shows the initial CVs up to the third loop cycle. Continuous activation of self-supported $Co(OH)_x$ upon CP steps led to a noticeable increase in capacitive currents, while the self-supported Co_3O_4 does not show significant changes in capacitive currents during the initial three loop cycles. The capacitive current was maximized in the 3rd loop cycle for $Co(OH)_x$ but decreased continuously for Co_3O_4 (Figure A.8b). The voltage responses of $Co(OH)_x$ during the initial three loop cycles (stabilization from transient overshoot-voltages to steady-state voltages because of the catalyst activation) align with increasing trend of capacitance (Figure A.8c).

The above analysis shows the higher degree of surface reconstruction into conductive and active $CoO_x(OH)_y$ phase for $Co(OH)_x$ form than Co_3O_4 form. This is interesting because $Co(OH)_x$ exhibits a much lower electrical conductivity than Co_3O_4 in powder form (6.4×10^{-5} mS·cm^{-1} versus 10.6 mS·cm^{-1}, respectively), which is likely why the initial capacitive currents were lower in the first loop cycle of CVs for $Co(OH)_x$. Notably, the light purple-colored as-synthesized $Co(OH)_x$ anode changed to black even after an hour-long electrolyzer test, and XP spectra show $Co^{2+/3+}$ mixed peaks after cell operation (Figure 2.5d). After a certain number of loop cycles, CVs show decreasing capacitance over time and an increase in cell voltage over CP steps. It is expected that, similar to previous studies,[4,5] ionomer oxidation and catalyst degradation would happen during CP steps, while repetitive cycling may further facilitate these degradation modes.

The superior performance of $Co(OH)_x$ at high current density may originate from better ionic conduction and concurring surface reconstruction. This might be attributed to the hydrous boundary and surface OH^- that $Co(OH)_x$ could retain after hydrothermal reaction and supply OH^- at the catalyst-ionomer interface during electrolyzer operation even at high current density. On the other hand, the hydrous shell and structural OH^- would be removed for Co_3O_4 after heat treatment,

which could limit OH^- transport to the catalyst surface which interfaces the ionomer. For reference, the crystal structures of $Co(OH)_x$ and Co_3O_4 are shown in Figure A.9.[45,46] For every six Co atoms in $Co(OH)_x$, there exists 8 hydroxyl groups as well as one structural water,[42] which can facilitate reconstruction to oxy(hydroxide) form in bulk structure. Although the performance difference between $Co(OH)_x$ and Co_3O_4 anodes was significantly large in pure water system, this difference became negligible when the cell was fed with 0.1 M KOH (Figure A.10). Here, no ionomer topcoats were used to examine the catalyst activation (surface reconstruction) purely driven by OH^- ions supplied from the soluble electrolyte, KOH. Continuous OH^- supply facilitated catalyst activation in Co_3O_4 form as fast as $Co(OH)_x$ form with the KOH feed mode, relatively similar HFRs and R_{CT}'s as well as kinetics. However, the CV capacitive currents of $Co(OH)_x$ were higher than Co_3O_4.

The durability test (1 $A \cdot cm^{-2}$ applied) was conducted for $Co(OH)_x$ and Co_3O_4 anodes in pure water-fed AEMWE cells with EIS and CV measurements compared before and after (see Figure 2.7 for $Co(OH)_x$ and Figure A.11 for Co_3O_4). Co_3O_4 showed faster voltage degradation, which was driven by increasing HFR and charge transfer resistance (R_{CT}) (Figure A.11b). Comparing CVs before and after the durability test, $Co(OH)_x$ retained its capacitance more (84 %) after the durability test compared to Co_3O_4 (59 %) (Figure A.11d). Post mortem XPS analysis of operated anodes is shown in Figure A.12, where ionomer topcoats were mostly oxidized and flushed out after 20 h of cell operation for both $Co(OH)_x$ and Co_3O_4 anodes. SEM images in Figure A.13 also show most ionomers on the anode surface were gone, and that the catalyst layers underneath the ionomer were degraded, which is likely due to higher oxidative potential on the anode that arises as the ionomer is continuously oxidized. However, the $Co(OH)_x$ anode retained its catalyst layer better than Co_3O_4 anode, evidenced by $Co(OH)_x$ retaining its nanoneedle

structure, which is visible in the SEM images. The Co_3O_4 anode exhibited a higher voltage during durability testing, suggesting that potential-driven ionomer oxidation may occur more rapidly compared to $Co(OH)_x$ anode. This accelerated oxidation could result in a local pH drop at the catalyst surface and promote the dissolution of Co species, thereby reducing the structural integrity of Co_3O_4 catalyst layer.

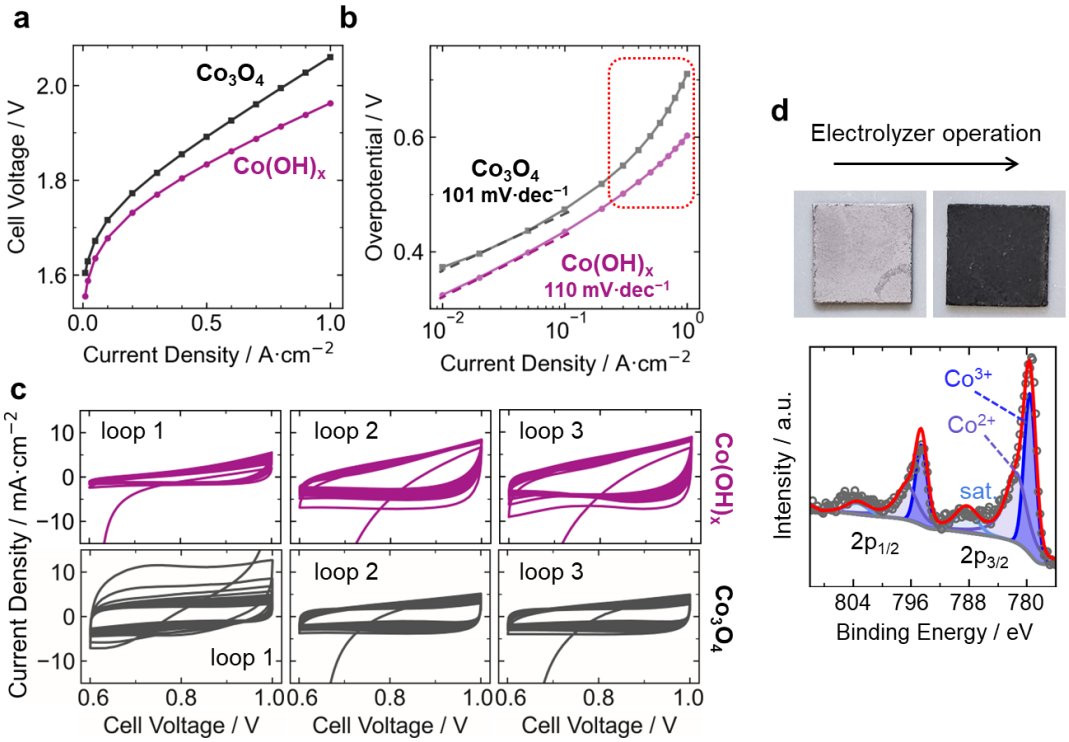

Figure 2.5 Comparison between $Co(OH)_x$ and Co_3O_4 in AEMWE devices

(a) Polarization curves of pure water-fed AEMWE cells at 56 °C with self-supported $Co(OH)_x$ and Co_3O_4 on Ni alloy PTLs. **(b)** *iR*-corrected overpotential versus current density plot of self-supported $Co(OH)_x$ and Co_3O_4 on Ni alloy PTLs. **(c)** CV scans of $Co(OH)_x$ and Co_3O_4 on Ni alloy PTLs in pure water-fed AEMWE cells showing the initial catalyst activation. **(d)** Pictures of pristine $Co(OH)_x$ anode and the anode disassembled after the cell operation (after polarization curve, EIS and CV measurements) and its corresponding Co 2p XP spectrum. The color change of the anode and XP spectra indicate the surface reconstruction to $CoO_x(OH)_y$ after the cell operation.

Effect of Polymer and Supporting Electrolytes

PiperION ionomer was incorporated over the anode catalyst layer to ensure better contact with bulk membrane and provide sufficient pathway for hydroxide ion conduction. This is critical

in a pure water-fed system where the OER is limited to OH^- accessible electrochemical active surface area (ECSA). The loading of ionomer topcoat was systematically controlled to access its role in device performance. The loading of ionomer topcoat was varied by changing the number of times that samples were dipped in a 2 wt% PiperION dispersion. After dip-coating samples in the ionomer dispersion, the samples were dried on a hot plate (80 °C). The dip-coating process was repeated, weighing samples before and after, until target ionomer loadings were achieved. A series of self-supported $Co(OH)_x$ anodes were prepared with PiperION loading of 0, 0.1, 0.5, 1.0, and 1.5 mg·cm^{-2} over 1.92 mg·cm^{-2} of $Co(OH)_x$ catalyst layer. Without an ionomer topcoat on the anode, the cell voltage was 2.31 V at 500 mA·cm^{-2} (Figure 2.6a). Not only did this sample have poor kinetics and high cell resistance, but it also exhibited a non-exponential relationship between the current and voltage in the current density range of 300 to 500 mA·cm^{-2}. The insufficient OH^- supply to the catalyst surface led to a high ionic resistance and thus poor performance. Once the ionomer topcoat was added, even with 0.1 mg·cm^{-2} of ionomer, the cell performance improved substantially. A higher ionomer loading further improved the cell voltage, but increasing the loading from 0.5 to 1.5 mg·cm^{-2} only led to a 20 mV improvement at 1 A·cm^{-2}. At an ionomer loading of 0.1 mg·cm^{-2}, the catalyst surface is barely covered, while at higher ionomer loadings, macrostructures with nanowires clumped together were formed (corresponding cross-sectional images in Figure A.14 and A.3). EIS data at 50 mA·cm^{-2} indicates how the HFR and R_{CT} improved or deteriorated with different ionomer topcoat loadings (Figure A.15a), which can be similarly interpreted from the polarization data. As expected, the sample without a topcoat showed the largest HFR and $R_{CT.}$ The HFR and R_{CT} improved with increasing ionomer topcoat loading up to 0.5 mg·cm^{-2}, while at higher loadings there was no further improvement (Table A.2). We

concluded that having a sufficient ionomer topcoat will result in better performance as it increases the OH^- concentration at the catalyst layer surface.

As a comparison to the ionomer topcoat in pure water study, *ionomer-free* self-supported $Co(OH)_x$ anodes were tested in different KOH concentrations, and their polarization curves are plotted in Figure 2.6b. Even with 1 mM KOH, the performance was notably enhanced, with further increases in KOH concentration leading to a voltage drop to ~ 1.9 V at 2 $A \cdot cm^{-2}$ with 100 mM KOH. Performance improvement of *ionomer-free* anodes with increasing KOH concentrations was also evident in EIS data (Figure A.16a and Table A.3), with decreasing HFR and R_{CT}.

To better understand how polymeric and supporting electrolytes influence catalytic activity, the relationship between current densities at a low overpotential (intrinsic kinetics) and capacitances (ECSAs) was examined. *iR*-corrected overpotentials as a function of logarithmic current density are plotted in Figures A15b,c and A16b. For *ionomer-coated* anodes in the pure water system, deviations from linearity were observed at higher current densities in the Tafel-like plots. In contrast, non-linear responses gradually diminished as the KOH concentration increased in ionomer-free anodes in the KOH system. This difference indicates that the KOH fed system has a sufficient supply of OH^-, while the pure water system, due to its reliance on the ionomer to provide OH^-, experiences an OH^- concentration gradient at the anode surface thereby limiting the OER at higher current densities. In the CVs shown in Figure A.17, the capacitive current increases as either ionomer loading or KOH concentration increases. This indicates sufficient OH^- surrounding the catalyst is fundamental to achieving higher active catalyst surface areas for the OER. The capacitances were calculated based on averaged charges over the sweeping potential range during a CV scan at a rate of 100 $mV \cdot s^{-1}$, which is sufficiently high to observe diffusion-limited behavior and estimate electroactive surface areas. Generally, higher capacitances were

correlated with higher kinetic current density as ionomer loading or KOH concentration increased (Figure 2.6c). Although there are linear trendlines overlayed with data points in the plot, it is not intended to fit with a certain physical model. Interestingly, that, at equal capacitances (between KOH system and pure water), the kinetic current density is still significantly higher in the KOH system.

The activation of *ionomer-free* and *ionomer-coated* $Co(OH)_x$ anodes were compared in AEMWE cells with dilute (0.1 mM) and relatively concentrated (100 mM) KOH feeds. With 0.1 mM KOH, a large overpotential was required to activate and stabilize the *ionomer-free* anode, resulting in a significant cell voltage gap compared to *ionomer-coated* one during the break-in procedure, which is stepping up the current density (Figure A.18). In 100 mM KOH, this performance gap diminished (Figure A.19d), and EIS data even indicated that the ionomer topcoat can contribute additional resistance in the cell, as showcased by the lower HFR without the ionomer topcoat (Figure A.19e). Interestingly, while the capacitance increased with the presence of the ionomer topcoat with pure water and dilute KOH feed, it decreased when ionomer was incorporated in 100 mM KOH fed cell (Figures A17a, and A19c,f). This suggests that OH^- accessibility at the catalyst surface with high concentration of KOH can be hindered by the ionomer topcoat, and therefore it is not beneficial to incorporate ionomer topcoat as it is in pure water system.

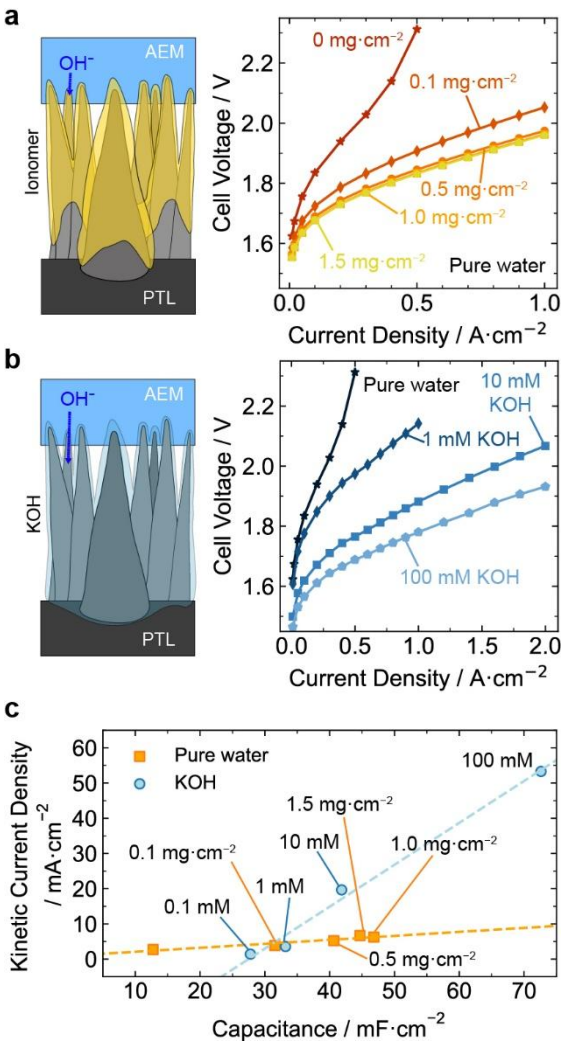

Figure 2.6 Effect of polymer and supporting electrolytes on AEMWE performance

(a) Scheme of *ionomer-coated* anode and its polarization curves of pure water-fed AEMWE cells at 56 °C with different PiperION ionomer topcoat loadings. **(b)** Scheme of *ionomer-free* anode and its polarization curves of AEMWE cells at 56 °C with different concentration of KOH feed. **(c)** Plot of kinetic current densities at an overpotential of 300 mV as a function of capacitance for *ionomer-coated* anodes in pure water and *ionomer-free* anodes in KOH.

With an understanding of how $Co(OH)_x$ is activated and how ionomer and KOH supporting electrolyte affect the cell performance, durability tests were conducted for 1 mg·cm^{-2} ionomer-coated $Co(OH)_x$ anodes in three different systems: a cell with pure water feed, 100 mM KOH feed, and a cell activated with 100 mM KOH and switched to pure water feed. All the cells were operated at 1 A·cm^{-2} for 20 h, with EIS and CV measurements conducted at the beginning of life (BOL)

and end of life (EOL). For the KOH-to-pure-water system, the cell was initially operated with 100 mM KOH feed for 2 h, and EIS and CV were obtained to monitor the initial catalyst activation in KOH (Int I). Subsequently, the cell was flushed with a sufficient amount of water (> 4 L) to remove residual KOH and operation was continued for an additional hour with the cell connected to a large water reservoir (~ 15 L). The durability test was interrupted to obtain another set of EIS and CV (Int II) to assess how the activated catalyst changed upon transitioning to the pure water system. In the pure water system, the cell voltage degraded rapidly with a voltage degradation rate of 8.0 $mV \cdot h^{-1}$ calculated over the last 10 h of the durability test as in Figure 2.7a. However, when KOH was fed to the cell, not only was the previously seen ~150 mV cell voltage improvement observed, but also the voltage degradation rate decreased significantly to 0.24 $mV \cdot h^{-1}$. When KOH was flushed out with pure water, the cell voltage increased by approximately 100 mV initially, and with continuous cell operation using pure water feed, the cell voltage degraded at a rate of 2.7 $mV \cdot h^{-1}$.

CVs obtained at different stages of operation across the three different feed systems are compared in Figure 2.7b. In the KOH-fed cell, the capacitance did not change significantly between the BOL and EOL. Presumably, maximum utilization of $Co(OH)_x$ with the reconstructed $CoO_x(OH)_y$ surface layer was maintained with sufficient OH^- flux. Furthermore, supporting electrolyte suppresses ionomer oxidation to keep the catalyst-ionomer interface stable, perhaps by screen charge-charge interactions at the catalyst-ionomer interface.[5] When the KOH-fed cell was switched to pure water operation, the CV of the Int II stage showed a pseudocapacitive behavior with apparent redox features around 0.9 to 1 V. It was hypothesized that if the KOH was washed completely from the catalyst surface, there would no longer be a charge screening effect, thus allowing activation of $Co(OH)_x$ to $CoO_x(OH)_y$ to be observed from the CV. Further cell operation of more than 10 h did not change the CV feature significantly (Int II vs. EOL), reflecting a

moderate voltage degradation rate. The capacitances at different stages are summarized in Figure A.20. When the cell was operated with pure water only, the initial CV (BOL) had a lower capacity, and it decreased significantly at the EOL. This reflects that the catalyst was not fully activated in pure water, leading to a higher cell voltage as well as a faster voltage degradation rate. It might be possible that the higher cell voltage from less activated catalyst (pure water only) led to higher degree of ionomer oxidation, hence reducing the active surface area. EIS data in Figure 2.7c also supports the stable cell voltage of the KOH system from similar EIS plots at the BOL and EOL, while the kinetics (R_{CT} part) changed a lot from the BOL to EOL for pure water system explaining the fast-degrading cell.

When the cell operated in KOH was flushed with pure water, the initial EIS plots were similar with slight activation and deactivation (BOL→Int I→Int II); longer operation in pure water further led to loss of ECSA as well as degraded kinetics. Probably even though the catalyst was fully activated in KOH without degrading ionomer substantially, when OH^- accessibility became limited again in pure water, ionomer started to degrade starting from the catalyst surface, which could lead to a slight decrease in capacity as well as worse kinetics (increase in R_{CT}). However, the increase in R_{CT} was not as severe as the EIS plot at EOL in the pure water-only system. (EIS fit results are summarized in Table A.4).

In the pure water system, anodes were severely damaged after the cell operation (Figures A12 and A13; ionomer oxidation and catalyst degradation). On the other hand, in KOH and KOH-to-pure-water systems, the catalyst-ionomer interface seems relatively stable. The SEM images in Figure A.21 show that ionomers are still covering the catalyst in both systems. XPS dataset of operated anodes in Figure A.22 also shows substantial reduction in ionomer oxidation. Presumably,

both catalyst surface charge screening effect from supporting electrolytes and lower oxidation potential limited drastic anodic ionomer oxidation.

In Figure 2.7d, we present hypothesized molecular-level models of the anode catalyst-ionomer interfacial structures in different feed modes. Anode catalysts with hydroxyl groups, partially deprotonated in the alkaline conditions ($pH_{PZC} > 9$),[47] will interact with the ionomer backbones cationic groups forming the electrical double layer initially in pure water system. When the oxidative potential is applied to the anode, $Co(OH)_x$ forms $CoO_x(OH)_y$ from deprotonation and oxidation of the metal center at the catalyst surface. When the cell is continuously operated, the close contact between the active $CoO_x(OH)_y$ and ionomer leads to electrochemical oxidation of ionomer, which is one of the dominant failure mechanisms. When the cell is flooded with KOH, it is possible that potassium cations adsorb at the catalyst surface and form a diffuse layer, which then pushes the ionomer away from the catalyst surface as well as screens surface charge. At a given oxidative potential, the catalyst surface reconstructs to a more active phase as it does in pure water system. However, while the degree of catalyst reconstruction is limited to available OH^- from ionomer contacting the catalyst in the pure water system, abundant OH^- in the KOH-fed system would maximize the formation of $CoO_x(OH)_y$. At the same time, the extended diffuse layer of soluble electrolytes would minimize the ionomer oxidation, leading to more-stable cell operation. From these molecular pictures, we hypothesize the improved performance and durability of the KOH-to-pure-water cell relative to the pure water-only cell is due to KOH-modulated activation of $Co(OH)_x$. Even after flushing the cell with pure water, residual K^+ ions can interact with reconstructed catalyst surface, then lower the cell voltage as well as the ionomer oxidation process. Based on hard and soft acids and base (HSAB) theory,[48,49] screening other ions with stronger interactions with the metal oxy(hydroxide) catalyst surface may provide additional

pathways to prevent direct interaction between the catalyst and ionomer and suppress ionomer oxidation. The nature of catalyst-counterion interactions in the supporting electrolyte probably on both catalyst surface charge and the ionic charge and radius of cations.

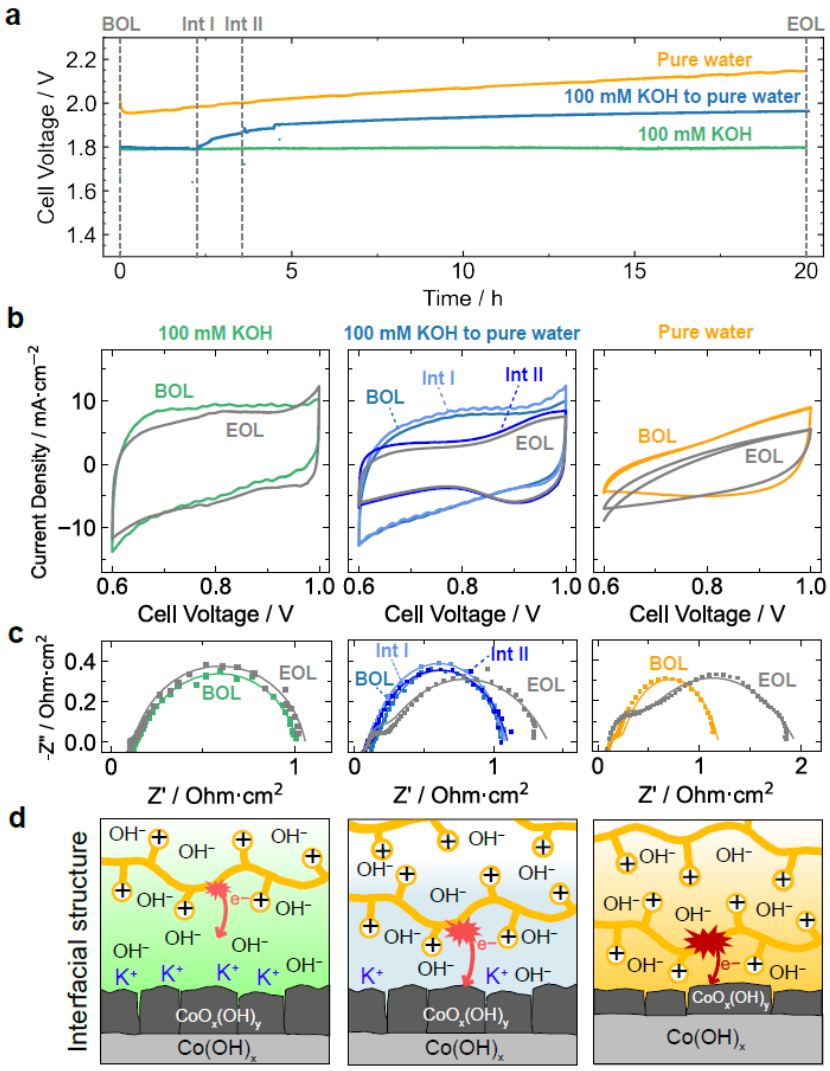

Figure 2.7 Durability of AEMWE devices with different feed modes and corresponding interfacial structures

(a) Durability test of KOH-fed, KOH-to-pure-water-fed, and pure water-fed AEMWE cells with PiperION coated $Co(OH)_x$ anodes. The cell was held at 1 $A \cdot cm^{-2}$ at 56 °C. During the durability test, CV and EIS were obtained at different stages. For the KOH-to-pure-water-fed system, after the cell was active in KOH for 2 h (Int I), the cell was flushed with pure water (Int II). Corresponding **(b)** CVs at a scan rate of 100 $mV \cdot s^{-1}$ with a sweeping range of 0.6 to 1 V, and **(c)** EIS curves at a current density of 50 $mA \cdot cm^{-2}$ applied. **(d)** Molecular-level schemes of catalyst-

ionomer interfaces with different feed modes at the end of life. Related processes include (i) catalyst surface interacting with KOH supporting electrolyte and/or ionomer; (ii) surface reconstruction of $Co(OH)_x$ to more active and conductive $CoO_x(OH)_y$ at oxidative potentials; and (iii) ionomer oxidation. The degree of catalyst surface reconstruction is higher for with KOH feed from abundant OH^-, however, having less ionomer degradation as cationic diffuse layer screens the surface charge of $Co(OH)_x$ and moves ionomer further away from the catalyst surface. In pure water system, direct contact between active catalyst and ionomer leads to severe ionomer oxidation. In KOH-to-pure-water system, activated $CoO_x(OH)_y$ and residual K^+ extended lifetime of the cell compared to the pure water system.

The durability of self-supported anodes in the device was not great in pure water (Figure 2.7a) due to ionomer oxidation and likely subsequent local acidification under OER (which consumes OH^-) and leading to catalyst degradation by mechanical breakdown, reconstruction or dissolution of catalysts. In the self-supported anode geometry, most of the catalyst surface is covered with ionomer, thus the facile electron transport through the catalyst layer would facilitate the ionomer degradation, in-turn accelerating cell degradation. In comparison, for the NP-based anode, disconnection between catalyst nanoparticles because of insulating ionomer covering the catalyst surface would lead to lower active surface area, and inferior performance, but could also lead to slower ionomer degradation (Figure A.23).

To address the problem of fast degrading self-supported anodes, we adopted a passivation layer concept from our previous study.[30] A 3.5-nm thick HfO_x coating was deposited by atomic-layer deposition to stabilize the catalyst-ionomer interface. The passivation layer led to an increase in the cell voltage by ~200 mV at 1 $A \cdot cm^{-2}$ (Figure A.24a). The HfO_x film limits hydroxide transport to the Co_3O_4 catalyst, leading to a lower (pseudo)capacitive current compared to the uncoated Co_3O_4 anode (Figure A.24b). When the cell was kept running at 500 $mA \cdot cm^{-2}$, HfO_x coated Co_3O_4 improved over the course of the durability test with a cell voltage change rate of -3.8 $mV \cdot h^{-1}$ (Figure A.24c), superior to the uncoated Co_3O_4 that degraded at 18 $mV \cdot h^{-1}$. Without the HfO_x coating, both HFR and total charge transfer resistance increased largely after 15 h of the

durability run (Figure A.24d), while with the HfO_x coating, the total charge transfer resistance decreases after the durability run. SEM images in Figure A.25 show that HfO_x coated anode maintained the ionomer topcoat after the durability test, while uncoated anode had all the ionomer-catalyst surface damaged. This is consistent with previous studies of ionomer oxidation in pure-water systems[4,5,30] and our hypothesis to suppress it via interface design. Since a 15 h test is not enough to fully demonstrate the application of self-supported anodes with passivation coatings in the commercial devices, further optimization of additional parameters in passivation coatings can be done in further study with longer test times and harsher conditions (higher temperatures and current densities).

CONCLUSION

In summary, self-supported non-PGM Co-based anodes for AEMWE were prepared *via* a simple hydrothermal reaction. The self-supported Co_3O_4 anode was compared to the conventional Co_3O_4 nanoparticle ink-based anode, emphasizing the importance of catalyst connectivity. When evaluating performance and durability of self-supported $Co(OH)_x$ and Co_3O_4 anodes, $Co(OH)_x$ was found to be better, because of abundant surface hydroxyl groups that facilitate catalyst reconstruction to the more active $CoO_x(OH)_y$ phase. The catalyst-electrolyte interface was investigated with ionomers (solid electrolytes) and KOH supporting electrolytes. Compared to KOH-fed AEMWE, one limitation of self-supported anodes in a pure water-fed AEMWE include their restricted active surface area as a result of the limited catalyst-ionomer interface and its susceptibility to degradation. Effects on cell performance and durability with pure water and KOH feeds were compared and molecular pictures of catalyst-ionomer interfaces were provided. This reflects the durability challenges associated with pure water-fed AEMWE, which we aim to address through advanced interfacial engineering strategies.

With the limitations and challenges established, we now propose methods to further optimize self-supported anodes for pure water-fed AEMWE system. First, we need to improve the catalyst-ionomer interface. The current ionomer coating process is rather simple, either spray coating or dip coating to meet the desired ionomer topcoat loading. These methods result in the ionomer coating the surface of catalyst layer or the pores of the PTL. To maximize the catalyst-ionomer interface area, it's necessary to ensure ionomer infiltration through the deep pores of the prepared catalyst coating. Alternatively, the local pH and hydroxide ion conductivity near catalyst surface can be improved with ionomers with higher ion exchange capacities (IECs).[29] The catalyst layer itself can be improved by depositing highly conductive OER catalysts and by modulating the reconstruction of surface structures to transform to an active oxy(hydroxide) phase. Additionally, pre-activation or in-situ activation of synthesized samples could facilitate the complete transformation to oxy(hydroxide), thereby further enhancing performance. Once more active and electrically conductive catalyst layers are developed, we can pinpoint our effort to stabilize the catalyst-ionomer interface using passivation concepts similar to what we briefly demonstrated with the HfO_x coating.

EXPERIMENTAL METHODS

Hydrothermal growth of $Co(OH)_x$ and Co_3O_4 on Ni alloy PTL

In a glass jar, 35 mmol of $Co(NO_3)_2$ hexahydrate and 7.5 mmol of urea, $CO(NH_2)_2$, were dissolved in 30 mL of 18.2 MΩ·cm high-purity water. A Ni alloy PTL substrate (Hastelloy X, Technetics Inc.) was cut in 3.3x3.3 cm^2, backside-masked with a 0.002-inch-thick polytetrafluoroethylene (PTFE) film, and supported by PTFE threaded rods and Nylon nuts. When tripod supported substrate was submerged in the solution and heated up to 100 °C in an oven, cobalt carbonate hydroxide grew on the PTL as well as precipitates. The hydrothermal reaction

time was varied to control the loading of deposited material. 10 h was found to be an optimum condition. After hydrothermal synthesis, the sample was taken out of the jar, washed with pure water rigorously, and dried overnight to measure the mass loading. $Co(NO_3)_2$ hexahydrate to urea ratio was optimized as the recipe shown here. To prepare Co_3O_4 anode, the as-synthesized sample was annealed at 300 °C for 2 h.

Preparation of HfO_x coating

A HfO_x coating was deposited on top of a self-supported Co_3O_4 anode using an atomic layer deposition system (Savannah, Ultratech). 3.5 nm of HfO_x layer was deposited from repetitive cycles of ALD deposition with 0.4 s-long-pulse of water and 0.015 s-long-pulse of tetrakis(dimethylamido)hafnium(IV), TDMAHf, with an interval of 5 s between each pulse at 250 °C. A Si wafer was put inside the ALD chamber along with Co_3O_4 coated Ni alloy PTL to measure the thickness of the HfO_x film using an ellipsometer.

Materials Characterization

Powder X-ray diffraction (PXRD) patterns were obtained to identify the phase of the prepared catalyst with a Bruker D2 Phaser benchtop diffractometer (Cu K-alpha radiation, λ=1.54 Å). Powder conductivity was measured following the literature.[4] For example, 100 mg of catalyst powder was pressed to form a pellet, and a current-voltage curve was obtained to calculate the electrical conductivity of the pellet. A M-2000 spectroscopic ellipsometer (J.A. Woollam) was used to calculate HfO_x ALD film on a Si wafer. Optical response from 240–1688 nm was fitted with a model of a dielectric film on a Si substrate. Scanning electron microscopy (SEM) images were obtained with a Helios Hydra (Thermo Fisher), to understand the nanostructure of catalyst layers. SEM characterization was performed at 5 kV using ETD or TLD mode. The anodes were cross-sectioned using a plasma focused-ion-bean (PFIB) and SEM images were obtained with elemental

maps using an EDS analyzer. X-ray photoelectron spectroscopy (XPS) measurements were conducted using an ESCALAB 250 (Thermo Scientific) using an Al Kα mono-chromated source with 20 eV pass energy (500 μm spot-size). The binding energies were calibrated with the C 1s spectra (main carbon peaks at 284.8 eV). For post-mortem XPS analysis, cell operated anodes were soaked in 3 M NaCl for to ion-exchange ionomer from OH^- to Cl^- form, washed with pure water vigorously and dried in air before XPS measurements.

Electrode preparation

NP-based electrodes were prepared by spray-coating ink solutions to anode and cathode PTLs. The catalyst ink solution was prepared by mixing 100 mg of nanocatalyst powder, 200 mg of 5 wt% PiperION dispersion (also known as TP-85, Versogen), 0.5 g of 18.2 MΩ·cm high-purity water, and 1.7 g of isopropyl alcohol. The mixed solution was sonicated for 2 hours with a cooling water line immersed in the sonication bath. Pt black (Fuel Cell Store) ink solution was spray-coated on carbon paper (Toray 090, Fuel Cell Store) to prepare cathodes. Co_3O_4 (30–50 nm, US Research Nanomaterials) ink solution was spray-coated on Ni alloy PTL as anodes. During spray-coating, the substrates were fixed on a hot plate at 80 °C to dry out solvent and form catalyst layer. After 1.5–2 $mg \cdot cm^{-2}$ of catalyst layer loading was obtained, a thin ionomer topcoat was applied by spraying 2 wt% PiperION dispersion. For self-supported anodes, after hydrothermal synthesis, PiperION topcoats were applied by dipping the anode into 2 wt% PiperION dispersion with the catalyst-coated sides facing down. After dipping, the samples were placed on the hot plate at 80 °C to remove solvent. The dipping-and-drying step was repeated until the target ionomer loading was obtained. The loading of ionomer topcoat was calculated from the mass difference of anodes before and after dip-coating. Ionomer-free anodes were tested in the electrolyzer without this dip-coating procedure.

Membrane electrode assembly (MEA)

The AEMWE single cell assembly was adopted from previous literature.[3,30] A preconditioned AEM (40 μm PiperION, Versogen) was sandwiched between 1 cm^2 precut cathode and anode electrodes with gaskets. The MEA was compressed in flow fields and bipolar plates. 18.2 MΩ·cm high-purity water was supplied to both anode and cathode from a water tank at 60 $mL \cdot m^{-1}$. The cell temperature was set to 56 ± 1 °C with the water tank (15 L) at 62 °C. Different concentrations of KOH were fed to both anode and cathode for KOH concentration-dependent performance measurements. For a KOH-to-pure-water cell operation, the cell was initially fed with 100 mM KOH, then flushed with pure water (> 4 L) to remove any residual KOH. Lastly, pure water was recirculated in the cell from the water tank.

AEMWE single cell operation

Electrolyzer test was conducted with a potentiostat, BioLogic VSP-300, equipped with a 10 A/5 V booster. Starting from 100 $mA \cdot cm^{-2}$, the current applied to the cell was stepped up to 1 $A \cdot cm^{-2}$ with an interval of 100 $mA \cdot cm^{-2}$ as a cell break-in procedure. The current was held for 2 min for each current step. After breaking in the cell, the current was stepped down with an interval of 100 $mA \cdot cm^{-2}$, held for 10 s for each step, back to 100 $mA \cdot cm^{-2}$ with two additional current steps to 50 and 10 $mA \cdot cm^{-2}$ to obtain a polarization curve. Electrochemical impedance was measured at 50 $mA \cdot cm^{-2}$ with a frequency range of 1 MHz to 100 mHz. Cyclic voltammogram was obtained by sweeping a cell voltage between 0.6 V and 1 V with a scan rate of 100 $mV \cdot s^{-1}$. For a durability test, the cell was held at either 500 $mA \cdot cm^{-2}$ or 1 $A \cdot cm^{-2}$ for a certain period. EIS and CV measurements were repeated after the durability test. When the cell was operated with KOH feed, the current was held up to 2 $A \cdot cm^{-2}$ for the initial cell break-in and obtaining polarization curve. To monitor the activation and degradation of $Co(OH)_x$ and Co_3O_4 anodes, the

cell was cycled with a voltage range of 0.6 V to 1 V for 50 times (CV) then the constant current of 0.5 $A \cdot cm^{-2}$ was applied for 10 minutes (CP). The CV and CP steps were repeated 20 times in a loop.

BRIDGE

Chapter II provides key insights into constructing efficient porous electrodes for AEMWE devices. Well-defined catalyst-ionomer interfaces in self-supported electrodes allow a better understanding of electronic and ionic processes at the interfaces while better control over interfacial reactions, such as catalyst/ionomer activation and degradation. Those understandings form foundations for Chapter III and Chapter IV, which focus on improving anode durability by surface passivation strategies.

REFERENCES

(1) Lee, S. A.; Kim, J.; Kwon, K. C.; Park, S. H.; Jang, H. W. Anion Exchange Membrane Water Electrolysis for Sustainable Large-Scale Hydrogen Production. *Carbon Neutralization* **2022**, *1* (1), 26-48.

(2) Li, D.; Motz, A. R.; Bae, C.; Fujimoto, C.; Yang, G.; Zhang, F. Y.; Ayers, K. E.; Kim, Y. S. Durability of Anion Exchange Membrane Water Electrolyzers. *Energy and Environmental Science* **2021**, *14* (6), 3393-3419.

(3) Lindquist, G. A.; Oener, S. Z.; Krivina, R.; Motz, A. R.; Keane, A.; Capuano, C.; Ayers, K. E.; Boettcher, S. W. Performance and Durability of Pure-Water-Fed Anion Exchange Membrane Electrolyzers Using Baseline Materials and Operation. *ACS Applied Materials and Interfaces* **2021**, *13* (44), 51917-51924.

(4) Krivina, R. A.; Lindquist, G. A.; Beaudoin, S. R.; Stovall, T. N.; Thompson, W. L.; Twight, L. P.; Marsh, D.; Grzyb, J.; Fabrizio, K.; Hutchison, J. E.; et al. Anode Catalysts in Anion-Exchange-Membrane Electrolysis without Supporting Electrolyte: Conductivity, Dynamics, and Ionomer Degradation. *Adv. Mater.* **2022**, *34* (35).

(5) Lindquist, G. A.; Gaitor, J. C.; Thompson, W. L.; Brogden, V.; Noonan, K. J. T.; Boettcher, S. W. Oxidative Instability of Ionomers in Hydroxide-Exchange-Membrane Water Electrolyzers. *Energy Environ. Sci.* **2023**, 4373-4387.

(6) Maximilian, M.; Matthias, F. E.; Matthias, K.; Frank, A.; Maximilian, B.; Jan, B.; Christian, E.; Christian, G.; Antonina, M.; Hubert, A. G. Durability Testing of Low-Iridium PEM Water Electrolysis Membrane Electrode Assemblies. *J. Electrochem. Soc.* **2022**, *169* (6), 064505.

(7) Mark, C.; Christopher, M. Z.; Margery, R. Perspectives on Current and Future Iridium Demand and Iridium Oxide Catalysts for PEM Water Electrolysis. *Catal. Today* **2023**, *420*, 114140.

(8) Carmo, M.; Fritz, D. L.; Mergel, J.; Stolten, D. A Comprehensive Review on PEM Water Electrolysis. *Int. J. Hydrogen Energy* **2013**, *38* (12), 4901-4934.

(9) Scarpelli, F.; Godbert, N.; Crispini, A.; Aiello, I. Nanostructured Iridium Oxide: State of the Art. *Inorganics* **2022**, *10* (8), 115.

(10) Christine, M.; Michel, S.; Boris, B.; Richard, H.-R. Is Iridium Demand a Potential Bottleneck in the Realization of Large-Scale PEM Water Electrolysis? *Int. J. Hydrogen Energy* **2021**, *46* (46), 23581-23590.

(11) Juchan, Y.; Myeong Je, J.; Xiaojun, Z.; Yoo Sei, P.; Jooyoung, L.; Sung Mook, C.; Yadong, Y. Non-Precious Electrocatalysts for Oxygen Evolution Reaction in Anion Exchange Membrane Water Electrolysis: A Mini Review. *Electrochem. Commun.* **2021**, *131*, 107118.

(12) Jang, M. J.; Yang, J.; Lee, J.; Park, Y. S.; Jeong, J.; Park, S. M.; Jeong, J.-Y.; Yin, Y.; Seo, M.-H.; Choi, S. M.; et al. Superior Performance and Stability of Anion Exchange Membrane Water Electrolysis: pH-Controlled Copper Cobalt Oxide Nanoparticles for the Cxygen Evolution Reaction. *J. Mater. Chem. A* **2020**, *8* (8), 4290-4299.

(13) Trotochaud, L.; Ranney, J. K.; Williams, K. N.; Boettcher, S. W. Solution-Cast Metal Oxide Thin Film Electrocatalysts for Oxygen Evolution. *J. Am. Chem. Soc.* **2012**, *134* (41), 17253-17261.

(14) Volk, E. K.; Kreider, M. E.; Kwon, S.; Alia, S. M. Recent Progress in Understanding the Catalyst Layer in Anion Exchange Membrane Electrolyzers – Durability, Utilization, and Integration. *EES Catalysis* **2024**, *2* (1), 109-137.

(15) Janghoon, P.; Zhenye, K.; Guido, B.; Michael, U.; Scott, A. M. Roll-to-roll Production of Catalyst Coated Membranes for Low-Temperature Electrolyzers. *J. Power Sources* **2020**, *479*, 228819.

(16) Yang, H.; Driess, M.; Menezes, P. W. Self-Supported Electrocatalysts for Practical Water Electrolysis. *Adv. Energy Mater.* **2021**, *11* (39), 2102074.

(17) Sun, H.; Yan, Z.; Liu, F.; Xu, W.; Cheng, F.; Chen, J. Self-Supported Transition-Metal-Based Electrocatalysts for Hydrogen and Oxygen Evolution. *Adv. Mater.* **2020**, *32* (3), 1806326.

(18) Romiluyi, O.; Danilovic, N.; Bell, A. T.; Weber, A. Z. Membrane-electrode assembly design parameters for optimal CO_2 reduction. *Electrochemical Science Advances* **2023**, *3* (1), e2100186.

(19) Krivina, R. A.; Lindquist, G. A.; Yang, M. C.; Cook, A. K.; Hendon, C. H.; Motz, A. R.; Capuano, C.; Ayers, K. E.; Hutchison, J. E.; Boettcher, S. W. Three-Electrode Study of Electrochemical Ionomer Degradation Relevant to Anion-Exchange-Membrane Water Electrolyzers. *ACS Applied Materials and Interfaces* **2022**, *14* (16), 18261-18274.

(20) Wang, P.; Wang, B. Designing Self-Supported Electrocatalysts for Electrochemical Water Splitting: Surface/Interface Engineering toward Enhanced Electrocatalytic Performance. *ACS Appl. Mater. Interfaces* **2021**, *13* (50), 59593-59617.

(21) Qiucheng, X.; Liyue, Z.; Jiahao, Z.; Jingyu, W.; Yanjie, H.; Hao, J.; Chunzhong, L. Anion Exchange Membrane Water Electrolyzer: Electrode Design, Lab-Scaled Testing System and Performance Evaluation. *EnergyChem* **2022**, *4* (5), 100087.

(22) Lei, W.; Ziang, X.; Peican, W.; Peng-Fei, L.; Qin, X.; Baoguo, W. Dual Regulation Both Intrinsic Activity and Mass Transport for Self-Supported Electrodes Using in Anion Exchange Membrane Water Electrolysis. *Chemical Engineering Journal* **2022**, *431*, 133942.

(23) Zheng, Y.; Serban, A.; Zhang, H.; Chen, N.; Song, F.; Hu, X. Anion Exchange Ionomers Enable Sustained Pure-Water Electrolysis Using Platinum-Group-Metal-Free Electrocatalysts. *ACS Energy Lett.* **2023**, 5018-5024.

(24) Kong, T.-H.; Thangavel, P.; Shin, S.; Kwon, S.; Choi, H.; Lee, H.; Park, N.; Woo, J.-J.; Kwon, Y. In-Situ Ionomer-Free Catalyst-Coated Membranes for Anion Exchange Membrane Water Electrolyzers. *ACS Energy Lett.* **2023**, *8* (11), 4666-4673.

(25) Grace, L.; Shannon, B. Reports From The Frontier: Overcoming Limitations for Pure-water Anion-exchange-membrane Electrolysis. *The Electrochemical Society Interface* **2023**, *32* (2), 32.

(26) Alaa, Y. F.; Lin, X.; Alejandro Oyarce, B.; Frode, S.; Donald, K.; Svein, S. Effect of Anion Exchange Ionomer Content on Electrode Performance in AEM Water Electrolysis. *Int. J. Hydrogen Energy* **2020**, *45* (53), 28272-28284.

(27) Koch, S.; Heizmann, P. A.; Kilian, S. K.; Britton, B.; Holdcroft, S.; Breitwieser, M.; Vierrath, S. The Effect of Ionomer Content in Catalyst Layers in Anion-Exchange Membrane Water Electrolyzers Prepared with Reinforced Membranes (Aemion+™). *J. Mater. Chem. A* **2021**, *9* (28), 15744-15754.

(28) Kreider, M. E.; Yu, H.; Osmieri, L.; Parimuha, M. R.; Reeves, K. S.; Marin, D. H.; Hannagan, R. T.; Volk, E. K.; Jaramillo, T. F.; Young, J. L.; et al. Understanding the Effects of Anode Catalyst Conductivity and Loading on Catalyst Layer Utilization and Performance for Anion Exchange Membrane Water Electrolysis. *ACS Catal.* **2024**, *14* (14), 10806-10819.

(29) Xiao, J.; Oliveira, A. M.; Wang, L.; Zhao, Y.; Wang, T.; Wang, J.; Setzler, B. P.; Yan, Y. Water-Fed Hydroxide Exchange Membrane Electrolyzer Enabled by a Fluoride-Incorporated Nickel–Iron Oxyhydroxide Oxygen Evolution Electrode. *ACS Catal.* **2021**, *11* (1), 264-270.

(30) Kwak, M.; Ojha, K.; Shen, M.; Boettcher, S. W. Electrically Insulated Catalyst–Ionomer Anode Interfaces toward Durable Alkaline Membrane Electrolyzers. *ACS Energy Lett.* **2024**, *9* (3), 1025-1034.

(31) Rong, C.; Hsin-Yi, W.; Jianwei, M.; Hongbin, Y.; Bin, L. A Flexible High-Performance Oxygen Evolution Electrode with Three-Dimensional $NiCo_2O_4$ Core-Shell Nanowires. *Nano Energy* **2015**, *11*, 333-340.

(32) Ji, H.; Ma, Y.; Cai, Z.; Yun, M.; Han, J.; Tong, Z.; Wang, M.; Suhr, J.; Xiao, L.; Jia, S.; et al. Mesoporous Cobalt Oxide (CoO_x) Nanowires with Different Aspect Ratios for High Performance Hybrid Supercapacitors. *Nanomaterials (Basel, Switzerland)* **2023**, *13* (4).

(33) Yang, Q.; Lu, Z.; Sun, X.; Liu, J. Ultrathin Co_3O_4 Nanosheet Arrays with High Supercapacitive Performance. *Sci. Rep.* **2013**, *3* (1), 3537.

(34) Li, X.; Kale, G. M. Urea-Based Hydrothermal Synthesis of ITO Nanopowders. *Journal of Physics: Conference Series* **2006**, *26* (1), 319.

(35) Mark, C. B.; Brad, P. P.; Andrew, P. G.; Leo, W. M. L.; Andrea, R. G.; Roger St, C. S. Resolving Surface Chemical States in XPS Analysis of First Row Transition Metals, Oxides and Hydroxides: Cr, Mn, Fe, Co and Ni. *Appl. Surf. Sci.* **2011**, *257* (7), 2717-2730.

(36) Xiao, J.; Oliveira, A. M.; Wang, L.; Zhao, Y.; Wang, T.; Wang, J.; Setzler, B. P.; Yan, Y. Water-Fed Hydroxide Exchange Membrane Electrolyzer Enabled by a Fluoride-Incorporated Nickel-Iron Oxyhydroxide Oxygen Evolution Electrode. *ACS Catal.* **2021**, *11* (1), 264-270.

(37) Yongzhen, Q.; Jiangjin, L.; Dinesh, C. S.; Ying, H.; Andrea, P.; Andrew, T. H.; Iryna, V. Z. Interpreting Ionic Conductivity for Polymer Electrolyte Fuel Cell Catalyst Layers with Electrochemical Impedance Spectroscopy and Transmission Line Modeling. *J. Electrochem. Soc.* **2021**, *168* (5), 054502.

(38) Emily, K. V.; Stephanie, K.; Shaun, M. A. Catalytic Activity and Stability of Non-Platinum Group Metal Oxides for the Oxygen Evolution Reaction in Anion Exchange Membrane Electrolyzers. *J. Electrochem. Soc.* **2023**, *170* (6), 064506.

(39) Burke, M. S.; Zou, S.; Enman, L. J.; Kellon, J. E.; Gabor, C. A.; Pledger, E.; Boettcher, S. W. Revised Oxygen Evolution Reaction Activity Trends for First-Row Transition-Metal (Oxy)hydroxides in Alkaline Media. *J. Phys. Chem. Lett.* **2015**, *6* (18), 3737-3742.

(40) Itou, Y.; Ogihara, N.; Kawauchi, S. Role of Conductive Carbon in Porous Li-Ion Battery Electrodes Revealed by Electrochemical Impedance Spectroscopy Using a Symmetric Cell. *J. Phys. Chem. C* **2020**, *124* (10), 5559-5564.

(41) Shawn, L. R.; Eugene, S. I.; Odeta, Q.; Yingge, D.; Sebastien, N. K. Cobalt Hydroxide–Cobalt Carbonate Competitive Growth on Carbonate Surfaces. *Chem. Geol.* **2022**, *605*, 120951.

(42) Oqmhula, K.; Toma, T.; Maezono, R.; Hongo, K. First-Principles-Based Insight into Electrochemical Reactivity in a Cobalt-Carbonate-Hydroxide Pseudocapacitor. *ACS Omega* **2023**, *8* (7), 6743-6752.

(43) Yang, J.; Liu, H.; Martens, W. N.; Frost, R. L. Synthesis and Characterization of Cobalt Hydroxide, Cobalt Oxyhydroxide, and Cobalt Oxide Nanodiscs. *J. Phys. Chem. C* **2010**, *114* (1), 111-119.

(44) Pralong, V.; Delahaye-Vidal, A.; Beaudoin, B.; Gérand, B.; Tarascon, J. M. Oxidation Mechanism of Cobalt Hydroxide to Cobalt Oxyhydroxide. *J. Mater. Chem.* **1999**, *9* (4), 955-960.

(45) Momma, K.; Izumi, F. VESTA 3 for Three-Dimensional Visualization of Crystal, Volumetric and Morphology Data. *J. Appl. Crystallogr.* **2011**, *44* (6), 1272-1276.

(46) Bhojane, P.; Le Bail, A.; Shirage, P. M. A Quarter of a Century After Its Synthesis and with >200 Papers Based on Its Use, `$Co(CO_3)_{0.5}(OH)\cdot 0.11H_2O$' Proves to be $Co_6(CO_3)_2(OH)_8\cdot H_2O$ from Synchrotron Powder Diffraction Data. *Acta Crystallographica Section C* **2019**, *75* (1), 61-64.

(47) Ardizzone, S.; Spinolo, G.; Trasatti, S. The Point of Zero Charge of Co_3O_4 Prepared by Thermal Decomposition of Basic Cobalt Carbonate. *Electrochim. Acta* **1995**, *40* (16), 2683-2686.

(48) Pearson, R. G. Absolute Electronegativity and Hardness: Application to Inorganic Chemistry. *Inorg. Chem.* **1988**, *27* (4), 734-740.

(49) Birkel, A.; Loges, N.; Mugnaioli, E.; Branscheid, R.; Koll, D.; Frank, S.; Panthfer, M.; Tremel, W. Interaction of Alkaline Metal Cations with Oxidic Surfaces: Effect on the Morphology of SnO_2 Nanoparticles. *Langmuir* **2010**, *26* (5), 3590-3595.

CHAPTER III

ELECTRICALLY INSULATED CATALYST–IONOMER ANODE INTERFACES TOWARD DURABLE ALKALINE MEMBRANE ELECTROLYZERS

Published as **Kwak, M**.; Ojha, K.; Shen, M.; Boettcher, S. W. Electrically Insulated Catalyst–Ionomer Anode Interfaces toward Durable Alkaline Membrane Electrolyzers. ACS Energy Lett. **2024**, *9* (3), 1025-1034. M.K., K.O. and S.W.B. designed the experiment and led the project. M.K. and K.O. prepared samples and collected electrolyzer data. M.K. conducted SEM and XPS measurement and analysis. K.O. led TEM data acquisition. M.S. performed conductive AFM characterization. M.K., K.O. and S.W.B. wrote the manuscript with input from all authors.

INTRODUCTION

Proton-exchange-membrane and alkaline water electrolysis (PEMWE and AWE) systems are the leading commercial technologies for green H_2 production. However, the locally acidic operating environment in PEMWE requires the use of expensive acid-stable catalysts, like IrO_2, and bipolar plates.[1,2] Fluorinated polymers are also used for the membrane/ionomer in PEMWE which might limit the deployment of PEM electrolyzers,[3] although this is likely manageable in the closed electrolyzer water loop. In contrast, AWE uses concentrated KOH electrolyte, with cheaper earth-abundant catalysts and flow fields / bipolar plates, thus lowering the system cost per electrode area. AWE, however, has traditional limitations in operating current density and hydrogen purity, crossover, and electrochemical pressurization.[4,5] Anion-exchange-membrane

water electrolysis (AEMWE) is an emerging technology that, in principle, combines advantages for both PEMWE (zero-gap configuration with electrolyte-free water feed, no soluble electrolyte, differential pressure, variable load, etc.) and AWE systems (the use of inexpensive non-platinum-group-metal catalysts and cheap bipolar plates).[6-8]

While much effort has gone to anion-exchange membrane/ionomer development for AEMWE stability in the presence of the strong OH^- nucleophile,[9-13] as well as in catalyst development,[14-18] the durability of the system remains the primary limiting factor for commercialization and scale-up.[4,8,19,20] Supporting electrolyte KOH feed (typically 0.1 to 1 M KOH) has been used to compensate the substantial performance and durability loss from instable ionomer/membrane of pure-water AEMWE system,[21,22] and AEM electrolyzers with dilute KOH feed have been commercialized by Enapter.[23] The dilute KOH decreases the voltage degradation rate at least an order of magnitude compared to the pure water feed,[7,21,24] although the soluble electrolyte re-introduces some of the limitations of traditional AWE. For example, there are possible issues with increased balance-of-plant cost, shunt currents, and reverse polarizations on shutdown.[25-28]

In pure-water AEMWE, and likely also (to a lesser extent) in liquid-KOH AEMWE, the oxidative instability of ionomers/membranes at the anode driving the oxygen evolution reaction (OER) is a key durability issue.[29-31] The anode catalysts and ionomers are traditionally in direct contact in the catalyst layer, and thus ionomers must be stable under the simultaneously highly oxidizing and strongly alkaline environment. However, even fluorocarbon polymers like Nafion degrade under these conditions,[21] perhaps because the oxidative bias increases the rate of nucleophilic attack by the hydroxide (Nafion ionomer is nominally stable at an acidic anode).

These anode ionomer-degradation processes increase the overvoltage at the anode due to loss of active catalyst surface area and increased hydroxide-transport-related losses.

The oxidative instability of ionomers interfaced with catalysts might be mitigated by interfacial engineering strategies, for example, by adding a thin film of electrically insulating metal oxides between ionomers and catalysts that block the electron flow from ionomers to catalysts but permits ions to transport. Thin layers of SiO_x and other metal oxides have been coated on top of electrocatalysts to minimize the undesired catalyst degradation processes[32-37] (*i.e.*, dissolution, catalyst-particle coalescence, detachment, or chemical poisoning) with desirable permselectivity towards reactants to maintain the electrocatalytic activity.[38,39] Metal-oxide coatings on battery electrode materials have been similarly used to prevent chemical attack and improve lifetime and electrolyte stability under cycling.[40,41] Because reactive electrochemical interfaces are broadly important in technology, strategies for understanding and engineering interfacial layers to enhance durability are of significant value.

Here we investigate interfacial engineering to stabilize the ionomer contacting the anode catalyst in AEMWE systems. We developed "passivated" anodes consisting of HfO_x-coated IrO_x or CoO_x nanostructured OER catalysts grown directly on the porous transport layer (PTL, sometimes also referred to as the gas diffusion layer or GDL). The model OER catalyst is prepared by electron-beam evaporation of Ir and Co, followed by thermal oxidation of an exposed metal layer on a stainless steel PTL for CoO_x. The interface is stabilized by adding HfO_x via atomic layer deposition (ALD), prior to fabricating and testing pure-water-fed AEMWE cells. The passivated anodes showed reduced interfacial anode-ionomer oxidation and improved durability with a small decrease in voltage efficiency compared to the unpassivated control devices. The electronic insulation of the passivation coatings was mapped with conductive-atomic force microscopy (c-

AFM), and post-mortem XPS analysis showed that catalyst-ionomer interface was stabilized with the thin film of HfO_x. We discuss strategies to improve passivation layers that are ideally electronically insulating, chemically stable, basic oxides that absorb protons from water providing free OH^- for conduction through the layer. These new concepts in catalyst-ionomer interfacial engineering are likely to play a key role in AEMWE and other emerging electrochemical technologies where dynamic and reactive interfaces are central to performance.

RESULTS AND DISCUSSION

Catalyst-Ionomer Interfaces

Figure 3.1 shows the AEMWE single-cell configuration with a conventional- and passivated-anode structure, along with their degradation and working mechanisms. Catalyst-coated electrodes and the AEMs are assembled and fed with pure water to generate H_2 and O_2 gas at the cathode and anode, resp3ectively (Figure 3.1a). Conventional anodes are fabricated by spray-coating catalyst/ionomer ink onto porous PTLs prior to integrating with the membrane in the cell (Figure 3.1b). In a microscopic picture of the catalyst-ionomer interface, the ionomer conducts OH^-, facilitating the OER at the interface with the catalyst (Figure 3.1b.*i*). This direct physical contact, however, allows electrons to flow from ionomer to catalyst, leading to electrochemical oxidative degradation of ionomers (Figure 3.1b.*ii*).

We demonstrate a new type of passivated anode (Figure 3.1c) where a thin OER catalyst layer grown directly on a PTL is coated with a metal-oxide thin film, here HfO_x, prior to adding ionomer. This passivation layer is meant to allow the transport of hydroxide ions, due to the porosity in the amorphous oxide (Figure 3.1c.*i*), but insulates (ideally) against direct electron transfer between catalysts and ionomers (Figure 3.1c.*ii*). HfO_x was chosen as a passivation layer material because as an amorphous thin film, it is electrically insulating (and thus used as a gate

dielectric in the semiconductor industry),[42,43] it has high alkaline stability,[43] and probably suitable for ion transport as are other thin amorphous oxides[44] and oxide surfaces.[45,46] HfO_x can also be deposited using well-established procedures and precursors in robust, conformal films by atomic layer deposition (ALD);[47,48] a technique sufficiently cost-effective and scalable to be integrated into catalyst/PTL processes.[49,50]

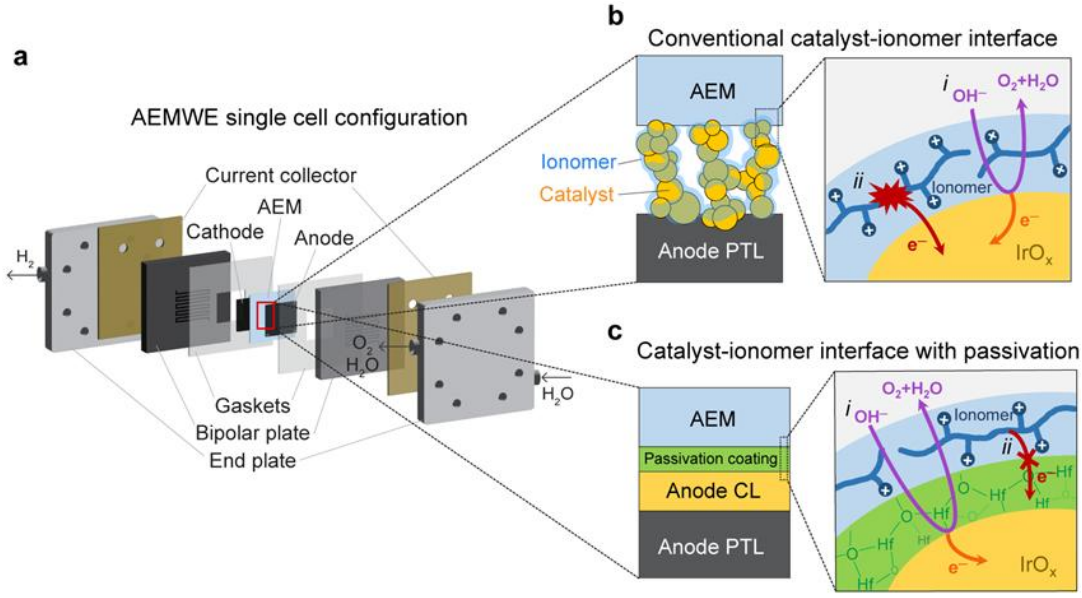

Figure 3.1 Scheme of AEMWE single cell configuration, conventional catalyst-ionomer interface and passivated catalyst-ionomer interface

(a) AEMWE single-cell configuration. **(b)** Conventional anode structure interfacing bulk membrane with a corresponding microscopic picture of the catalyst-ionomer interface describing ionic and electronic processes: (*i*) OH^- transport and OER, (*ii*) oxidative ionomer degradation. **(c)** Passivated anode interfacing bulk membrane with a corresponding microscopic picture of the passivated catalyst-ionomer interface describing ionic and electronic processes: (*i*) OH^- transport and OER with HfO_x coating and (*ii*) suppression of ionomer degradation with an electronically insulating HfO_x layer.

Fabrication of model anodes

To study the effect of passivation coatings at the catalyst-ionomer interface, simplified Ir- and CoO_x-based anodes were built. In one case, a 75 nm layer of Ir metal was deposited on a stainless steel (SS) PTL as a catalyst layer using electron-beam evaporation. To enhance the

performance of the Ir anode, we tried annealing the as-deposited samples to transform metallic Ir to iridium oxide. However, oxidation required ~600 °C to form iridium oxide (Figure B.1) and concomitant oxidation of the SS PTL substrate apparently led to additional resistance. In another case, we deposited ~150 nm of Co on SS PTLs which were annealed at 300 °C to yield cobalt oxides which had better performance and stability (Figure B.2). Scanning electron microscopy (SEM) images (Figures 3.2a and 3.2b) show uniform surface coverage and morphology of Ir and CoO_x catalyst layers on the SS GDLs. While the Ir catalyst layer was a continuous film with island-type particles on the SS GDL, the CoO_x catalyst layer developed nanostructured platelets on the SS PTL driven by thermal annealing and oxide crystallization. SEM cross-sectional images were obtained using focused ion beam (FIB) milling which illustrate the uniformity of the catalyst layers on SS GDLs. The thicknesses of Ir and CoO_x catalyst layers were ~75 nm and ~200 nm, respectively (Figures 3.2c and 3.2d). X-ray photoelectron spectroscopy (XPS) spectra of Ir 4f and Co 2p were used to assess the chemical state of the as-synthesized catalysts (Figures 3.2e and 3.2f).

Fabrication of passivation coatings

A passivation coating, a thin film of HfO_x, was deposited on top of the anode catalyst layer using ALD. The thickness of the HfO_x controls the OH^- transport and electron-insulating properties, as well as the electrochemical and mechanical stability of the films. Figure 3.3a shows a cross-sectional SEM image of a 2.5 nm-thick HfO_x-coated CoO_x electrode with a topcoat of PiperION ionomer. High-angle annular dark-field scanning transmission electron microscopy (HAADF-STEM) images with energy dispersive X-ray spectroscopy (EDS) mapping (Figure 3.3b) and a line-cut scan of elements (Figure 3.3c) show individual layers; a SS PTL, CoO_x catalyst layer, and HfO_x passivation layer. The electrical insulation of HfO_x was tested by using conducting atomic-force microscopy (c-AFM). Electrical current through the HfO_x on a partially coated Pt metal film

was measured along with height under voltage bias. Figures 3.3d and 3.3e show that ~2.5 nm of HfO_x thin film was deposited on the Pt layer and that this nanoscale film is conformal enough to insulate the conductive Pt surface. Thickness-dependent c-AFM measurements are further shown in Figure B.3.

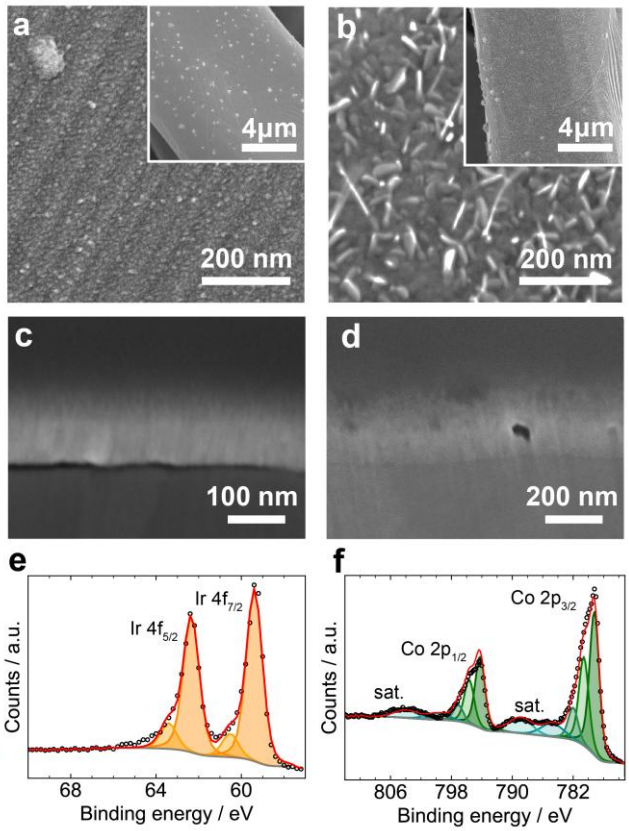

Figure 3.2 SEM images of Ir and CoO_x-based electrodes and corresponding XPS

SEM images of the **(a)** Ir-based electrode and **(b)** CoO_x-based electrode showing surface features. Cross-sectional SEM images of the **(c)** Ir-based electrode and **(d)** CoO_x-based electrode. XP spectra of the **(e)** Ir-based electrode and **(f)** CoO_x-based electrode. The XP spectra fits were made assuming metallic Ir with a surface oxide layer (Ir^{4+}) in Ir 4f spectra and mixed oxidation states of Co^{3+}/Co^{2+} in the Co 2p spectra (most likely forming Co_3O_4 after annealing).

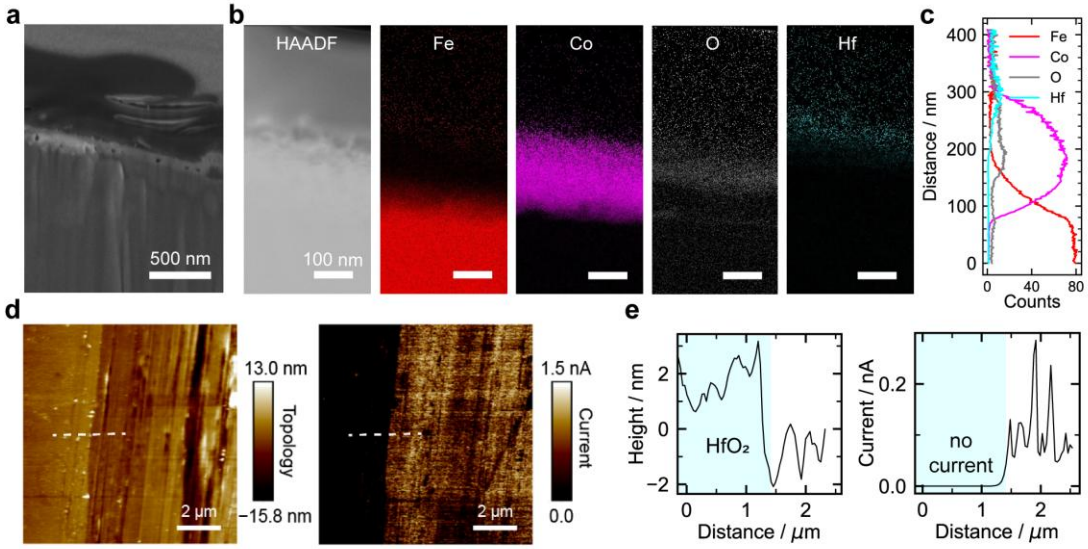

Figure 3.3 Cross-sectional SEM images of HfO_x-coated CoO_x anode and conductive AFM analysis

(a) Cross-sectional SEM image of the CoO_x anode with 2.5 nm of HfO_x coating and a PiperION topcoat. **(b)** HAADF-STEM images of HfO_x coated CoO_x anode with EDS elemental maps of Fe, Co, O, and Hf (scale bars = 100 nm). **(c)** Line-cut STEM-EDS plot of Fe, Co, O, and Hf elements illustrating the layers. **(d)** AFM height (left) and current map (right) of 2.5 nm of HfO_x on Pt/Ti on glass and **(e)** their corresponding line-cut plots.

Effect of passivation coating on Ir and Co system

PiperION, and other ionomers, are prone to oxidation when in contact with IrO_x at oxygen evolution potentials.[30,31] We started with metallic Ir as a model catalyst to investigate the role of HfO_x passivation layers in the oxidation process. Ir-based anodes, with HfO_x coatings of 0.8, 3.5, 4.8, and 12 nm thickness (calibrated based on thicknesses found on Si witness wafers placed in the same deposition process), were prepared and denoted as Ir-Hf0.8, Ir-Hf3.5, Ir-Hf4.8, and Ir-Hf12, respectively. The series of passivated anodes was evaluated in a 1 cm^2 AEMWE device. Before the electrodes were assembled in the single cell, a thin layer of PiperION was spray-coated on the anode surface as a topcoat with a loading of 0.1–0.2 $mg \cdot cm^{-2}$ to improve ionic contact with the bulk PiperION membrane. All AEMWE tests were conducted in the electrolyzer hardware at 56 ± 1 °C with pure-water feed, while the same cathode (Pt on carbon paper) and membrane (40-µm

PiperION) materials were used to investigate the effects of passivation coatings on anodes in the cell. The temperature and materials were selected based on previous AEMWE literature with pure-water feed[21,30,31] to establish a comparable model anode system to conventional nanoparticle-based anodes. The polarization curves obtained with uncoated and HfO_x-coated Ir-based anodes are shown in Figure 3.4a. Compared to the unpassivated Ir-based anode, labeled as Ir, the HfO_x-passivated anodes initially performed worse. This is likely because of the additional ionic resistance across HfO_x, leading to the cell voltage increasing by 0.8 V for the thickest 12 nm HfO_x at 500 $mA \cdot cm^{-2}$.

Electrochemical impedance spectroscopy (EIS) shows that the performance loss comes from an increase in apparent charge-transfer resistance with increasing HfO_x thickness, rather than high frequency resistance (Figure 3.4b). This suggests the HfO_x coatings led to a decrease in the active surface area of Ir catalysts, blocking the active sites and affecting the OER activity of Ir electrodes, as opposed to contributing additional ohmic resistance. However, the durability data at 500 $mA \cdot cm^{-2}$ shows different cell-voltage degradation behavior of uncoated and HfO_x-coated Ir electrodes (Figure 3.4c). While the Ir control electrode, without any passivation layer, degraded rapidly (increasing voltage by ~0.3 V in 1 h), the HfO_x passivated Ir anodes degraded slower even though they had higher initial cell voltages. After 40 h of AEMWE operation at 500 $mA \cdot cm^{-2}$, 3.5-nm-HfO_x-coated Ir had the lowest cell voltage of all Ir-devices tested. This result demonstrates the opportunity for durability improvement by implementing the passivation layers in the anode architecture. The Ir-Hf4.8 and Ir-Hf12 samples were operated at the lower current density of 200 $mA \cdot cm^{-2}$ and plotted in Figure B.4a because of their high resistivity of HfO_x coatings. Of the coatings tested here, 3.5 nm of ALD HfO_x was found to be the best.

Cycle stability tests were also performed on fresh Ir anodes with and without HfO_x passivation layers. The cell voltage was cycled between 0.6 V and 2.2 V, with a scan rate of 100 $mV \cdot s^{-1}$ to investigate the cell activation and degradation observed during the initial stages of the durability test (Figure B.5a and B.5d). Every 50 cycles, polarization and EIS data were obtained (Figure B.5). The Ir sample without passivation showed significant performance loss, likely attributed to anode ionomer and catalyst/ionomer interface degradation. In contrast, the Ir-Hf3.5 sample showed performance improvement throughout the cycling test as well as reduction in charge-transfer resistance. This data is consistent with the need to control the reactive catalyst/ionomer interface for durability.

In a second series of devices, the CoO_x on SS PTL annealed at 300 °C was compared to HfO_x-coated CoO_x anodes similarly prepared and tested as previously but with a narrower range of HfO_x thickness including 0.6, 1.1, 2.5, and 4.5 nm (CoO_x-Hf0.6, CoO_x -Hf1.1, CoO_x -Hf2.5, and CoO_x -Hf4.5). To improve catalyst-membrane contact and achieve better cell performance, we used a dip-coating method, adopted from the literature,[51] to coat the nanoplatelet CoO_x-based electrodes with PiperION ionomer, which led to a higher loading of ionomer at ~1 $mg \cdot cm^{-2}$. The effect of different ionomer topcoat preparation procedures is described in Figure B.6.

The polarization curves of the bare CoO_x, and those coated with HfO_x, were tested in small 1 cm^2 AEMWE cells (Figure 3.4d). As with the Ir-based electrodes, the bare CoO_x electrode initially performed best, and the HfO_x caused incremental increases in initial cell voltage with thickness. Analysis of the impedance spectra shows that HfO_x increases the initial charge-transfer resistance (Figure 3.4e). During the durability test at 1 $A \cdot cm^{-2}$, however, different cell voltage degradation rates (Figure 3.4f) were found. We decomposed the total cell voltage into anode and cathode contributions using a previously validated membrane-sensing reference electrode

technique[52] (Figure B.7 and Tables B.1 and B.2). While the anode voltage contributions were higher with the HfO_x-coated CoO_x electrodes than without the HfO_x coating, likely due to suppression of OER active sites requiring further interface engineering, the passivation layer did decrease the voltage degradation rate from 1.7 $mV \cdot h^{-1}$ for the uncoated sample to 0.7 $mV \cdot h^{-1}$ for CoO_x-Hf2.5.

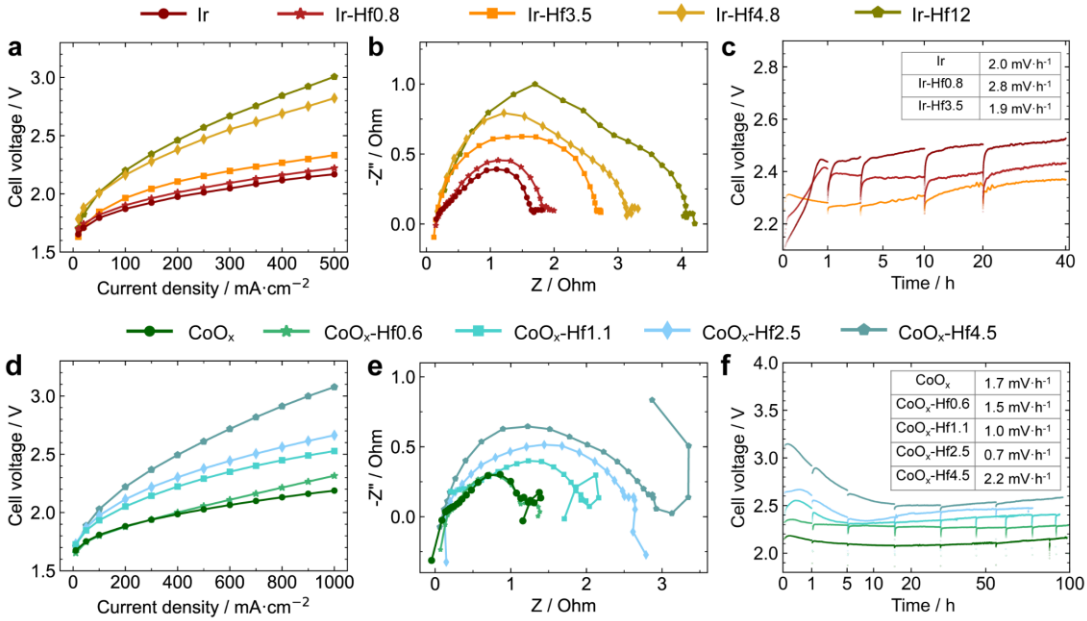

Figure 3.4 Electrochemical data of AEMWE devices with passivated anodes

(a) Polarization curves of AEMWE cells with uncoated and HfO_x-coated Ir-based anodes, **(b)** corresponding EIS curves at a current density of 50 $mA \cdot cm^{-2}$ applied, and **(c)** durability test at a current density of 500 $mA \cdot cm^{-2}$ applied at 56 °C with pure-water feed. Inset table summarizes cell voltage degradation rates from the last 20 h durability run. **(d)** Polarization curves of AEMWE cells with uncoated and HfO_x coated CoO_x-based anodes, **(e)** corresponding EIS curves at a current density of 50 $mA \cdot cm^{-2}$ applied, and **(f)** durability test at a current density of 1 $A \cdot cm^{-2}$ applied at 56 °C with pure water feed. Inset table summarizes cell voltage degradation rates from the last 50 h durability run. Ir samples were coated with ionomer using spray coating (~0.2 $mg \cdot cm^{-2}$ of loading). CoO_x-based samples were dip-coated with ionomer (loading ~1 $mg \cdot cm^{-2}$). Only one of each type of different device was fabricated for this set of data.

Conventional nanoparticle-based anodes (Co_3O_4) were also prepared and operated at 1 $A \cdot cm^{-2}$ for comparison (Figure B.8). The cell voltage degradation rate for the Co_3O_4 nanoparticle anode from the last 50 h was 2.3 $mV \cdot h^{-1}$, higher than any of the uncoated or HfO_x-coated CoO_x-

based electrodes, likely in part because the oxidative degradation is coupled to more-severe mechanical degradation for the powder catalyst-based electrodes.[21] Similar to the Ir-based electrode, AEMWE cycling tests on CoO_x anodes with and without the passivation layer were conducted (Figure B.9). The CoO_x electrode without the HfO_x coating had the cell voltage increase from 2.22 V to 2.30 V at 1 $A \cdot cm^{-2}$ before and after 300 cycles, while CoO_x-Hf2.5 had the cell voltage decrease from 2.41 V to 2.28 V at 1 $A \cdot cm^{-2}$. The passivation layer in this cycling experiment is likely stabilizing the interface and suppressing metal-oxide redox that may additionally contribute to interface morphological degradation on top of ionomer oxidation. The activation process with cycling is not fully understood.

Given the recent interest in KOH-fed AEMWE as a hybrid technology bridging conventional alkaline electrolysis with membrane technologies, selected anodes were tested in 0.1 M KOH at 75 °C (Figure B.10) and a current density of up to 2 $A \cdot cm^{-2}$. These conditions accelerate operative degradation modes. The passivated anodes showed higher initial operation voltages but lower degradation rates, consistent with improved anode durability. We note that compared to tests in pure-water at lower current, additional degradation modes besides those at the anode may be operative that must be isolated and further addressed. We also note that we tested ALD TiO_x as an alternative passivation material candidate along with HfO_x, finding the HfO_x more promising in our screening test (Figure B.11) in terms of ion-conducting (lower cell voltage) and electron insulating (less ionomer degradation) properties. Other than inorganic-based materials, of which there are likely many with similar roles to HfO_x, PTFE additives have been incorporated in anode catalyst layers as oxidative-resistant binders previously,[21] although ionic resistance from the non-ion-conducting PTFE led to poor performance.

Post-mortem analysis

XPS analysis was used to characterize the ionomer-related chemical species present before and after the durability tests at 500 $mA \cdot cm^{-2}$ for 40 h and at 1.0 $A \cdot cm^{-2}$ for 100 h for Ir and CoO_x samples, respectively. PiperION ionomer consists of a rigid aromatic carbon group, charged nitrogen and fluorinated carbon species. PiperION can be oxidized during AEMWE operation to lose charged nitrogen and fluorinated species and fragment the aromatic backbone (Figure 3.5a).[29,53]

XP C-1s, F-1s and N-1s spectra of pristine PiperION on the Ir anode before AEMWE operation (Figure 3.5b) were decomposed into component chemical species including C–C/C=C and C–N for the C1s spectrum, quaternary ammonium for the N1s spectrum, and fluorinated carbon for the F1s spectrum. After 500 $mA \cdot cm^{-2}$ for 40 h, a more intense O–C=O peak at higher binding energy was observed and the main carbon peak broadened, suggesting oxidation and partial loss of ionomer backbone carbon. For N1s and F1s spectra, no obvious charged nitrogen and fluorinated species were found for the uncoated Ir sample. HfO_x coatings on Ir samples (Ir-Hf0.8, Ir-Hf3.5) reduce the oxidation of carbon species after operation, as evident from the C1s spectra. The charged nitrogen and fluorine peaks are also still observed for both Ir-Hf0.8 and Ir-Hf3.5. Those peaks remain more intense as the thickness of HfO_x increases (Figure 3.5b). The sum of the XPS data shows that even under large oxidizing biases, the HfO_x passivation layer substantially protects the ionomer. After operation, a new broad peak also appears in the C1s spectra for the Ir sample at binding energies above 296 eV from Ir 4d, which indicates the ionomer topcoat on bare Ir was mostly oxidized and flushed away. In contrast, the signal in this region is much weaker with the HfO_x, suggesting retention of the ionomer and a stabilized interface.

Comparing a bare CoO_x electrode with a HfO_x-coated one after electrolyzer operation at 1.0 $A \cdot cm^{-2}$ for 100 h, the XP spectra show the suppression of ionomer degradation with HfO_x (Figure 3.5c). A less-intense oxidized carbon peak is shown in the C1s spectra for both CoO_x-Hf1.1 and CoO_x-Hf2.5 compared to bare CoO_x. More-intense signals were obtained for charged nitrogen and fluorine peaks from the HfO_x-coated CoO_x compared to the uncoated CoO_x, reflecting ionomer structures were better-retained with HfO_x passivation. All these results are consistent with the passivation layer functioning to block the oxidative damage to the ionomer. Noticeably, a large broad new peak was observed in the nominal F1s spectra in samples after electrolyzer operation at binding energies higher than 696 eV, which is in the Auger region of Co. The Co-Auger signal is suppressed when the HfO_x coating is present, indicating the ionomer and CoO_x catalyst layers were physically separated. From the XP spectra collected before and after electrolyzer testing, the relative areal ratios of oxidized carbon peaks to total carbon peaks in the C 1s spectrum and charged nitrogen and fluorine peaks to total carbon peak in each sample are calculated and listed in Table A.3. Ionomer oxidation is suppressed with HfO_x coatings in both Ir and CoO_x systems, respectively. In addition, even though there is no distinct trend observed in the ratio of N^+ or F over total C peaks with the thickness of HfO_x, the calculated ratios of N^+ or F over total C are higher when the electrode surface is coated with HfO_x.

Ir-4f and Co-2p XP spectra were also collected and compared. During the cell operation, metallic Ir is oxidized as evident from the shift of the Ir peaks to higher binding energies after operation (Figure 3.6a). The degree of this change differs somewhat with HfO_x coating thickness, yet all the films show oxidation of the Ir, consistent with the permeability of the thin HfO_x to OH^-. The CoO_x (Figure 3.6b), being already oxidized, are much less affected by cell operation having similar XP spectra for all samples. The Hf-4f spectra of Ir-Hf0.8, Ir-Hf3.5, CoO_x-Hf1.1, and CoO_x-

Hf2.5, show the HfO_x layers remain on the anodes even after the durability AEMWE cell test (Figure 3.6c). For comparison, the Hf 4f spectra of all samples before the cell operation are plotted in Figure B.12.

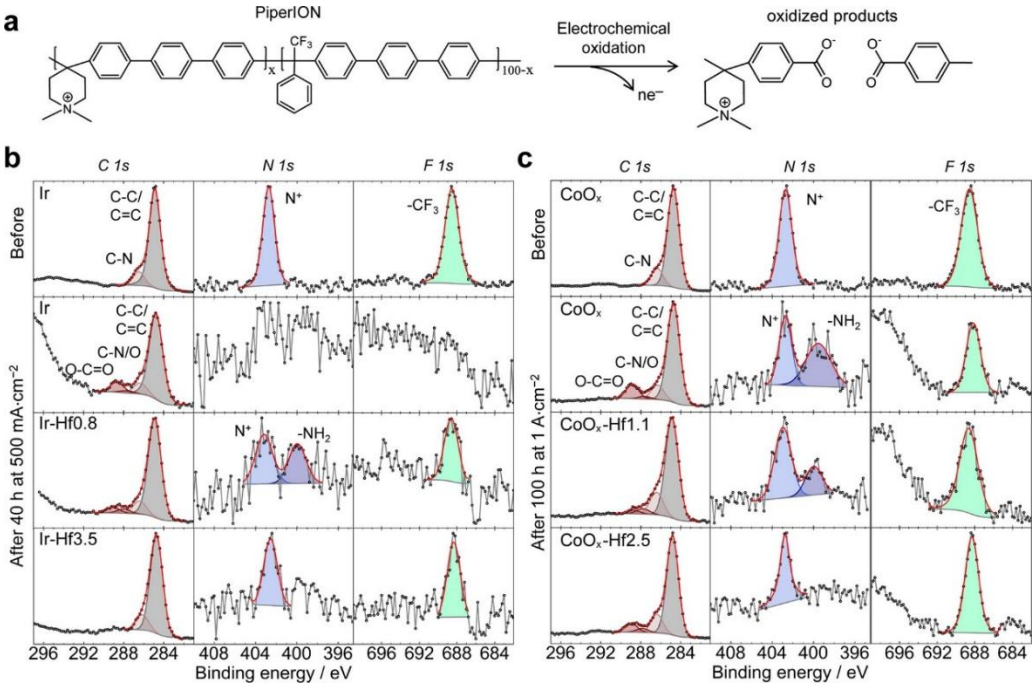

Figure 3.5 XPS analysis of operated anodes

(a) PiperION structure and its exemplified electrochemical degradation products due to oxidation. **(b)** XP spectra of C 1s, N 1s, and F 1s of Ir the sample before and after cell operation and Ir-Hf0.8 and Ir-Hf3.5 samples after cell operation (500 $mA \cdot cm^{-2}$, 40 h). **(c)** XP spectra of C 1s, N 1s, and F 1s of the CoO_x sample before and after cell operation and CoOx-Hf1.1 and CoOx-Hf2.5 samples after cell operation (1.0 $A \cdot cm^{-2}$, 100 h).

Because quantification is difficult with XPS, especially for the non-planar catalyst-coated PTLs studied here, we also used cross-sectional electron microscopy. The CoO_x-Hf2.5 anode after operating at 1.0 $A \cdot cm^{-2}$ for 100 h was characterized using FIB-SEM and HAADF-STEM/EDS (Figure 3.6d; compared to Figures 3.3a and 3.3b). In the cross-sectional view, ~200 nm of CoO_x is visible on the top of the SS surface, even after operation. High-resolution transmission-electron microscopy (HRTEM) analysis of the CoO_x layer shows lattice fringes probably corresponding Co_3O_4 (Figure B.13).

From elemental mapping, we observe that the SS PTL, CoO_x catalyst layer, and HfO_x passivation layer were largely preserved after 100 h of the electrolyzer testing at 1.0 $A \cdot cm^{-2}$. The EDS spectra of CoO_x-Hf2.5 sample were taken before and after the electrolyzer operation showing the Hf signal remained after operating in the harsh oxidative environment (Figure B.14). Importantly, the darker region (as marked in the SEM image of Figure 3.6d) is the ionomer layer which remains present after 100 h of electrolyzer test at 1.0 $A \cdot cm^{-2}$ (see EELS spectrum in Figure B.15). Furthermore, for Ir-Hf12 sample, where HfO_x is thick enough to substantially impede hydroxide transport, after operating the anode at lower current density, we still observe the HfO_x layer using SEM-EDS (Figure B.4b).

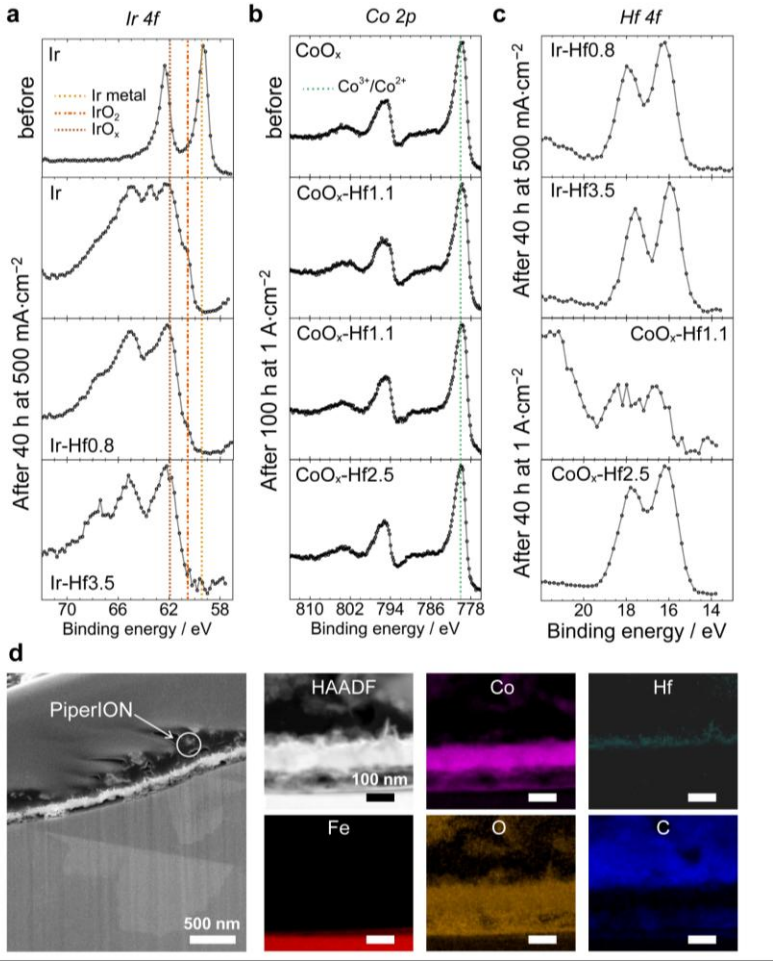

Figure 3.6 XPS analysis of operated anodes along with cross-sectional SEM/TEM images with EDS elemental maps

XPS spectra of **(a)** Ir-4f of the Ir sample before and after cell operation and Ir-Hf0.8 and Ir-Hf3.5 samples after cell operation (500 mA·cm^{-2}, 40 h), **(b)** Co 2p spectra of the CoO_x sample before and after cell operation and CoO_x-Hf1.1 and CoO_x -Hf2.5 samples after cell operation (1 A·cm^{-2}, 100 h), and **(c)** Hf 4f spectra of Ir-Hf0.8 and Ir-Hf3.5 samples after cell operation (500 mA·cm^{-2}, 40 h) and CoO_x-Hf1.1 and CoO_x-Hf2.5 samples after cell operation (1 A·cm^{-2}, 100 h). **(d)** Cross-sectional SEM image and HAADF-STEM images with EDS elemental maps of CoO_x-Hf2.5 sample operated at 1.0 A·cm^{-2} for 100 h (scale bars = 100 nm for elemental maps).

The behavior of HfO_x coatings on the Ir- and CoO_x-based anodes can be explained by the various hypothesized degradation mechanisms. There are often multiple reasons for voltage degradation, including: *i*) catalyst deactivation, dissolution, and detachment, *ii*) ionomer degradation and poisoning, *iii*) ion contamination, and *iv*) mechanical failure.[4,19] The most-dominant factor for IrO_x during the long-term test was probably ionomer oxidation, as reported previously.[31] Similarly, here we find ionomers are easily oxidized at the OER potential by Ir. When the Ir|ionomer interface is separated by HfO_x to form Ir|HfO_x|ionomer, less ionomer degradation occurs, and thus lower cell voltages and voltage degradation rates were observed. In contrast, CoO_x is a poor electrical conductor, and probably forms an interfacial oxyhydroxide spontaneously under operation. This appears to provide a more-stable interface with ionomer, and slower ionomer oxidation during operation. When we apply HfO_x on the CoO_x anode, the ionic and electrical resistances coming from HfO_x are relatively more important. Over longer time periods, slower degradation rates are still provided with the CoO_x|HfO_x|ionomer systems compared to CoO_x|ionomer. This result emphasizes the importance of interfacial engineering in AEMWE systems. However, we emphasize that conductive, metallic catalyst layers are obviously preferred in the porous electrode to reach the ultimate performance. However, as oxidation-resistant ionomers/membranes for AEMWE have not yet been developed, the ionomer-catalyst interface is prone to damage by oxidation from the catalyst. Conductive catalysts can both drive water

oxidation and ionomer oxidation more efficiently over their entire surface area. Thus, we need to improve the catalyst-ionomer interface to fully exploit conductive and efficient anode catalysts.

In addition to ionomer degradation, catalyst degradation by dissolution can occur during electrolyzer operation. Ir-based OER catalysts are known to slowly leach during operation, and dissolution rates are faster for oxidized metallic Ir compared to crystalline rutile IrO_2.[54-56] It is possible that the added HfO_x layers may protect and stabilize the surface of the Ir catalyst layer from dissolution, leading to lower cell voltage in durability test data. The CoO_x model catalyst we prepared here appears stable in its oxide form and may have less dissolution under OER conditions intrinsically,[57] thus being less affected by the presence of the HfO_x coatings. While the scope of this study is the role of passivation coatings in ionomer degradation, further study focused on catalyst degradation/dissolution using online inductively coupled plasma mass spectrometry (ICP-MS)[58,59] would be helpful to determine the role of HfO_x, or other, coatings in stabilizing catalyst layer specifically.

CONCLUSION

In summary, a new passivated anode for AEMWE has been developed where the OER catalysts are directly deposited on the GDLs, and the surface of the catalysts is protected with thin films of ion-permeable but electron-blocking metal oxide films, here ALD HfO_x. The best working thickness of HfO_x coating found here was ~2–3 nm, where the HfO_x layer is thin enough not to substantially limit the OH^- transport through the layer, but thick enough to form a continuous film so that the ionomer degradation is suppressed, and the desirable mechanical stability of the film is maintained. The total-cell voltage degradation was suppressed with the presence of HfO_x protective layers in the Ir-based system because of substantially lowered ionomer degradation and increased Ir layer stability at the anodes. For CoO_x-based anodes, although less ionomer

degradation is confirmed with XPS analysis, the resistivity of HfO_x increased the cell voltage for these model anodes. This work indicates that understanding and engineering the catalyst-ionomer interface is a promising and viable strategy to solve the limitations and problems in AEMWE development and additional work will apply these innovations to higher-surface-area catalysts designed for high-efficiency AEMWE. The concepts developed and employed here may also be useful for electrolyte-fed hybrid AWE/AEMWE systems.

EXPERIMENTAL METHODS

Preparation of catalyst layer

Stainless steel mesh (25AL3, Bekaert), a fiber-based porous substrate, was used as a gas diffusion layer / porous transport layer (PTL). Ir and Co metals were deposited on the steel PTL under ultra-high vacuum (~10^{-7} torr) using an electron-beam evaporator (Amod, Angstrom Engineering) as water oxidation catalyst that could be later coated with HfO_x passivating thin films. Ir metal was deposited at an applied power of ~30 % with a deposition rate no larger than 0.2 Å·s^{-1} and the final thickness was 75 nm. Similarly, Co metal was deposited at an applied power of ~6.5 %, and the final thickness was kept to 150 nm. To enhance the activity of catalysts, Co-on-steel PTL samples were thermally treated at temperature of 250–600 °C for 2 h in a box furnace in air to form surface oxides.

Preparation of HfO_x passivation coating

A HfO_x thin film was deposited on the catalyst layer with an atomic layer deposition system (Savannah, Ultratech) using tetrakis dimethylamido hafnium (TDMAHf) Hf precursor and water at 250 °C. The thickness of the HfO_x layer varied with the number of cycles of ALD deposition, and each cycle consists of consecutive pulse of water for 0.4 s and precursor TDMAHf for 0.015 s with an interval of 5 s between each pulse. Si wafers were used as bystander witness

samples inside the ALD chamber along with the experimental samples to analyze the thickness using an ellipsometer. For a TiO_x thin film, tetrakis dimethylamido titanium (TDMAT) was used as a Ti precursor, and all the deposition parameters were same except using TDMAT pulse for 0.1 s.

Material characterization

Grazing incidence X-ray diffraction (GIXRD) was performed to understand the phase of the prepared catalyst layer. Experiments were carried out on the thin films grown on the Si wafer using a Rigaku (SmartLab), which is equipped with Cu K-alpha radiation (1.54 Å) and Cu K-beta filter. GIXRD patterns were obtained in the 2-theta scan mode with a scan step size of 0.02 deg, and an incident angle of 0.5 deg with step time of 0.6 s per step. Ellipsometry measurements were conducted to calculate the thickness of HfO_x on the witness Si wafer that was put in the ALD chamber together with anode samples. Optical response from 240–1688 nm as obtained using a M-2000 spectroscopic ellipsometer (J.A. Woollam) and fit with a model of a dielectric film on a Si substrate.

HfO_x films were characterized with conductive atomic force microscopy (c-AFM) with a Dimension ICON with ScanAsyst (Bruker) to measure the topographical surface and insulating property with 1.0 V bias. Pt coated Ti/glass was used as a substrate, and HfO_x coated slides were electronically connected to the AFM stage after a scratch on the sample surface was made. Scanning electron microscopy (SEM) imaging was carried out to understand the surface of the electrodes using a Thermo Fisher HELIOS NANOLAB 600i equipped with EDS analyzer (Oxford Instruments). SEM characterization was performed at 5 kV with a working distance of 5.1- or 10.2-mm using ETD or TLD mode. Electrode structure and element distribution were analyzed in cross-section using SEM, TEM and HAADF-STEM/EDS mapping. Samples were cut using a focused

ion beam (FIB) and the lift outs were welded to a TEM grid. FIB-cut samples were cleaned for thinning to electron transparency so that they can be imaged in TEM (FEI Titan 80-200). X-ray photoelectron spectroscopy **(**XPS) characterizations were performed with an ESCALAB 250 (Thermo Scientific) using an Al Kα monochromated flood source with 20 eV pass energy and 500 μm spot size. The obtained spectra were analyzed with Avantage 5.99 software (Thermo Scientific). The binding energies were calibrated with the C 1s spectra where the main carbon peaks from all samples were shifted to 284.8 eV. The C 1s, N 1s and F 1s spectra were fitted with proper chemical moieties using the software.

Electrode preparation

Cathode PTLs for the electrolyzers were prepared as reported previously.[31] The catalyst ink solution was prepared by mixing 100 mg of nanocatalyst powder, 200 mg of 5 wt% TP-85 (also known as PiperION, Versogen), 1.5 g of milli-Q water and 1.7 g of isopropyl alcohol and sonicated until the desirable dispersion was obtained. Pt black (Fuel Cell Store) ink solution was spray-coated on carbon paper (Toray 090, Fuel Cell Store) to prepare cathode PTLs. During spraying, the substrates were heated on a hot plate at 80 °C to dry out the solvent. After 2–3 $mg \cdot cm^{-2}$ of catalyst loading was obtained, a thin ionomer top-coat was deposited by spraying 2 % PiperION solution. For control nanoparticle-based anode preparation, core/shell Ir/IrO_x and Co_3O_4 (Fuel Cell Store) ink solutions were prepared and sprayed over SS mesh in a similar way as in preparing the cathodes.

For the anodes, metallic Ir/Co or cobalt oxide was directly grown onto the steel PTLs by e-beam deposition, followed by thermal treatment when it was needed. The catalyst-coated PTLs were cut into 1.0 cm^2 electrodes and covered with PiperION topcoats by either spraying or dip-coating 2.0% ionomer solution. Ir-based electrodes were covered with PiperION topcoats by

spraying ionomer solution to get 0.1 to 0.2 mg·cm^{-2} of ionomer loading (after drying on the hot plate at 80 °C). For CoO_x-based anodes, samples were dipped 5 or 6 times in 2% PiperION solution to add ionomer topcoats. For dip-coating, only the catalyst-deposited side of the PTLs was horizontally dipped into the ionomer solution and then dried on a hot plate at 80 °C. The ionomer topcoat loading was calculated from the mass difference of PTLs before and after dip coating as 1.0 ± 0.2 mg·cm^{-2}.

Membrane electrode assemblies (MEAs)

Electrolyzer single cells were assembled according to the literature[30] where preconditioned AEM (40 μm thick PiperION, also known as TP-85, Versogen) was placed in between 1 cm^2 sized cathode and anode electrodes and compressed in flow fields and bipolar plates. High-purity water (18.2 MΩ·cm) was supplied to both anode and cathode from a water tank, which was heated at 62 °C to obtain the actual cell temperature of 56 ± 1 °C. When operating with KOH, a KOH bath was heated at 83 °C and the cell hardware was heated to 75 ± 1 °C with an external insertion heater. The 0.1 M KOH was supplied to the cell as an anolyte. To incorporate a membrane-potential-sensing probe in the AEMWE cell,[3] a 7.5 cm long membrane strip (TP-85) was overlapped with the AEM in the electrolyzer, but outside of 1.0 cm^2 active surface area, and extended to outside of the electrolyzer hardware. A compartment was set up using an O-ring and glass tube on the membrane strip, and a Hg/HgO reference electrode was placed inside the glass tube in 0.10 M KOH to make electrolyte contact between the membrane strip and the reference electrode. The potentials of both anode and cathode as a function of current were determined using this membrane-sensing technique.

AEMWE single cell testing

Electrolyzer performance was measured with a potentiostat (BioLogic VSP-300) equipped

with a 10 A/5 V booster. To break in the cell, the current was stepped from 100 mA·cm^{-2} to 1 A·cm^{-2} with an interval of 100 mA·cm^{-2}. At each step, the current was held for 2 min. To investigate individual cell resistances, for example, contact resistance, anodic and cathodic charge-transfer resistances, etc., impedance was measured with a frequency range of 1 MHz to 100 mHz at 50 mA·cm^{-2}. The current-voltage performance curve was then obtained starting with applying a constant current of 1A·cm^{-2} for 2 min, then the current was decreased to 900, 800, ⋯, 200, 100, 50 and 10 mA·cm^{-2} and held for 10 s for each step. For some samples, the maximum applied current was 500 mA·cm^{-2} to minimize severe electrode degradation. After the performance measurement, the cell was held at either 500 mA·cm^{-2} or 1 A·cm^{-2} for a specific amount of time as a long-term durability test. A cycle stability test was conducted by sweeping a voltage between 0.6 V and 2.2 V with a scan rate of 100 mV·s^{-1}. After each 50 cycles, polarization and EIS data were obtained using the same procedures.

When operating with KOH, the cell was stepped up to 2 A·cm^{-2} for initial break-in and polarization curve measurements, and the cell was held at 2 A·cm^{-2} for the durability run. After electrolyzer operation, the cells were disassembled, and anode electrodes were separately treated for post-mortem XPS analysis. The electrodes were washed with DI water and soaked in 3 M aq. NaCl to ion-exchange the ionomer from hydroxide form to Cl^- form, to minimize the ionomer degradation by OH^-attack while drying. Later, the anodes were washed with DI water to remove residual NaCl salts from the surface and dried in air.

Membrane sensing

In addition to conventional lab-scale AEMWE single cell, a membrane sensing system was used to separate the total cell voltage into the cathodic and anodic contributions.[52] A strip of the membrane was extended from the MEA to the outside of the cell and was coupled with a

Hg/HgO reference electrode in 0.1 M KOH. The voltage was measured from the strip to the anode and the strip to the cathode, respectively, without interruption of the total cell voltage measurement. To achieve reliable long-term durability data with the integrated reference-electrode system, the sensing membrane strip was kept hydrated, and the concentration of 0.1 M KOH was kept the same during the measurement. Using this membrane sensing, the anode and cathode voltage contributions as well as anode and cathode voltage-degradation rates were deconvoluted during the durability tests. All the voltage degradation rate was calculated by a linear regression of data points from the last 20 h for Ir system and 50 h for CoO_x system in durability tests.

BRIDGE

Chapter III conceptualizes passivated anodes in AEMWE, where nanoscale metal oxide films at catalyst-ionomer interfaces act as electron-blocking but ion-conducting layers, suppressing the electrochemical oxidation of ionomers. This enables further investigation of passivation materials that can extend the lifetime of AEMWE anodes.

REFERENCES

(1) Ayers, K. E.; Anderson, E. B.; Capuano, C.; Carter, B.; Dalton, L.; Hanlon, G.; Manco, J.; Niedzwiecki, M. Research Advances towards Low Cost, High Efficiency PEM Electrolysis. *ECS Transactions* **2010**, *33* (1), 3-3.

(2) Carmo, M.; Fritz, D. L.; Mergel, J.; Stolten, D. A Comprehensive Review on PEM Water Electrolysis. *Int. J. Hydrogen Energy* **2013**, *38* (12), 4901-4934.

(3) Evich, M. G.; Davis, M. J. B.; McCord, J. P.; Acrey, B.; Awkerman, J. A.; Knappe, D. R. U.; Lindstrom, A. B.; Speth, T. F.; Tebes-Stevens, C.; Strynar, M. J.; et al. Per- and Polyfluoroalkyl Substances in the Environment. *Science* **2022**, *375* (6580), 9065-9065.

(4) Li, D.; Motz, A. R.; Bae, C.; Fujimoto, C.; Yang, G.; Zhang, F. Y.; Ayers, K. E.; Kim, Y. S. Durability of Anion Exchange Membrane Water Electrolyzers. *Energy and Environmental Science* **2021**, *14* (6), 3393-3419.

(5) Ehlers, J. C.; Feidenhans'l, A. A.; Therkildsen, K. T.; Larrazábal, G. O. Affordable Green Hydrogen from Alkaline Water Electrolysis: Key Research Needs from an Industrial Perspective. *ACS Energy Lett.* **2023**, *8* (3), 1502-1509.

(6) Vincent, I.; Bessarabov, D. Low Cost Hydrogen Production by Anion Exchange Membrane Electrolysis: A Review. *Renew. Sustain. Energy Rev.* **2018**, *81*, 1690-1704.

(7) Leng, Y.; Chen, G.; Mendoza, A. J.; Tighe, T. B.; Hickner, M. A.; Wang, C.-Y. Solid-State Water Electrolysis with an Alkaline Membrane. *J. Am. Chem. Soc.* **2012**, *134* (22), 9054-9057.

(8) Henkensmeier, D.; Najibah, M.; Harms, C.; Žitka, J.; Hnát, J.; Bouzek, K. Overview: State-of-the Art Commercial Membranes for Anion Exchange Membrane Water Electrolysis. *Journal of Electrochemical Energy Conversion and Storage* **2020**, *18* (2).

(9) Mardle, P.; Chen, B.; Holdcroft, S. Opportunities of Ionomer Development for Anion-Exchange Membrane Water Electrolysis. *ACS Energy Lett.* **2023**, *8* (8), 3330-3342.

10) Li, D.; Park, E. J.; Zhu, W.; Shi, Q.; Zhou, Y.; Tian, H.; Lin, Y.; Serov, A.; Zulevi, B.; Baca, E. D.; et al. Highly Quaternized Polystyrene Ionomers for High Performance Anion Exchange Membrane Water Electrolysers. *Nat. Energy.* **2020**, *5* (5), 378-385.

(11) Kang, S. Y.; Park, J. E.; Jang, G. Y.; Kim, O.-H.; Kwon, O. J.; Cho, Y.-H.; Sung, Y.-E. High-Performance and Durable Water Electrolysis Using a Highly Conductive and Stable Anion-Exchange Membrane. *Int. J. Hydrogen Energy* **2022**, *47* (15), 9115-9126.

(12) Chen, N.; Jiang, Q.; Song, F.; Hu, X. Robust Piperidinium-Enriched Polystyrene Ionomers for Anion Exchange Membrane Fuel Cells and Water Electrolyzers. *ACS Energy Lett.* **2023**, *8* (10), 4043-4051.

(13) Song, W.; Peng, K.; Xu, W.; Liu, X.; Zhang, H.; Liang, X.; Ye, B.; Zhang, H.; Yang, Z.; Wu, L.; et al. Upscaled Production of an Ultramicroporous Anion-Exchange Membrane Enables Long-Term Operation in Electrochemical Energy Devices. *Nat. Commun.* **2023**, *14* (1), 2732.

(14) Gong, M.; Li, Y.; Wang, H.; Liang, Y.; Wu, J. Z.; Zhou, J.; Wang, J.; Regier, T.; Wei, F.; Dai, H. An Advanced Ni–Fe Layered Double Hydroxide Electrocatalyst for Water Oxidation. *J. Am. Chem. Soc.* **2013**, *135* (23), 8452-8455.

(15) Jeon, S. S.; Lim, J.; Kang, P. W.; Lee, J. W.; Kang, G.; Lee, H. Design Principles of NiFe-Layered Double Hydroxide Anode Catalysts for Anion Exchange Membrane Water Electrolyzers. *ACS Appl. Mater. Interfaces* **2021**, *13* (31), 37179-37186.

(16) Choi, W.-S.; Jang, M. J.; Park, Y. S.; Lee, K. H.; Lee, J. Y.; Seo, M.-H.; Choi, S. M. Three-Dimensional Honeycomb-Like $Cu_{0.81}Co_{2.19}O_4$ Nanosheet Arrays Supported by Ni Foam and Their High Efficiency as Oxygen Evolution Electrodes. *ACS Appl. Mater. Interfaces* **2018**, *10* (45), 38663-38668.

(17) Chen, D.; Park, Y. S.; Liu, F.; Fang, L.; Duan, C. Hybrid Perovskites as Oxygen Evolution Electrocatalysts for High-Performance Anion Exchange Membrane Water Electrolyzers. *Chemical Engineering Journal* **2023**, *452*, 139105-139105.

(18) Zheng, Y.; Serban, A.; Zhang, H.; Chen, N.; Song, F.; Hu, X. Anion Exchange Ionomers Enable Sustained Pure-Water Electrolysis Using Platinum-Group-Metal-Free Electrocatalysts. *ACS Energy Lett.* **2023**, 5018-5024.

(19) Xu, Q.; Zhang, L.; Zhang, J.; Wang, J.; Hu, Y.; Jiang, H.; Li, C. Anion Exchange Membrane Water Electrolyzer: Electrode Design, Lab-Scaled Testing System and Performance Evaluation. *EnergyChem* **2022**, *4* (5), 100087.

(20) Lee, S. A.; Kim, J.; Kwon, K. C.; Park, S. H.; Jang, H. W. Anion Exchange Membrane Water Electrolysis for Sustainable Large-Scale Hydrogen Production. *Carbon Neutralization* **2022**, *1* (1), 26-48.

(21) Lindquist, G. A.; Gaitor, J. C.; Thompson, W. L.; Brogden, V.; Noonan, K. J. T.; Boettcher, S. W. Oxidative instability of ionomers in hydroxide-exchange-membrane water electrolyzers. *Energy Environ. Sci.* **2023**, 4373-4387.

(22) Andrew, W. T.; Jason, K. L.; Jason, R. S.; Nemanja, D.; Adam, Z. W.; Xiong, P. Design and Operating Principles for High-Performing Anion Exchange Membrane Water Electrolyzers. *J. Power Sources* **2023**, *567*, 232967.

(23) Enapter. Enapter AG Unveils the World's First Megawatt-Class AEM Electrolyser. https://www.enapter.com/newsroom/enapter-ag-unveils-the-worlds-first-megawatt-class-aem-electrolyser

(24) Zhang, L.; Xu, Q.; Hu, Y.; Chen, L.; Jiang, H. Benchmarking the pH–Stability Relationship of Metal Oxide Anodes in Anion Exchange Membrane Water Electrolysis. *ACS Sustainable Chemistry & Engineering* **2023**, *11* (36), 13251-13259.

(25) Joseph Steven, L.; Sanggyu, K.; Hyun-Seok, C.; Chang-Hee, K.; Sirivatch, S. Impacts of Manifold Geometry and Flow Configuration on Shunt Current, Current Distributions, and Crossover in an Alkaline Electrolysis Stack. *ECS Meeting Abstracts* **2022**, *MA2022-01* (38), 1696.

(26) Ashraf; Jinlei, H.; Kensaku, N.; Yoshiyuki, K.; Yoshinori, N.; Akihiro, K.; Takaaki, N.; Takuto, A.; Shigenori, M. Effects of operation and shutdown parameters and electrode materials on the reverse current phenomenon in alkaline water analyzers. *J. Power Sources* **2022**, *535*, 231454.

(27) Uchino, Y.; Kobayashi, T.; Hasegawa, S.; Nagashima, I.; Sunada, Y.; Manabe, A.; Nishiki, Y.; Mitsushima, S. Relationship Between the Redox Reactions on a Bipolar Plate and Reverse Current After Alkaline Water Electrolysis. *Electrocatalysis* **2018**, *9* (1), 67-74.

(28) Hydrogen Production Cost by AEM Water Electrolysis. https://ionomr.com/the-solutions-center/

(29) Li, D.; Matanovic, I.; Lee, A. S.; Park, E. J.; Fujimoto, C.; Chung, H. T.; Kim, Y. S. Phenyl Oxidation Impacts the Durability of Alkaline Membrane Water Electrolyzer. *ACS Applied Materials and Interfaces* **2019**, *11* (10), 9696-9701.

(30) Lindquist, G. A.; Oener, S. Z.; Krivina, R.; Motz, A. R.; Keane, A.; Capuano, C.; Ayers, K. E.; Boettcher, S. W. Performance and Durability of Pure-Water-Fed Anion Exchange Membrane Electrolyzers Using Baseline Materials and Operation. *ACS Appl. Mater. Interfaces* **2021**, *13* (44), 51917-51924.

(31) Krivina, R. A.; Lindquist, G. A.; Beaudoin, S. R.; Stovall, T. N.; Thompson, W. L.; Twight, L. P.; Marsh, D.; Grzyb, J.; Fabrizio, K.; Hutchison, J. E.; et al. Anode Catalysts in Anion-Exchange-Membrane Electrolysis without Supporting Electrolyte: Conductivity, Dynamics, and Ionomer Degradation. *Adv. Mater.* **2022**, *34* (35).

(32) Bhardwaj, A. A.; Vos, J. G.; Beatty, M. E. S.; Baxter, A. F.; Koper, M. T. M.; Yip, N. Y.; Esposito, D. V. Ultrathin Silicon Oxide Overlayers Enable Selective Oxygen Evolution from Acidic and Unbuffered pH-Neutral Seawater. *ACS Catal.* **2021**, *11* (3), 1316-1330.

(33) Esposito, D. V. Membrane-Coated Electrocatalysts—An Alternative Approach To Achieving Stable and Tunable Electrocatalysis. *ACS Catal.* **2018**, *8* (1), 457-465.

(34) Maeda, K.; Teramura, K.; Lu, D.; Saito, N.; Inoue, Y.; Domen, K. Noble-Metal/Cr_2O_3 Core/Shell Nanoparticles as a Cocatalyst for Photocatalytic Overall Water Splitting. *Angew. Chem. Int. Ed.* **2006**, *45* (46), 7806-7809.

(35) Finke, C. E.; Omelchenko, S. T.; Jasper, J. T.; Lichterman, M. F.; Read, C. G.; Lewis, N. S.; Hoffmann, M. R. Enhancing the Activity of Oxygen-Evolution and Chlorine-Evolution Electrocatalysts by Atomic Layer Deposition of TiO_2. *Energy Environ. Sci.* **2019**, *12* (1), 358-365.

(36) Marichy, C.; Ercolano, G.; Caputo, G.; Willinger, M. G.; Jones, D.; Rozière, J.; Pinna, N.; Cavaliere, S. ALD SnO_2 Protective Decoration Enhances the Durability of a Pt Based Electrocatalyst. *J. Mater. Chem. A* **2016**, *4* (3), 969-975.

(37) Tran-Phu, T.; Chen, H.; Daiyan, R.; Chatti, M.; Liu, B.; Amal, R.; Liu, Y.; Macfarlane, D. R.; Simonov, A. N.; Tricoli, A. Nanoscale TiO_2 Coatings Improve the Stability of an Earth-Abundant Cobalt Oxide Catalyst during Acidic Water Oxidation. *ACS Applied Materials and Interfaces* **2022**.

(38) Vos, J. G.; Wezendonk, T. A.; Jeremiasse, A. W.; Koper, M. T. M. MnO_x/IrO_x as Selective Oxygen Evolution Electrocatalyst in Acidic Chloride Solution. *J. Am. Chem. Soc.* **2018**, *140* (32), 10270-10281.

(39) Obata, K.; Takanabe, K. A Permselective CeO_x Coating To Improve the Stability of Oxygen Evolution Electrocatalysts. *Angew. Chem.* **2018**, *130* (6), 1632-1636.

(40) Ramasamy, H. V.; Sinha, S.; Park, J.; Gong, M.; Aravindan, V.; Heo, J.; Lee, Y.-S. Enhancement of Electrochemical Activity of Ni-rich $LiNi_{0.8}Mn_{0.1}Co_{0.1}O_2$ by Precisely Controlled Al_2O_3 Nanocoatings via Atomic Layer Deposition. *J. Electrochem. Sci. Technol.* **2019**, *10* (2), 196-205.

(41) Kazyak, E.; Chen, K.-H.; Chen, Y.; Cho, T. H.; Dasgupta, N. P. Enabling 4C Fast Charging of Lithium-Ion Batteries by Coating Graphite with a Solid-State Electrolyte. *Adv. Energy Mater.* **2022**, *12* (1), 2102618-2102618.

(42) Kaufmann, I. R.; Pick, A.; Pereira, M. B.; Boudinov, H. Metal-insulator-SiC Schottky structures using HfO_2 and TiO_2 dielectrics. *Thin Solid Films* **2017**, *621*, 184-187.

(43) Li, M.; Jin, Z. X.; Zhang, W.; Bai, Y. H.; Cao, Y. Q.; Li, W. M.; Wu, D.; Li, A. D. Comparison of Chemical Stability and Corrosion Resistance of Group IV Metal Oxide Films Formed by Thermal and Plasma-Enhanced Atomic Layer Deposition. *Scientific Reports* **2019**, *9* (1).

(44) Chen, L.; Xu, Q.; Oener, S. Z.; Fabrizio, K.; Boettcher, S. W. Design Principles for Water Dissociation Catalysts in High-Performance Bipolar Membranes. *Nat. Commun.* **2022**, *13* (1), 3846.

(45) Kosmulski, M. Attempt to Determine Pristine Points of Zero Charge of Nb_2O_5, Ta_2O_5, and HfO_2. *Langmuir* **1997**, *13*, 6315-6320.

(46) Janusz, W. The Electrical Double Layer Parameters for the Group 4 Metal Oxide/Electrolyte System. *Adsorpt. Sci. Technol.* **2000**, *18*, 117-134.

(47) Ritala, M.; Leskelä, M.; Niinistö, L.; Prohaska, T.; Friedbacher, G.; Grasserbauer, M. Development of Crystallinity and Morphology in Hafnium Dioxide Thin Films Grown by Atomic Layer Epitaxy. *Thin Solid Films* **1994**, *250* (1), 72-80.

(48) Hausmann, D. M.; Kim, E. H.; Becker, J. S.; Gordon, R. G. Atomic Layer Deposition of Hafnium and Zirconium Oxides Using Metal Amide Precursors. *Chem. Mater.* **2002**, *14*, 4350-4358.

(49) Chia-Hung, C.; Chien-Te, H.; Wen-Jie, K.; Li-Wei, L.; Yeou-Fu, L.; Hao-Wei, L.; Siyong, G.; Chun-Chieh, F.; Ruey-Shin, J.; Bikash Chandra, M.; et al. Roll-to-roll Atomic Layer Deposition of Titania Coating on Polymeric Separators for Lithium-Ion Batteries. *J. Power Sources* **2021**, *482*, 228896.

(50) Chang, N. L.; Poduval, G. K.; Sang, B.; Khoo, K.; Woodhouse, M.; Qi, F.; Dehghanimadvar, M.; Li, W. M.; Egan, R. J.; Hoex, B. Techno-Economic Analysis of the Use of Atomic Layer Deposited Transition Metal Oxides in Silicon Heterojunction Solar Cells. *Prog. Photovolt.* **2023**, *31* (4), 414-428.

(51) Xiao, J.; Oliveira, A. M.; Wang, L.; Zhao, Y.; Wang, T.; Wang, J.; Setzler, B. P.; Yan, Y. Water-Fed Hydroxide Exchange Membrane Electrolyzer Enabled by a Fluoride-Incorporated Nickel-Iron Oxyhydroxide Oxygen Evolution Electrode. *ACS Catal.* **2021**, *11* (1), 264-270.

(52) Xu, Q.; Oener, S. Z.; Lindquist, G.; Jiang, H.; Li, C.; Boettcher, S. W. Integrated Reference Electrodes in Anion-Exchange-Membrane Electrolyzers: Impact of Stainless-Steel Gas-Diffusion Layers and Internal Mechanical Pressure. *ACS Energy Lett.* **2021**, *6* (2), 305-312.

(53) Krivina, R. A.; Lindquist, G. A.; Yang, M. C.; Cook, A. K.; Hendon, C. H.; Motz, A. R.; Capuano, C.; Ayers, K. E.; Hutchison, J. E.; Boettcher, S. W. Three-Electrode Study of Electrochemical Ionomer Degradation Relevant to Anion-Exchange-Membrane Water Electrolyzers. *ACS Applied Materials and Interfaces* **2022**, *14* (16), 18261-18274.

(54) Kasian, O.; Grote, J.-P.; Geiger, S.; Cherevko, S.; Mayrhofer, K. J. J. The Common Intermediates of Oxygen Evolution and Dissolution Reactions during Water Electrolysis on Iridium. *Angew. Chem.* **2018**, *130* (9), 2514-2517.

(55) Lončar, A.; Escalera-López, D.; Cherevko, S.; Hodnik, N. Inter-Relationships between Oxygen Evolution and Iridium Dissolution Mechanisms. *Angew. Chem. Int. Ed.* **2022**, *61*.

(56) Geiger, S.; Kasian, O.; Ledendecker, M.; Pizzutilo, E.; Mingers, A. M.; Fu, W. T.; Diaz-Morales, O.; Li, Z.; Oellers, T.; Fruchter, L.; et al. The stability number as a metric for electrocatalyst stability benchmarking. *Nat. Catal.* **2018**, *1* (7), 508-515.

(57) Kreider, M. E.; Burke Stevens, M. Material Changes in Electrocatalysis: An In Situ/Operando Focus on the Dynamics of Cobalt-Based Oxygen Reduction and Evolution Catalysts. *ChemElectroChem* **2023**, *10* (3), e202200958.

(58) Krivina, R. A.; Zlatar, M.; Stovall, T. N.; Lindquist, G. A.; Escalera-López, D.; Cook, A. K.; Hutchison, J. E.; Cherevko, S.; Boettcher, S. W. Oxygen Evolution Electrocatalysis in Acids: Atomic Tuning of the Stability Number for Submonolayer IrO_x on Conductive Oxides from Molecular Precursors. *ACS Catal.* **2023**, *13* (2), 902-915.

(59) Schalenbach, M.; Kasian, O.; Ledendecker, M.; Speck, F. D.; Mingers, A. M.; Mayrhofer, K. J. J.; Cherevko, S. The Electrochemical Dissolution of Noble Metals in Alkaline Media. *Electrocatalysis* **2018**, *9* (2), 153-161.

CHAPTER IV

FLEXIBLE HAFNIUM(EG) COATINGS FOR IMPROVED PERFORMANCE AND DURABILITY OF PURE-WATER-FED ALKALINE MEMBRANE ELECTROLYZERS

This chapter includes unpublished co-authored work with Sharmistha Bhattacharjee, Nicholas Strandwitz, and Shannon W. Boettcher. M.K. and S.W.B. designed the experiment and led the project. M.K. collected electrolyzer data and conducted materials characterization. S.B. prepared atomic/molecular layer deposition layers. M.K. wrote the chapter.

INTRODUCTION

Solid-electrolyte interfaces play an important role in the performance and lifetime of many electrochemical devices. In batteries, specifically, efforts have been made to engineer stable interfaces by building nano-scale passivation layers or generating them during operation to modulate electronic and ionic processes, often forming Li^+ ion conducting but electron-insulating passivation layer.[1-3] These approaches can be adopted in water electrolysis devices, where solid-electrolyte interfaces are important to enable electron and ion transportation and evolving product gas.[4,5] Common failure mechanisms in the systems include catalyst dissolution, catalyst detachment, and degradation of polymeric electrolytes, ionomers.[6-9] Especially for AEMWE, ionomers are easily oxidized at oxidative potentials, losing their ability to transport OH^- near to the surface of oxygen evolving catalysts.[8-10] Previously, we conceptualized the deployment of nanoscale HfO_x thin films using atomic layer deposition (ALD) for anodes to minimize unwanted

side reactions and stabilize the ionomer-catalyst interface.[11] Also, there are several other literatures using ALD technique in water electrolysis systems to minimize side reactions and maintain the device performance.[12-14]

On the other hand, nano-scale thin films can be further optimized to enhance the performance and durability of porous electrodes. Instead of using water as an oxidizing source for ALD, molecular linker can be employed in molecular layer deposition (MLD). For example, as opposed to ALD HfO_x, MLD Hf(EG) can be deposited via alternative pulses of a metal precursor, tetrakis(dimethylamido)hafinium, and ethylene glycol (EG) as a linker.[15,16] While maintaining key characteristics of ALD coatings (i.e., film uniformity, conformality, and precise thickness control), MLD coatings have additional advantages, including tunable porosity and flexibility due to incorporated organic linkers.[17-19] The controlled porosity of MLD coatings is expected to facilitate ion transport, enabling the oxygen evolution reaction without compromising the device performance, compared to ALD coatings. Additionally, their inherent flexibility allows a better adaptation to the underlaying catalyst layer, particularly in accommodating significant volume expansion during surface reconstruction, unlike the more rigid ALD coatings.[17] While the novel properties of MLD bring those new functionalities, the fundamental roles of the passivation layer in AEMWE are expected to remain unchanged, as it continues to regulate catalyst dissolution and ionomer oxidation at the catalyst-ionomer interfaces.

In this work, we systematically controlled the thickness of MLD Hf(EG) coatings on the $Co(OH)_x$ oxygen evolving catalyst layer and evaluated their impact on the AEMWE cell performance and durability. While Hf(EG) layers thicker than 20 nm acted as significant electrical resistors, they effectively slowed down ionomer oxidation and catalyst dissolution, stabilizing the reconstructed active $CoO_x(OH)_y$ phase longer for an extended lifetime. As a result the cell voltage

degradation rate was ~ 8 times lower compared to the unpassivated $Co(OH)_x$ anode. X-ray photoelectron spectroscopy and online inductively coupled plasma mass spectrometry analyses confirmed that the Hf(EG) coatings successfully passivated the catalyst surface, minimizing ionomer oxidation, catalyst dissolution, and catalyst particle detachment during the operation. This approach provides new insights to fine-tune catalyst-ionomer interfacial processes, ultimately enhancing the performance and durability of pure water fed-AEMWE systems to meet commercialization standards.

RESULTS AND DISCUSSION

Synthesis and characterization of passivated anodes

A $Co(OH)_x$ catalyst layer was deposited onto a porous transport layer using hydrothermal synthesis (see details in Chapter II), followed by a molecular layer deposition technique to prepare nano-scale Hf(EG) thin films. The number of repetitive cycles of tetrakis(dimethylamido)hafinium and ethylene glycol pulses was controlled to obtain certain thickness of Hf(EG) films onto $Co(OH)_x$ layers. The growth rate of Hf(EG) was 0.78-0.94 Å per cycle (Figure C.1). When assembled in an AEMWE cell as an anode, an ionomer topcoat was applied to reduce ionic resistances between prepared passivated catalyst layers and bulk membranes (Figure 4.1a). This electrode design was intended to encapsulate $Co(OH)_x$ layers with Hf(EG) coatings, thereby mitigating undesirable ionomer oxidation and catalyst dissolution, while maintaining relatively good OER activity (Figure 4.1b). As an example of Hf(EG) coated anodes, cross-sectional scanning electron microscope (SEM) images of a 47-nm-thick-Hf(EG)-coated $Co(OH)_x$ electrode are presented in Figure 4.1c. The SEM image and elemental maps of *region 1* reveal a thick Hf(EG) layer covering the nanoneedle-structured catalyst surface, with a thickness similar to that

measured using optical ellipsometry on a Si wafer after the same deposition process. The elemental map of Hf M edge of *region 2* indicates that the Hf(EG) coating was not deposited on the compact $Co(OH)_x$ layer, as the MLD precursors could not penetrate through the layer.

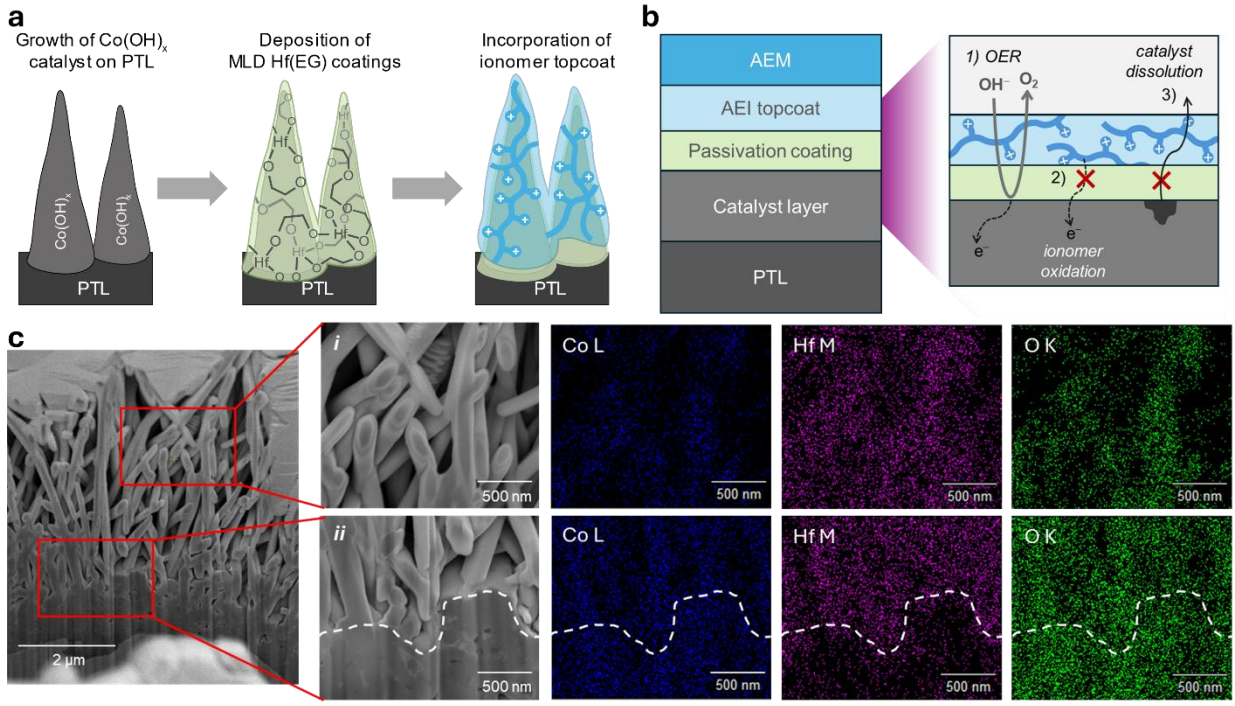

Figure 4.1 Scheme of process steps for passivated anodes and their functions in AEM device along with SEM images

Scheme of **(a)** fabrication steps and **(b)** interfacial reactions at engineered anode-AEI/AEM interface. Deposited passivation coatings regulate interfacial reactions; transporting hydroxide ions to generate oxygen molecules, suppressing ionomer oxidation, and prevent catalyst dissolution or detachment. **(c)** Cross-sectional SEM images of 47-nm-thick-Hf(EG)-coated $Co(OH)_x$ anode and corresponding EDX elemental maps. A comparison of Hf M edge maps between *region 1* ($Co(OH)_x$ nanoneedles) and *region 2* (compact $Co(OH)_x$ layer) shows how deep the precursor molecules can penetrate through nanoneedle structures and form thick-conformal Hf(EG) films.

Comparison between ALD and MLD

While ALD coatings have been widely used in many electrochemical devices to protect active materials from undesirable side reactions in porous electrodes, MLD has been much less explored. In our water electrolysis system, rigid ALD films can encapsulate the anode catalyst surface minimizing prevalent catalyst/ionomer degradation; however, when these films are too

thick, they can obstruct hydroxide ion transport and impede an anodic reaction. Previous study has suggested that 2-3 nm of HfO_x coatings enhances electrode lifetime in the device without compromising OER performance.[11] We expect that ion-permeating MLD coatings could have similar functionality but allow a thicker layer, potentially extending the lifetime of anodes (Figure 4.2a). Here we compare how ALD and MLD coatings modulate related electrochemical reactions in water electrolysis. A $Co(OH)_x$ coated PTL was chosen as a model anode, and 5 nm of ALD HfO_x and 6 nm of MLD Hf(EG) thin films were deposited, individually. 1 $mg \cdot cm^{-2}$ (± 0.2 $mg \cdot cm^{-2}$) of PiperION topcoat was incorporated using a dip-coating method to ensure a better contact between prepared anodes and bulk membranes. The prepared anode was assembled with a Pt-based cathode and 40-μm-thick-PiperION membrane in a 1 cm^2 AEMWE device and operated at 56 ± 1 °C with pure water feed. Figure 4.2b shows polarization curves of ALD and MLD coated anodes along with a control $Co(OH)_x$ anode without passivation coatings. While the Hf(EG) coated anode exhibited almost similar device performance of the control $Co(OH)_x$ anode, the HfO_x coated anode had a higher cell voltage, almost 400 mV higher than others at 1 $A \cdot cm^{-2}$. The high frequence resistance of the cell with HfO_x-coated anode was 0.24 Ω, significantly larger than those of Hf(EG)-coated and uncoated anodes (0.15 Ω). Even after *iR* correction, HfO_x coated anode had a overpotential ~300 mV higher than those of Hf(EG) coated and control anodes (Figure C.2b). This is expected considering the difference in the film density and compactness between HfO_x and Hf(EG) layers, as alkoxide linkers in Hf(EG) film would give open pores and allow OH^- diffusion more readily than HfO_x film.. From limited OH^- transportation within HfO_x, the $Co(OH)_x$ reconstruction to more active $CoO_x(OH)_y$ phase would slow down, leading to slow OER kinetics.

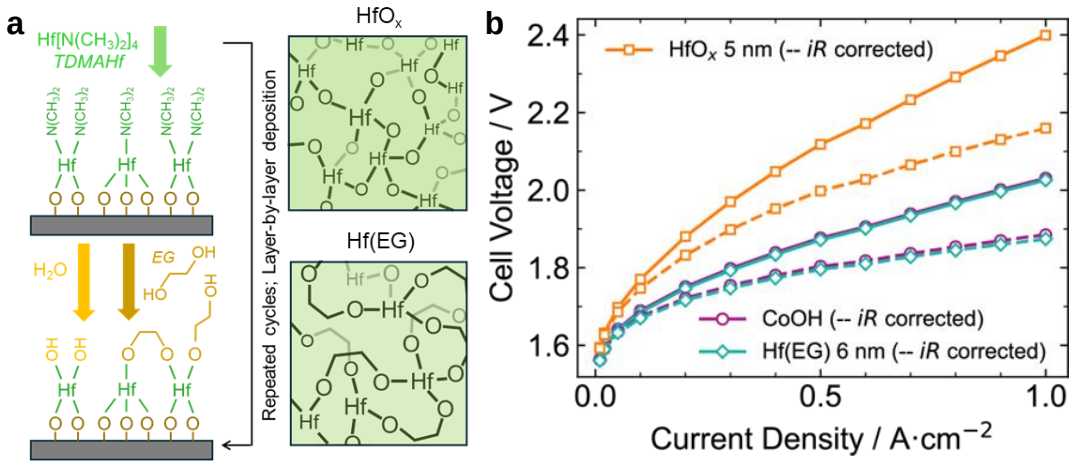

Figure 4.2 ALD and MLD comparison

(a) Scheme of ALD and MLD processes and **(b)** polarization curves of AEMWE cells with ALD HfO_x and 6 nm of MLD Hf(EG) coatings on $Co(OH)_x$ anodes. The cell was operated at 56 °C with pure water feed. Dashed lines are *iR*-corrected.

Effect of Hf(EG) thickness on AEMWE device

To investigate how Hf(EG) coatings with different thickness affect the AEMWE device performance and durability, a series of Hf(EG)-coated anodes were prepared with Hf(EG) thicknesses of 3, 6, 12, 23, and 47 nm. All the samples were tested in a pure water-fed AEMWE device under the same conditions (cathode, membrane, temperature, feed mode, etc.) except for the anode.[9] Polarization curves were initially obtained at the beginning of the test (BOT), along with an electrochemical impedance spectrum (EIS) and cyclic voltammograms (CV). The cell was then held at a constant current of 1 $A \cdot cm^{-2}$ for 40 h to evaluate the durability. After this period, another polarization curve, EIS and CV measurements were conducted as end-of-test (EOT) metrics. All unprocessed data can be found in Figure C.3. Figure 4.3a summarizes the cell voltages at 1 $A \cdot cm^{-2}$ at both BOT and EOT, and the minimum cell voltages observed during the durability tests for the various Hf(EG)-coated anodes. The minimum cell voltages were extracted to account for the initial stabilization/activation phase during the constant operation, which seemed varied

with Hf(EG) thickness. At the BOT, the anode with a 3 nm Hf(EG) demonstrated better performance than the control $Co(OH)_x$ anode. The performance improvement may be attributed to interaction between $Co(OH)_x$ catalysts and overlaid Hf(EG), which facilitates formation of water channel and enhances OH^- transport, similar to role of ZrO_x when incorporated in bulk AEM.[20] However, for thicker Hf(EG) coatings (23 and 47 nm), the cell voltage increased due to electrical and ionic resistances introduced by the Hf(EG) layers. At the EOT, while the uncoated $Co(OH)_x$ anode exhibited a degraded cell voltage of 2.27 V, most of the Hf(EG)-coated anodes maintained a cell voltage around 2.05 V.

The ohmic drops at both BOT and EOT were calculated from high-frequency resistances in the EIS at 50 m $A \cdot cm^{-2}$ (Figure C.4). Generally, as the Hf(EG) coating thickness increased, the ohmic drop also increased, contributing significantly to the increase in cell voltages at the BOT for the 23- and 47-nm-Hf(EG)-coated anodes (Figure 4.3b). At the EOT, however, ohmic drop values were similar for all anodes, except for the $Co(OH)_x$ anode, likely due to severe degradation of the catalyst-ionomer interface, which resulted in higher contact resistance. We speculate that the decrease in ohmic drops for Hf(EG) coated anodes after operation may be due to ionomer-Hf(EG)-$Co(OH)_x$ layer intermixing and forming a stable interphase, etching of Hf(EG) during operation, or the sacrificial oxidation of Hf(EG); however, these mechanisms have yet to be proven. Figure 4.3c presents the kinetic losses at the BOT and EOT, extracted from Tafel-like iR-corrected overpotential versus logarithmic current density plots. Linear extrapolations of the plots yielded kinetic overpotentials at 1 $A \cdot cm^{-2}$ (only data points up to a current density of 100 $mA \cdot cm^{-2}$ were used to exclude any effects from catalyst resistances or mass transport). Interestingly, the kinetic performance was not significantly affected by the Hf(EG) coatings, suggesting that while those layers added extra resistances to the cell, they did not change the intrinsic kinetic of $Co(OH)_x$

at the BOT. The kinetic drop data at the EOT implies that the huge cell voltage degradation is coming from the poor kinetics of $Co(OH)_x$ when it was not passivated with Hf(EG). The catalyst-ionomer interface is expected to experience severe damage.

The cell voltage degradation rates were calculated as changes in cell voltage over time, from the start of degradation (when the minimum cell voltage was observed) to the EOT for each anode. These rates are plotted against the start times of degradation in Figure 4.3d. It was found that a 6 nm of Hf(EG) coating was sufficient to extend the lifetime of anodes, while uncoated or 3-nm-thick-Hf(EG) coated anodes began to degrade earlier and exhibited higher cell voltage degradation rates. All other samples possessed the cell voltage degradation rates lower than 1 $mV \cdot h^{-1}$. The EIS plots in Figure 4.3e correspond to the cell metrics measured. The EIS of $Co(OH)_x$ control anode exhibited an increase in charge transfer resistance at the EOT compared to the BOT. In contrast, the EIS of the anode with 47 nm of Hf(EG) shifted left after the durability test, with no change in the charge transfer resistance, but a decrease in high frequency resistance. The EIS at 1.25 V in Figure C.5 also provided evidence of degradation of the catalyst-ionomer interface of the unpassivated $Co(OH)_x$ anode from a largely limited ionic diffusion (the decreased slope for the stretch at low frequencies) after 40 h of operation. In contrast, relatively thicker Hf(EG)-coated anodes showed improved ionic diffusion, presumably either forming an efficient ionic transport path upon the cell operation or Hf(EG) coatings being etched out over time. Figure C.6 summarizes the substantial retention of active surface area with Hf(EG) coatings. Although 40 hours of operation may not be sufficient to fully demonstrate the passivated anodes in pure water AEMWE systems, this was intended to screen and evaluate the effective thickness of Hf(EG) coatings.

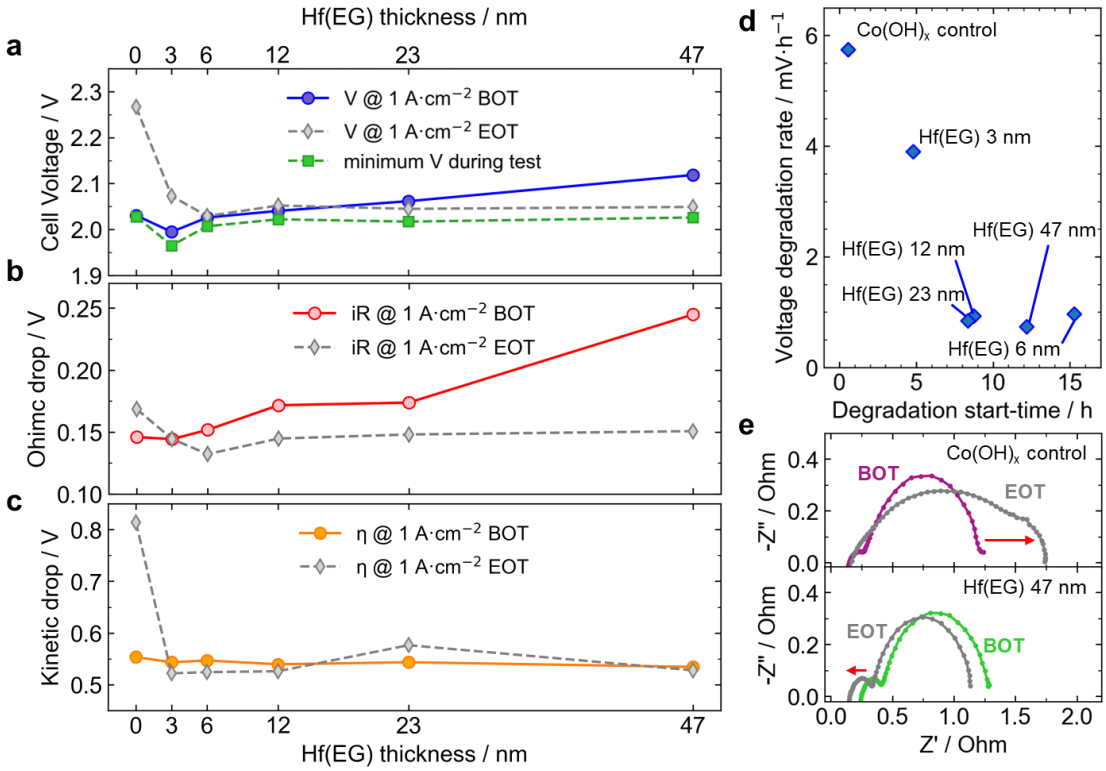

Figure 4.3 MLD coating thickness dependent AEMWE device performance and durability

(a) The cell voltages at 1 A cm^{-2} at the BOT and EOT along with the minimum cell voltage during the durability test are plotted as a function of Hf(EG) thickness. (b)Plot of ohmic drops at 1 A cm^{-2} at the BOT and EOT as a function of Hf(EG) thickness. The ohmic resistances were determined from galvano electrochemical impedance spectra obtained at 50 mA cm^{-2}. (c) Plot of kinetic drops at 1 A cm^{-2} at the BOT and EOT as a function of Hf(EG) thickness. The kinetic drops were calculated from the Tafel equation fitted at low current densities. (d) 2D plot of the cell voltage degradation versus the degradation start-time of above-mentioned anodes. The degradation start-time was sampled when the cell voltage started to increase during the durability test. The cell voltage degradation rate was calculated from the voltage difference over the degradation start-time to the end-of-test time. (e) Galvano electrochemical impedance spectra of $Co(OH)_x$ control anode and 47-nm-thick-Hf(EG)-coated anode at the BOT and EOT.

Ex-situ characterization of passivated anodes

Electrochemical analysis in the AEMWE device demonstrated that Hf(EG) coatings were stabilizing the anode catalyst-ionomer interfaces, thereby extending the durability of the cell without a huge penalty in the cell performance. To understand degradation modes of anodes, we first conducted SEM and XPS analyses to monitor the time-dependent catalyst-ionomer stabilization/degradation without Hf(EG) coatings along with electrochemical analysis. Here we

operated the cell at 70 °C with the same procedure as previous but the maximum operation current density was 2 $A \cdot cm^{-2}$. This was intended to accelerate the degradation modes of anodes during the durability runs, and we varied the duration of durability tests as 1, 3, 5, and 10 hours. After each operation, the anode was washed with deionized water and soaked in 3 M NaCl to exchange OH^- in ionomer topcoat to Cl^- to minimize ionomer degradation from OH^- nucleophilic attack. SEM images in Figure C.7 show that without any Hf(EG) passivation layer, the anode catalyst-ionomer was hugely damaged within 5 h, with catalysts exposed as ionomers degraded and being washed out. After 10 hours of operation, most ionomers were gone and the nanostructured $Co(OH)_x$ layer collapsed. However, with the same operation time, the Hf(EG)-coated anode retained its original structure (Figure 4.4). In XP spectra (Figure C.9), despite the existence of N 1s and F 1s peaks from PiperION structure, in all the operated anodes without Hf(EG) coatings, Co 2p peaks associated with anode catalyst layer became prominent as the operation time proceeded. On the other hand, for the 47 nm-thick-Hf(EG)-coated anode, the XPS peaks of charged nitrogen and fluorinated carbon species were retained after 10 h of operation, but Co 2p signals were still weak. This aligns with the above-mentioned SEM and EDX map results. It is expected that based on our previous study, interfacial layers between the anode catalyst and ionomer/membrane can prevent electron spillover from ionomers to catalysts and thereby electrochemical oxidation of ionomers.[11] Additionally, all the electrolyzer data is summarized in Table C.1 as percentage changes of cell voltages, integrated charges, high frequency resistances, and cell voltage degradation rates.

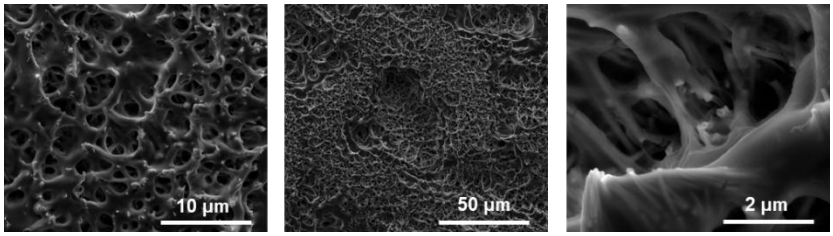

Figure 4.4 Suppressed catalyst and ionomer degradation with Hf(EG) coating

SEM images of Hf(EG) coated anode after the 10 h of cell operation at 2 $A \cdot cm^{-2}$ (70 °C). Still $Co(OH)_x$ catalyt and ionomer experience degradation with an oxidative bias but less severe than those without Hf(EG) coatings. Less reconstructed catalyst featured in the magnified SEM image.

This ongoing work has focused on ex-situ characterization on anodes to investigate how Hf(EG) coatings improved the stability of catalysts and ionomers. We plan to further probe real-time catalyst dissolution or particle detachment using in-situ / online inductively coupled plasma mass spectrometry (ICP-MS). Additionally, we will study the mechanical and (electro)chemical stability of Hf(EG) MLD coatings in the future.

CONCLUSION

In summary, we developed anode catalyst-ionomer interfaces modified using a molecular layer deposition method for stable pure water-fed AEMWE operation. MLD Hf(EG) layers were successfully incorporated in porous electrodes, and various film parameters, such as Hf(EG) thickness, processing temperature, and porosity were controlled to understand how those parameters affect anode performance and durability. It was found that < 20 nm of Hf(EG) coatings enhanced the durability in AEMWE cell voltage, while not compromising the anode catalytic activity, while even 5 nm of ALD HfO_x led to poor anode kinetics. Online ICP-MS data Hf(EG) layers suppressed dissolution of underlying Co-based catalysts, and SEM and XPS analysis indicated less electrochemical oxidation of overlayed ionomers with Hf(EG) passivation coatings.

This work provides a key engineering factor in the AEMWE device other than HER/OER catalysts, ionomers and membranes, showing that how catalyst layers and ionomers are

constructed into the porous electrodes hugely impacts the overall cell performance and durability. On top of our study, ALD/MLD co-deposition and use of different organic linkers can be applied in AEMWE electrode design to fine tune electronic and ionic processes in porous electrodes and to improve the mechanical and chemical stability.

EXPERIMENTAL METHODS

Electrode preparation

For anodes, a $Co(OH)_x$ layer was grown on a Ni alloy porous transport layer (PTL) using an optimized recipe of hydrothermal synthesis in Chapter II. Atomic / molecular layer deposition was conducted at 120 °C, alternating a pulse of tetrakis(dimethylamido)hafnium(IV), TDMAHf, and water or ethylene glycol (EG). In between pulses, N_2 gas was purged. The thickness of ALD and MLD layers was calculated using an ellipsometer on a Si wafer. Before assembling anodes in the cell, 1 $mg \cdot cm^{-2}$ of PiperION (Versogen) ionomer topcoat was added. For cathodes, Pt black (Fuel Cell Store) nanoparticle powder was mixed with PiperION ionomer in water/isopropyl alcohol solution and spraycoated on a Toray 090 carbon paper (Fuel Cell Store). After achieving a catalyst layer loading of 2 $mg \cdot cm^{-2}$, a thin ionomer topcoat (0.1-0.2 $mg \cdot cm^{-2}$) was added.

Membrane electrode assembly (MEA) and AEMWE single cell operation

The AEMWE single cell assembly and operation were prepared same as Chapter II and III, a 40-μm-thick-AEM (PiperION, Versogen) was sandwiched between 1 cm^2-sized cathode and anode with gaskets. The MEA was compressed between flow fields and bipolar plates. By flowing pre-heated high-purity water (18.2 MΩ·cm, 62 °C) to both anode and cathode, the cell temperature was kept as 56 °C. Electrochemical data of AEMWE single cell was obtained using a potentiostat, BioLogic VSP-300, equipped with a 10 A/5 V booster. As an initial cell break-in procedure, the current was stepped up from 100 $mA \cdot cm^{-2}$ to 1 $A \cdot cm^{-2}$ with an interval of 100 $mA \cdot cm^{-2}$, then the

current was stepped down back to 10 $mA \cdot cm^{-2}$ to obtain a polarization curve. For some experiments, the maximum current was raised to 2 $A \cdot cm^{-2}$. Potentio electrochemical impedance spectra was obtained at 1.25 V (voltage where no significant faradaic reaction happens), and galvano electrochemical impedance was measured at 50 $mA \cdot cm^{-2}$, where mass transportation effect was minimized with a frequency range of 1 MHz to 100 mHz. To monitor electrochemically active surface area, cyclic voltammetry was performed by sweeping a cell voltage between 0.6 V and 1.6 V at a scan rate of 100 $mV \cdot s^{-1}$. For a durability test, the cell was held at either 1 $A \cdot cm^{-2}$ or 2 $A \cdot cm^{-2}$ for a certain period. After the durability test, polarization curve, impedance spectra, and cyclic voltammogram were obtained as end-of-test metrics.

Materials Characterization

A Helios Hydra (Thermo Fisher) was used to obtain scanning electron microscopy (SEM) images at 5 kV. Cross-sectioned anode interfaces were probed using a plasma focused-ion-bean (PFIB) and EDS analyzer. X-ray photoelectron spectroscopy (XPS) measurements were conducted using a Kratos Axis Ultra DLD system equipped with a monochromatic Al Kα. All spectra were calibrated with the binding energy of C 1s main carbon peaks adjusted to 284.8 eV using CasaXPS software.

BRIDGE

Chapter IV builds upon the passivated anode architecture introduced in Chapter III, further advancing the design with Hf(EG) MLD coatings. These MLD coatings exhibit superior ion permeability and flexibility, facilitating OH^- transport toward underlying catalyst layers at the anodes. From there, the AEMWE cell performance can be retained while extending the lifetime of anodes by suppressing ionomer and catalyst degradation. This work provides valuable insights into

constructing durable AEMWE devices that operate with pure water feed, bringing the technology closer to commercialization.

REFERENCES

(1) Wang, A.; Kadam, S.; Li, H.; Shi, S.; Qi, Y. Review on modeling of the anode solid electrolyte interphase (SEI) for lithium-ion batteries. *npj Computational Materials* **2018**, *4* (1), 15.

(2) Deng, T.; Ji, X.; Zhao, Y.; Cao, L.; Li, S.; Hwang, S.; Luo, C.; Wang, P.; Jia, H.; Fan, X.; et al. Tuning the Anode–Electrolyte Interface Chemistry for Garnet-Based Solid-State Li Metal Batteries. *Adv. Mater.* **2020**, *32* (23), 2000030.

(3) Satu Kristiina, H.; Jongjung, K.; Brett, L. L. Generation and Evolution of the Solid Electrolyte Interphase of Lithium-Ion Batteries. *Joule* **2019**, *3* (10), 2322-2333.

(4) Liu, J.; Kang, Z.; Li, D.; Pak, M.; Alia, S. M.; Fujimoto, C.; Bender, G.; Kim, Y. S.; Weber, A. Z. Elucidating the Role of Hydroxide Electrolyte on Anion-Exchange-Membrane Water Electrolyzer Performance. *J. Electrochem. Soc.* **2021**, *168* (5), 054522.

(5) Li, D.; Motz, A. R.; Bae, C.; Fujimoto, C.; Yang, G.; Zhang, F. Y.; Ayers, K. E.; Kim, Y. S. Durability of Anion Exchange Membrane Water Electrolyzers. *Energy and Environmental Science* **2021**, *14* (6), 3393-3419.

(6) Milosevic, M.; Böhm, T.; Körner, A.; Bierling, M.; Winkelmann, L.; Ehelebe, K.; Hutzler, A.; Suermann, M.; Thiele, S.; Cherevko, S. In Search of Lost Iridium: Quantification of Anode Catalyst Layer Dissolution in Proton Exchange Membrane Water Electrolyzers. *ACS Energy Lett.* **2023**, *8* (6), 2682-2688.

(7) Priamushko, T.; Franz, E.; Logar, A.; Bijelić, L.; Guggenberger, P.; Escalera-López, D.; Zlatar, M.; Libuda, J.; Kleitz, F.; Hodnik, N.; et al. Be Aware of Transient Dissolution Processes in Co3O4 Acidic Oxygen Evolution Reaction Electrocatalysts. *J. Am. Chem. Soc.* **2025**, *147* (4), 3517-3528.

(8) Lindquist, G. A.; Gaitor, J. C.; Thompson, W. L.; Brogden, V.; Noonan, K. J. T.; Boettcher, S. W. Oxidative Instability of Ionomers in Hydroxide-Exchange-Membrane Water Electrolyzers. *Energy Environ. Sci.* **2023**, 4373-4387.

(9) Krivina, R. A.; Lindquist, G. A.; Beaudoin, S. R.; Stovall, T. N.; Thompson, W. L.; Twight, L. P.; Marsh, D.; Grzyb, J.; Fabrizio, K.; Hutchison, J. E.; et al. Anode Catalysts in Anion-Exchange-Membrane Electrolysis without Supporting Electrolyte: Conductivity, Dynamics, and Ionomer Degradation. *Adv. Mater.* **2022**, *34* (35).

(10) Zhang, L.; Xu, Q.; Hu, Y.; Chen, L.; Jiang, H. Benchmarking the pH–Stability Relationship of Metal Oxide Anodes in Anion Exchange Membrane Water Electrolysis. *ACS Sustainable Chemistry & Engineering* **2023**, *11* (36), 13251-13259.

(11) Kwak, M.; Ojha, K.; Shen, M.; Boettcher, S. W. Electrically Insulated Catalyst–Ionomer Anode Interfaces toward Durable Alkaline Membrane Electrolyzers. *ACS Energy Lett.* **2024**, *9* (3), 1025-1034.

(12) Zhou, L.; Guo, D.; Wu, L.; Guan, Z.; Zou, C.; Jin, H.; Fang, G.; Chen, X. a.; Wang, S. A Restricted Dynamic Surface Self-Reconstruction toward High-Performance of Direct Seawater Oxidation. *Nat. Commun.* **2024**, *15* (1), 2481.

(13) Li, M.; Saedy, S.; Fu, S.; Stellema, T.; Kortlever, R.; van Ommen, J. R. Enhancing the Durability of Pt Nanoparticles for Water Electrolysis using Ultrathin SiO_2 Layers. *Catalysis Science & Technology* **2024**, *14* (5), 1328-1335.

(14) Tran-Phu, T.; Chen, H.; Daiyan, R.; Chatti, M.; Liu, B.; Amal, R.; Liu, Y.; Macfarlane, D. R.; Simonov, A. N.; Tricoli, A. Nanoscale TiO_2 Coatings Improve the Stability of an Earth-Abundant Cobalt Oxide Catalyst during Acidic Water Oxidation. *ACS Applied Materials and Interfaces* **2022**.

(15) Lee, B. H.; Anderson, V. R.; George, S. M. Growth and Properties of Hafnicone and HfO_2/Hafnicone Nanolaminate and Alloy Films Using Molecular Layer Deposition Techniques. *ACS Appl. Mater. Interfaces* **2014**, *6* (19), 16880-16887.

(16) Vemuri, V.; King, S. W.; Thorpe, R.; Jones, A. H.; Gaskins, J. T.; Hopkins, P. E.; Strandwitz, N. C. Chemical, Structural, and Electrical Changes in Molecular Layer-Deposited Hafnicone Thin Films after Thermal Processing. *ACS Applied Electronic Materials* **2024**, *6* (7), 5173-5182.

(17) Ban, C.; George, S. M. Molecular Layer Deposition for Surface Modification of Lithium-Ion Battery Electrodes. *Adv. Mater. Interfaces* **2016**, *3* (21), 1600762.

(18) Sundberg, P.; Karppinen, M. Organic and Inorganic-Organic Thin Film Structures by Molecular Layer Deposition: A Review. *Beilstein journal of nanotechnology* **2014**, *5*, 1104-1136.

(19) Zhao, Y.; Zhang, L.; Liu, J.; Adair, K.; Zhao, F.; Sun, Y.; Wu, T.; Bi, X.; Amine, K.; Lu, J.; et al. Atomic/Molecular Layer Deposition for Energy Storage and Conversion. *Chem. Soc. Rev.* **2021**, *50* (6), 3889-3956.

(20) Ji Eun, K.; Young Hwa, Y.; Hyeonjung, P.; Justin, A.; Gisu, D.; Sechan, L.; Jongsu, S.; Changsoo, L.; MinJoong, K.; Hyun-Seok, C.; et al. Hydrogen-bonded QSEBS/ZrO_2 mixed matrix anion exchange membranes for water electrolyzer. *Fuel* **2024**, *376*, 132684.

(21) Kasian, O.; Geiger, S.; Mayrhofer, K. J. J.; Cherevko, S. Electrochemical On-line ICP-MS in Electrocatalysis Research. *The Chemical Record* **2019**, *19* (10), 2130-2142.

CHAPTER V

CONCLUSIONS AND OUTLOOK

Unpublished material written by myself.

This dissertation presented key advancements in anode design for pure-water-fed anion exchange-membrane-water electrolyzers (AEMWEs). Chapter I outlined challenges and strategies in material selection, porous electrode construction, and interfacial engineering for cost effective, efficient, and durable anodes in the AEMWE systems. In Chapter II, we developed self-supported Co-based anodes to understand catalyst-ionomer interactions and interfacial activation/degradation mechanisms. The optimized Co_3O_4 self-supported anode outperformed the conventional nanoparticle-based anode as a result of micron-scale continuous electrical and ionic conduction. The as-synthesized $Co(OH)_x$ further improved the device performance, presumably from structural hydroxyl groups in the bulk $Co(OH)_x$ catalyst layer, which facilitated rapid reconstruction into the more active $CoO_x(OH)_y$ phase. Still, the "limited" catalyst-ionomer interface in pure water-fed AEMWE poses challenges in ensuring long-term stability. Remember that the reactant for the oxygen evolution reaction (OER), OH^-, is only supplied to the catalyst surface from overlaid ionomers contacting with bulk AEM in pure water systems. Nonetheless, this work emphasizes the importance of porous electrode microstructures, which can also be leveraged to design high performing anodes as well as improve cathodes−an area beyond the scope of this study but equally important. Furthermore, this model anode design provides more well-

defined catalyst-ionomer interfaces, unlike NP-based anodes, where interfaces are randomly distributed throughout the catalyst layer. These well-defined interfaces enable the strategic incorporation of passivation coatings, a key approach to addressing durability challenges in AEMWE anodes.

Chapter III served as a proof-of-concept demonstration of "passivated anodes". We hypothesized that the durability problems arise from the oxidative instability of ionomers incorporated in anodes. Direct contact between the electrically conductive anode catalysts and ionomers makes ionomers susceptible to electrochemical oxidation, which in turn limits the supply of OH^- to the catalyst surface, increasing the overpotentials for the oxygen evolution reaction. By introducing a thin HfO_x layer (2-3 nm) via atomic layer deposition (ALD) between the anodic catalyst and ionomer layers, we observed less ionomer oxidation and improved device stability. This enables future studies on designing durable anode architecture using interface/interphase engineering, emphasizing the need for tailored passivation layers that balances catalytic activity and durability.

In Chapter IV, we further investigated the design principles and chemistry of passivation coatings. Building on Chapter III, we developed ion-permeable, flexible Hf-ethylene glycol (EG) crosslinked passivation coatings using molecular layer deposition (MLD). These coatings effectively blocked the electron spillover from catalyst to ionomer, reducing ionomer oxidation while offering superior OH^--ion-permeability compared to compact ALD HfO_x. This improved permeability enabled thicker coatings−up to 50 nm−without significantly compromising device performance. Additionally, MLD coatings suppressed catalyst degradation (*i.e.*, catalyst dissolution and fragmentation/detachment). Although we successfully demonstrated Hf(EG) as a passivation material, reducing degradation of both catalysts and ionomers, the exact mechanisms

underlying MLD coating functionality remain unproven. We hypothesize three possible explanations: (*i*) interlayer mixing of Hf(EG) and underlying $Co(OH)_x$, forming a more stable interphase, (*ii*) Hf(EG) etching via hydrolysis or OH^- attack, or (*iii*) sacrificial oxidation of Hf(EG), all could contribute to a nominally stable cell voltage. In-depth characterization could help elucidate these mechanisms, such as real-time detection of any dissolved Hf-containing species or ionomer species in the anode effluent using liquid/gas chromatography-mass spectroscopy and/or ICP-MS, as well as *ex-situ* studies on Hf(EG) stability. Additionally, exploring various ALD/MLD coating chemistries and layer designs would be valuable directions for future research. For instance, how would incorporating two metal species in ALD coatings−such as alternating deposition of HfO_x and ZrO_x, or HfO_x and AlO_x−affect device metrics? What if ALD and MLD layers were alternated to control the compactness and electronic properties of final films?[1] What other organic linkers could be used to fine-tune the ion permeability and film stability?[2] Furthermore, how do these factors influence key film properties (i.e., dielectric constant, mechanical strength, (electro)chemical stability, and porosity) and, in turn, impact the AEMWE anode performance and durability? There are numerous engineering parameters to explore.

This dissertation focused on understanding and engineering anode catalyst-ionomer interfaces for efficient and durable "electrolyte-free" AEMWE. Beyond the research and development discussed above, what other key components should be further investigated to ultimately demonstrate the commercial viability of this technology?

First, there is still a significant performance gap between AEMWE and other water electrolysis technologies.[3,4] To overcome this, highly conductive and active non-precious group metal (non-PGM) anode catalysts should be designed. Zhai *et al*. demonstrated perovskite-based anode catalysts, with metallic electrical conductivities and high surface areas, achieving

exceptional performance in pure-water-fed systems.[5] Further research should focus on optimizing composition, morphology/structure, as well as refining electrode geometry to maximize catalyst-ionomer interfacial areas and enhance overall efficiency.

Second, we need to develop non-PGM cathode catalysts with activity and stability comparable to Pt-based catalysts. To compensate for the higher activity of Pt, increasing the loading of non-PGM catalysts or incorporating conductive support to overcome their lower intrinsic activity and electrical conductivity is necessary. However, enabling those catalysts to operate at high current densities is challenging,[6] especially in pure water systems, where the available active area is limited by OH^- transportation. Future research should focus on optimizing catalyst composition, morphology, and integration strategies as porous electrodes.

Third, the development of alkaline-stable ionomers and membranes is crucial for advancing AEMWE technology. While proton exchange membrane water electrolyzers (PEMWEs) have demonstrated over 10,000 hours of stable operation with Nafion^{TM}, achieving similar durability for pure-water-fed AEMWEs remains a challenge.[7] Developing an AEMWE-compatible Nafion counterpart, with high ionic conductivity, chemical/mechanical stability under operating conditions, would be a major technological breakthrough.

Finally, with all components developed individually, we can revisit previously introduced interfacial engineering concepts to form stable catalyst-ionomer/membrane interfaces, incorporating all components as an ultimate device.

Interfacial engineering strategies, inspired by advanced battery technologies,[8-10] will not only contribute to the ongoing progress in AEMWE technology but also provide valuable principles applicable to relevant water electrolysis technologies. For example, in PEMWE systems, researchers have been working to thrift use of iridium,[11,12] a critical material in commercialized

devices. At such low Ir loadings, device durability is heavily dependent on the dissolution rate of Ir-based OER catalysts under oxidative bias.[13,14] This inevitable Ir dissolution can be mitigated by incorporating functional passivation coatings over Ir-based catalyst layers. To successfully integrate this approach into PEMWE systems, the chemistry and properties of these protective films must be carefully tailored to ensure compatibility and effectiveness. In alkaline water electrolysis (AWE) systems, iron plays a crucial role in improving the OER activity of base catalysts, either as dissolved species in the electrolytes or as part of OER catalyst itself. However, dissolved iron species can redeposit onto HER catalysts and deactivate them, while Fe dissolution from OER catalysts can degrade their catalytic performance.[15-17] Passivation coatings can provide a potential solution here, by preventing Fe leaching, minimizing migration through the system, and deteriorating the cathode performance. Obata *et al*. demonstrated a CeO_x-coated NiFe-based OER catalyst, where the CeO_x layer served as a permselective barrier, allowing reactants and products to diffuse in and out while limiting Fe dissolution to the bulk electrolyte.[18] Translating this approach into practical devices would be valuable.

REFRENCES

(1) Karttunen, A. J.; Tynell, T.; Karppinen, M. Atomic-Level Structural and Electronic Properties of Hybrid Inorganic–Organic ZnO:Hydroquinone Superlattices Fabricated by ALD/MLD. *J. Phys. Chem. C* **2015**, *119* (23), 13105-13114.

(2) Multia, J.; Karppinen, M. Atomic/Molecular Layer Deposition for Designer's Functional Metal–Organic Materials. *Adv. Mater. Interfaces* **2022**, *9* (15), 2200210.

(3) Vincent, I.; Lee, E.-C.; Kim, H.-M. Comprehensive Impedance Investigation of Low-Cost Anion Exchange Membrane Electrolysis for Large-Scale Hydrogen Production. *Sci. Rep.* **2021**, *11* (1), 293.

(4) Kang, S. Y.; Park, J. E.; Jang, G. Y.; Kim, O.-H.; Kwon, O. J.; Cho, Y.-H.; Sung, Y.-E. High-Performance and Durable Water Electrolysis Using a Highly Conductive and Stable Anion-Exchange Membrane. *Int. J. Hydrogen Energy* **2022**, *47* (15), 9115-9126.

(5) Zhai, T.; Wang, H.; Beaudoin, S.; Zhang, R.; Kwak, M.; Hou, S.; Guo, Z.; Boettcher, S. W. Perovskite Catalysts for Pure-Water-Fed Anion-Exchange-Membrane Electrolyzer Anodes: Co-Design of Electrically Conductive Nanoparticle Cores and Active Surfaces. *ChemRxiv* **2025**.

(6) Serban, A.; Liu, M.-T.; Chen, N.; Chen, H. M.; Hu, X. An Oxide-Promoted, Self-Supported Ni_4Mo Catalyst for High Current Density Anion Exchange Membrane Water Electrolysis. *Energy Environ. Sci.* **2025**, *18* (3), 1533-1543.

(7) Li, D.; Motz, A. R.; Bae, C.; Fujimoto, C.; Yang, G.; Zhang, F. Y.; Ayers, K. E.; Kim, Y. S. Durability of Anion Exchange Membrane Water Electrolyzers. *Energy and Environmental Science* **2021**, *14* (6), 3393-3419.

(8) Yang, Z.; Kelly, Z.; Xueliang, S. Addressing Interfacial Issues in Liquid-Based and Solid-State Batteries by Atomic and Molecular Layer Deposition. *Joule* **2018**, *2* (12), 2583-2604.

(9) Kim, K.; Ma, H.; Park, S.; Choi, N.-S. Electrolyte-Additive-Driven Interfacial Engineering for High-Capacity Electrodes in Lithium-Ion Batteries: Promise and Challenges. *ACS Energy Lett.* **2020**, *5* (5), 1537-1553.

(10) Shi, P.; Wang, X.; Cheng, X.; Jiang, Y. Progress on Designing Artificial Solid Electrolyte Interphases for Dendrite-Free Sodium Metal Anodes. *Batteries* **2023**, *9* (7), 345.

(11) Ferner, K. J.; Litster, S. Composite Anode for PEM Water Electrolyzers: Lowering Iridium Loadings and Reducing Material Costs with a Conductive Additive. *ACS Appl. Energy Mater.* **2024**, *7* (18), 8124-8135.

(12) Mark, C.; Christopher, M. Z.; Margery, R. Perspectives on Current and Future Iridium Demand and Iridium Oxide Catalysts for PEM Water Electrolysis. *Catal. Today* **2023**, *420*, 114140.

(13) Milosevic, M.; Böhm, T.; Körner, A.; Bierling, M.; Winkelmann, L.; Ehelebe, K.; Hutzler, A.; Suermann, M.; Thiele, S.; Cherevko, S. In Search of Lost Iridium: Quantification of Anode Catalyst Layer Dissolution in Proton Exchange Membrane Water Electrolyzers. *ACS Energy Lett.* **2023**, *8* (6), 2682-2688.

(14) Lončar, A.; Escalera-López, D.; Cherevko, S.; Hodnik, N. Inter-Relationships between Oxygen Evolution and Iridium Dissolution Mechanisms. *Angew. Chem. Int. Ed.* **2022**, *61*.

(15) Demnitz, M.; Lamas, Y. M.; Garcia Barros, R. L.; de Leeuw den Bouter, A.; van der Schaaf, J.; Theodorus de Groot, M. Effect of Iron Addition to the Electrolyte on Alkaline Water Electrolysis Performance. *iScience* **2024**, *27*

(16) Matheus, T. Alkaline Water Electrolysis: With or Without Iron in the Electrolyte? *Current Opinion in Chemical Engineering* **2023**, *42*, 100981.

(17) Rajeev, M.; Jerome-Saboori, A.; Shekhar, R.; Boettcher, S. W.; Kempler, P. A. Impacts of Dissolved Iron on Alkaline Water Electrolysis Cells. *ACS Catal.* **2025**, *15* (4), 2847-2856.

(18) Obata, K.; Takanabe, K. A Permselective CeO_x Coating To Improve the Stability of Oxygen Evolution Electrocatalysts. *Angew. Chem.* **2018**, *130* (6), 1632-1636.

APPENDIX A

CHAPTER II SUPPLEMENTARY INFORMATION

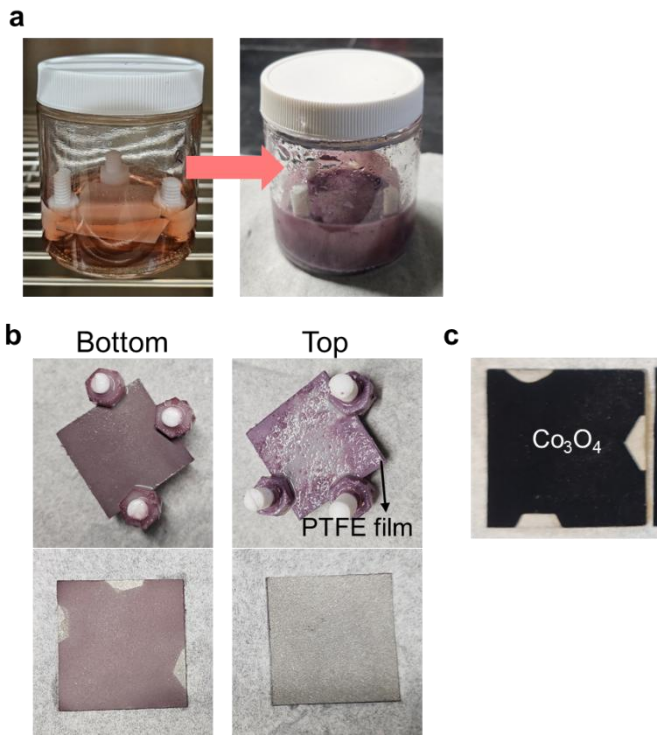

Figure A.1 Exemplified hydrothermal synthesis of Co-based catalysts

(a) Pictures of an assembled glass jar with a precursor solution and a PTFE masked Ni alloy PTL and the glass jar after the hydrothermal synthesis. **(b)** Pictures of a $Co(OH)_x$ catalyst layer selectively deposited on bottom side of the Ni alloy PTL. The top side was successfully masked with the PTFE film. **(c)** Picture of a Co_3O_4 catalyst layer on the PTL after annealing at 300 °C for 2 h.

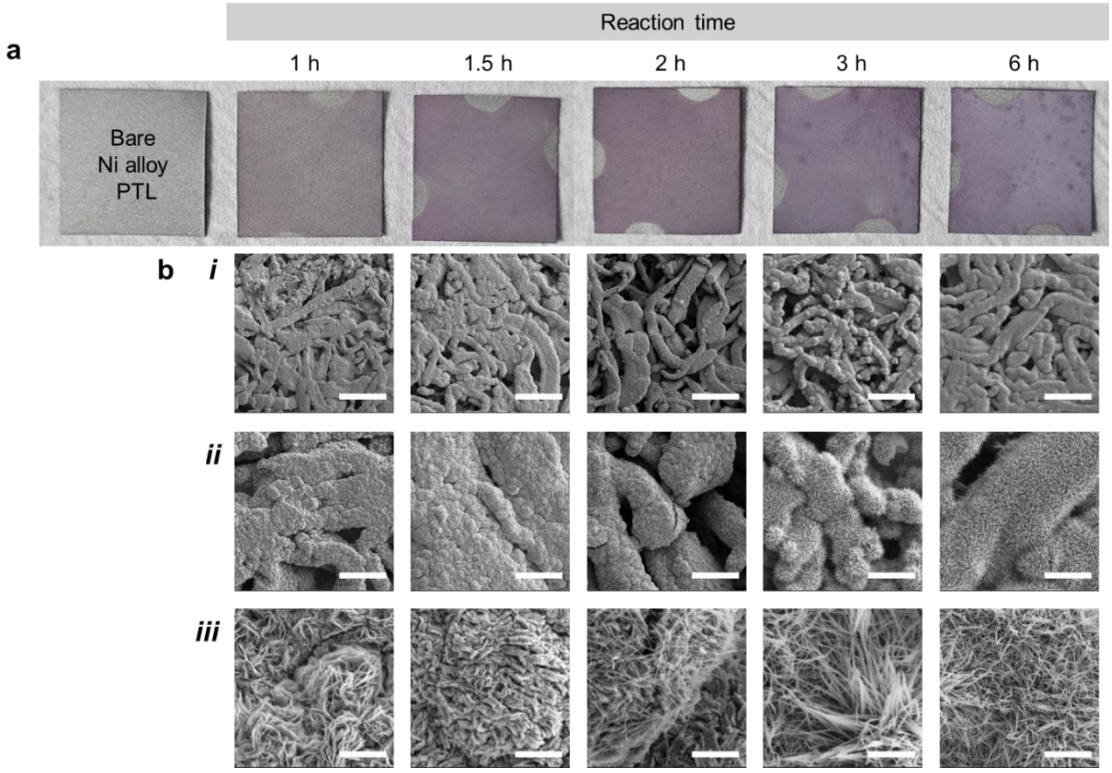

Figure A.2 Exemplified time-dependent study of hydrothermal synthesis of Co-based catalysts

(a) Images of bare and $Co(OH)_x$ deposited substrates. **(b)** SEM images of catalysts on the substrates vertically aligned based on reaction times at different magnification. Scale bars are set as (i) 100 μm, (ii) 25 μm, and (iii) 2 μm for each panel. All SEM images were obtained after annealing to prevent the charging effect because of the lower conductivity of as-synthesized $Co(OH)_x$.

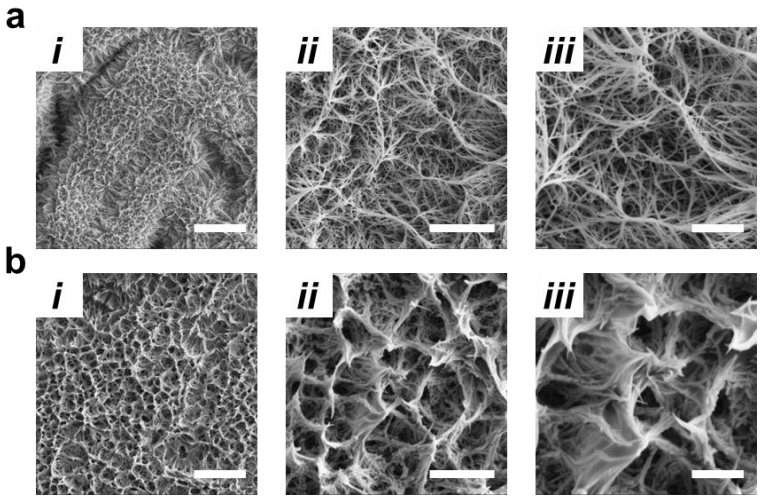

Figure A.3 SEM images of Co_3O_4 anodes

SEM images of **(a)** Co_3O_4 on Ni alloy PTL and **(b)** ionomer-coated Co_3O_4 on Ni alloy PTL (ionomer loading of 1 mg·cm^{-2}). Scale bars are set as (i) 20 μm, (ii) 5 μm, and (iii) 2 μm for each panel. After ionomer dip-coating, the sample had a more defined macrostructure.

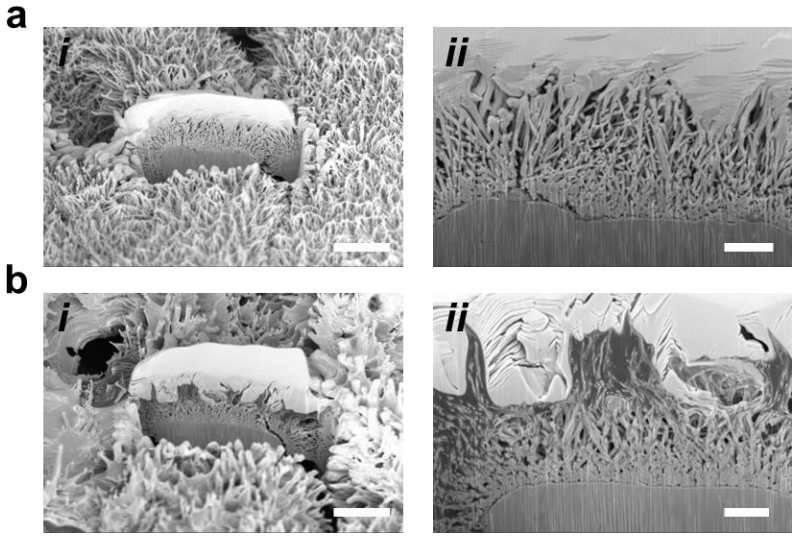

Figure A.4 Cross-sectional SEM images of ionomer-Co_3O_4 catalyst-PTLs

Cross-sectional SEM images of **(a)** Co_3O_4 on Ni alloy PTL and **(b)** ionomer-coated Co_3O_4 on Ni alloy PTL (ionomer loading of 1 mg·cm^{-2}). Scale bars are set as (i) 10 μm and (ii) 2 μm for each panel.

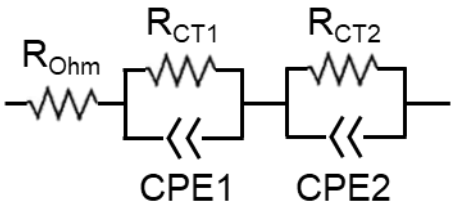

Figure A.5 Diagram of equivalent circuit representing AEMWE devices

Diagram of an equivalent electrical circuit of EIS Nyquist plot measured at 50 $mA \cdot cm^{-2}$. R_{Ohm} is a combination of electrical and ionic contact resistances, mostly governed by the ionic resistance through the membrane, but also influenced by the electrical resistances of assembled electrodes. Two semicircles in the Nyquist plot can be modelled with charge two sets of transfer resistance-constant phase element (CPE) in parallel, coming from anode and cathode reactions.

Table A.1 EIS fit results of different anode geometries

Sample	R_{Ohm} ($\Omega \cdot cm^2$)	R_{CT1} ($\Omega \cdot cm^2$)	Q_{CPE1} ($F \cdot s^{\alpha-1}$)	α_1	R_{CT2} ($\Omega \cdot cm^2$)	Q_{CPE2} ($F \cdot s^{\alpha-1}$)	α_2	Total R_{CT} ($\Omega \cdot cm^2$)
Self-supported Co_3O_4	0.119	0.937	0.133	0.79	0.147	0.008	0.68	1.084
NP Co_3O_4	0.156	1.088	0.082	0.68	0.196	0.082	0.68	1.284
Bare Ni alloy PTL	0.130	1.124	0.051	0.46	0.143	0.001	0.81	1.267

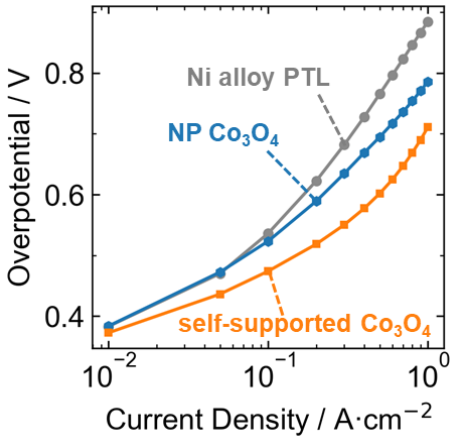

Figure A.6 Kinetics of different anode geometries

Plot of *iR-corrected* overpotential vs. current density in logarithm scale of pure water-fed AEMWE cells at 56 °C with a self-supported Co_3O_4 on PTL, ink-based Co_3O_4 on PTL, and bare Ni alloy PTL.

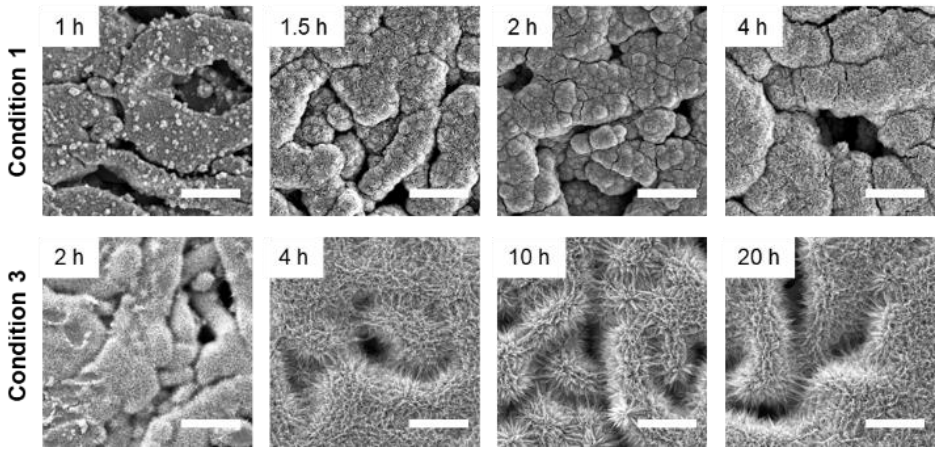

Figure A.7 Growth of $Co(OH)_x$ at different reaction times

SEM images of catalysts on the substrates with synthetic parameters (Condition 1 and 3 with different hydrothermal reaction times). Condition 1; 27 mmol of cobalt nitrate hexahydrate and 15 mmol urea used. Condition 3; 35 mmol of cobalt nitrate hexahydrate and 7.5 mmol urea used. SEM images of Condition 2 (35 mmol of cobalt nitrate hexahydrate and 15 mmol urea) are shown in Figure A.2. Scale bars are set as 25 μm, and all SEM images were obtained after annealing to prevent the charging effect.

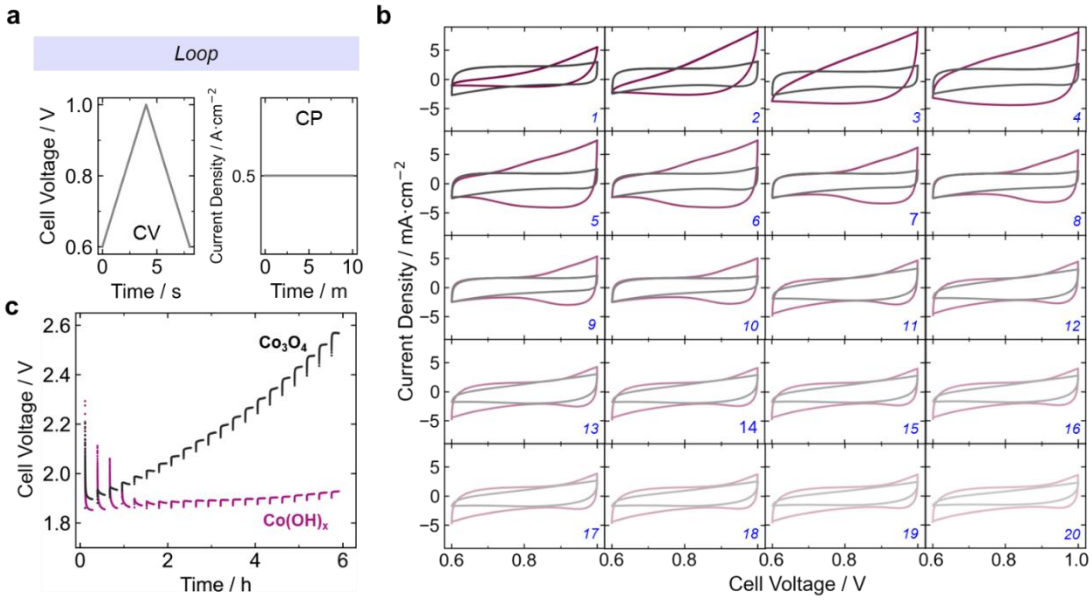

Figure A.8 Activation and degradation of $Co(OH)_x$ and Co_3O_4 in AEMWE devices

(a) Electrochemical technique built to monitor the catalyst activation and degradation of $Co(OH)_x$ and Co_3O_4 samples. The voltage was swept between 0.6 to 1.0 V at a scan rate of 100 $mV \cdot s^{-1}$ for 50 times (CV). The cell was held at 0.5 $A \cdot cm^{-2}$ for 10 minutes (CP). The CV and CP steps were repeated for 20 times as a loop. **(b)** Cyclic voltammograms of $Co(OH)_x$ and Co_3O_4 anodes in the cell at 50th-cycle-CV for each loop cycle. **(c)** The cell voltage of $Co(OH)_x$ and Co_3O_4 anodes in the cell over 20 CP loop cycles.

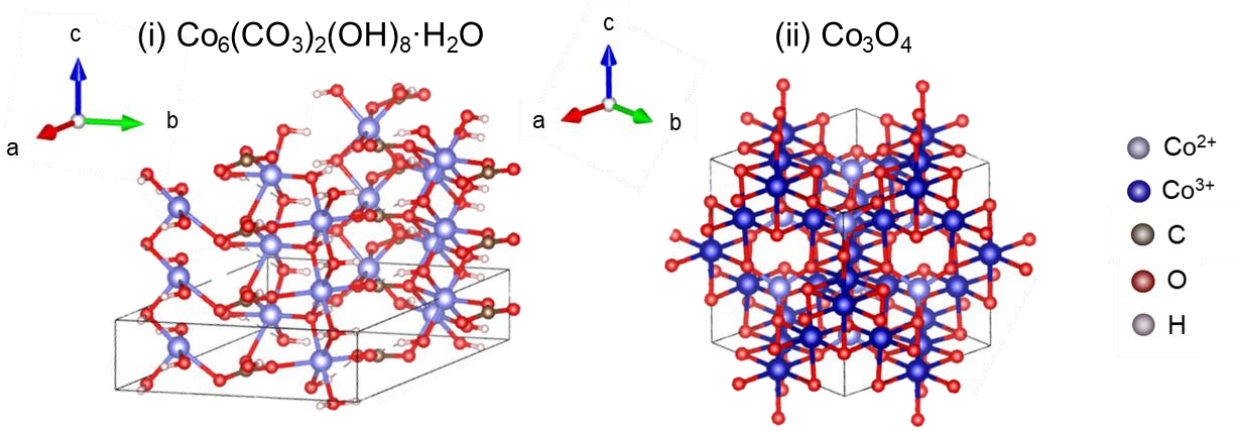

Figure A.9 Crystal structures of $Co(OH)_x$ and Co_3O_4

Crystal structures of (i) $Co_6(CO_3)_2(OH)_8 \cdot H_2O$ (namely, $Co(OH)_x$) and (ii) Co_3O_4 visualized using a software VESTA.[1] The structure of $Co(OH)_x$ was optimized following literature.[2]

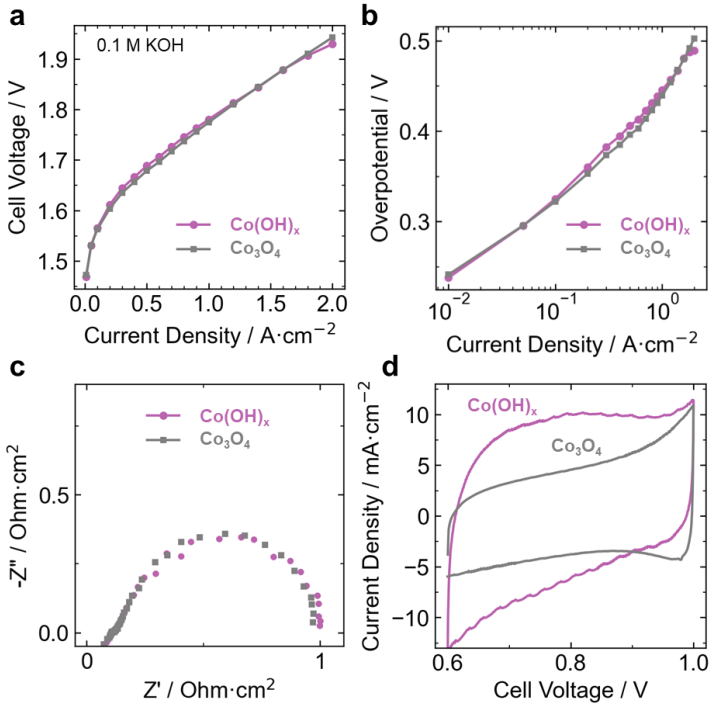

Figure A.10 Performance comparison of $Co(OH)_x$ and Co_3O_4 in KOH-fed AEMWE devices

(a) Polarization curves of AEMWE cells at 56 °C with a self-supported $Co(OH)_x$ and Co_3O_4 on PTL with 0.1 M KOH feed. **(b)** Plot of *iR-corrected* overpotential vs. current density in logarithm scale of AEMWE cells. **(c)** EIS curves at a current density of 50 mA·cm^{-2} applied and **(d)** cyclic voltammograms at a scan rate of 100 mV·s^{-1} with a sweeping range of 0.6 to 1 V of individual samples in AEMWE cells.

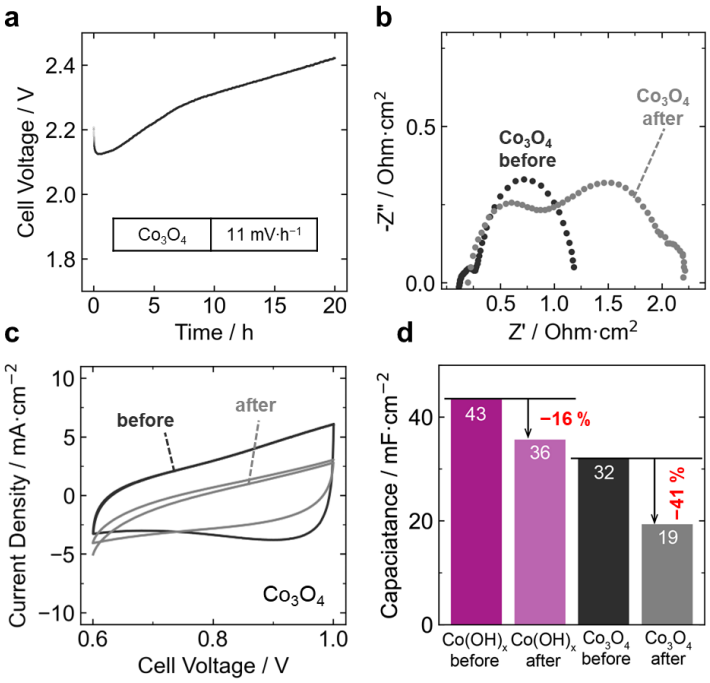

Figure A.11. Durability of Co_3O_4 in AEMWE devices

(a) Durability of Co_3O_4 anode in pure water-fed AEMWE cells held at 1 $A \cdot cm^{-2}$ at 56 °C. Inset table shows the voltage degradation rates calculated from last 10 hours of cell operation. Corresponding **(b)** EIS before and after the durability test. **(c)** Cyclic voltammograms of $Co(OH)_x$ anode before and after the durability test. **(d)** Bar graph of capacitances before and after the durability test. The capacitance values for $Co(OH)_x$ were obtained from CV scans in Figure 2.6b ("Pure water" mode).

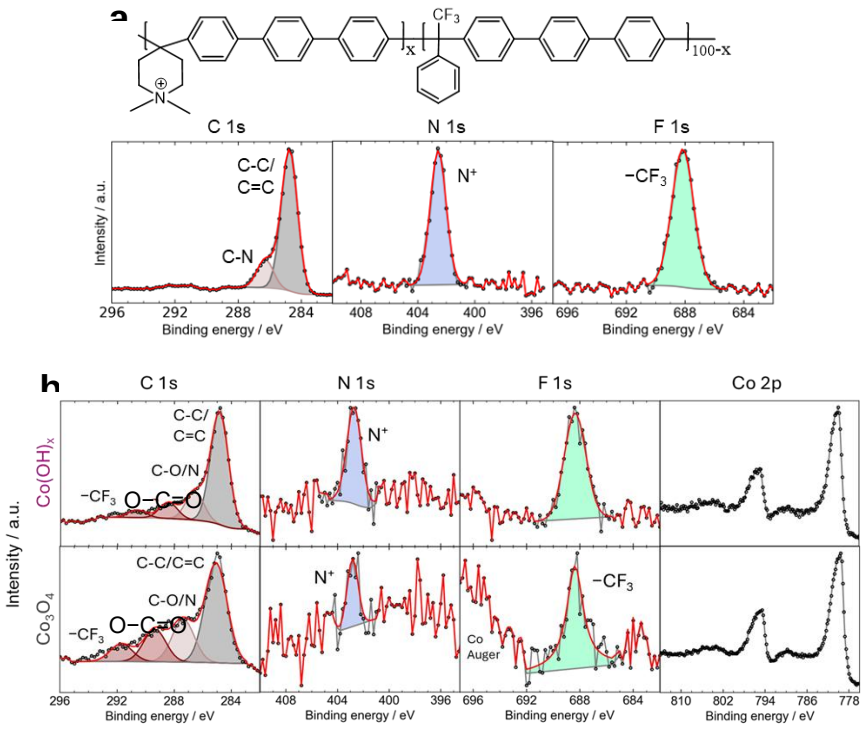

Figure A.12 XPS analysis of operated $Co(OH)_x$ and Co_3O_4 anodes

(a) Chemical structure of PiperION and its XP spectra of C 1s, N 1s, F 1s as a topcoat on the anode before the cell operation. **(b)** XP spectra of C 1s, N 1s, F 1s, and Co 2p of $Co(OH)_x$ and Co_3O_4 anodes after the durability test (1 $A \cdot cm^{-2}$ for 20 h). Ionomer oxidation was observed for both samples.

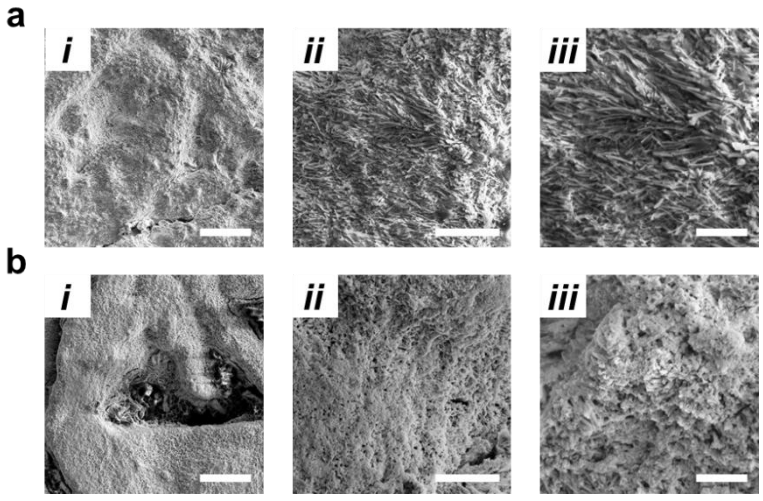

Figure A.13 SEM images of operated $Co(OH)_x$ and Co_3O_4 anodes

SEM images of **(a)** $Co(OH)_x$ and **(b)** Co_3O_4 anodes after the durability test (1 $A \cdot cm^{-2}$ for 20 h). Scale bars are set as (i) 20 μm, (ii) 5 μm, and (iii) 2 μm for each panel.

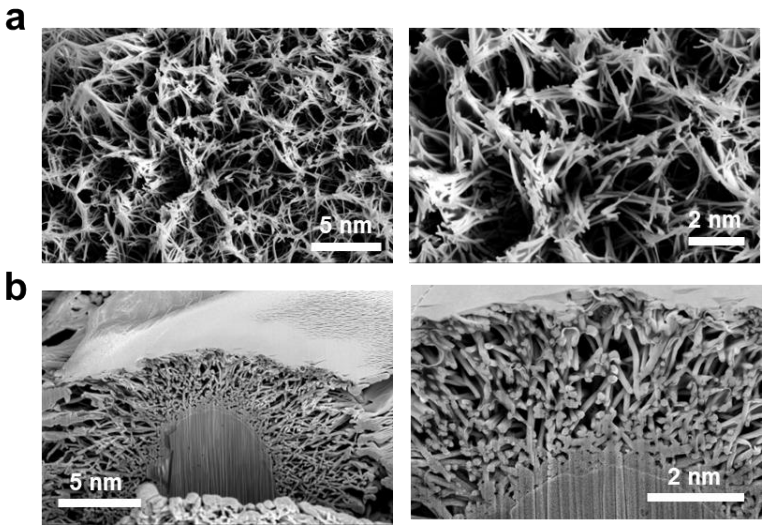

Figure A.14 SEM images of Co_3O_4 anode with lower ionomer loading

SEM images of **(a)** Co_3O_4 on Ni alloy PTL with an ionomer loading of 0.1 mg·cm^{-2} and **(b)** its cross-sectional images. Compared to Co_3O_4 with 1 mg·cm^{-2} ionomer coating in Figures S3 and S4, the sample did not show a prominent macrostructure with ionomers covering only the catalyst surfaces. This still would not provide good contact with a bulk membrane when assembled in the AEMWE device.

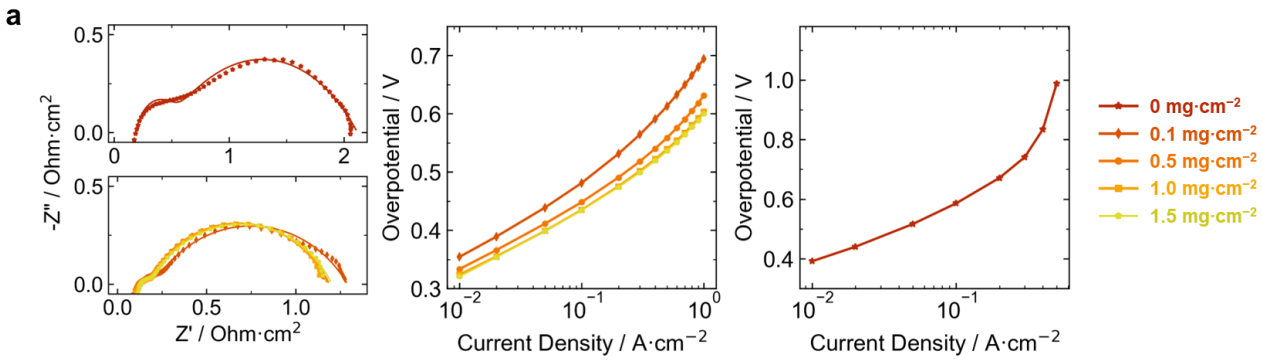

Figure A.15 Effect of ionomer loading on AEMWE devices

(a) EIS curves of pure water-fed AEMWE cells with $Co(OH)_x$ anodes with different PiperION ionomer topcoat loadings. **(b)** and **(c)** Plots of *iR-corrected* overpotential vs. current density in logarithm scale of the same anodes.

Table A.2 EIS fit results of ionomer loading dependence

Ionomer loading	R_{Ohm} ($\Omega \cdot cm^2$)	R_{CT1} ($\Omega \cdot cm^2$)	Q_{CPE1} ($F \cdot s^{\alpha-1}$)	α_1	R_{CT2} ($\Omega \cdot cm^2$)	Q_{CPE2} ($F \cdot s^{\alpha-1}$)	α_2	Total R_{CT} ($\Omega \cdot cm^2$)
0 $mg \cdot cm^{-2}$	0.189	1.651	0.032	0.54	0.276	$9 \cdot 10^{-5}$	0.92	1.927
0.1 $mg \cdot cm^{-2}$	0.128	1.081	0.059	0.64	0.081	0.001	0.88	1.162
0.5 $mg \cdot cm^{-2}$	0.113	1.018	0.084	0.70	0.057	0.003	0.82	1.075
1.0 $mg \cdot cm^{-2}$	0.129	0.998	0.101	0.71	0.052	0.007	0.77	1.050
1.5 $mg \cdot cm^{-2}$	0.130	1.018	0.114	0.69	0.054	0.004	0.85	1.072

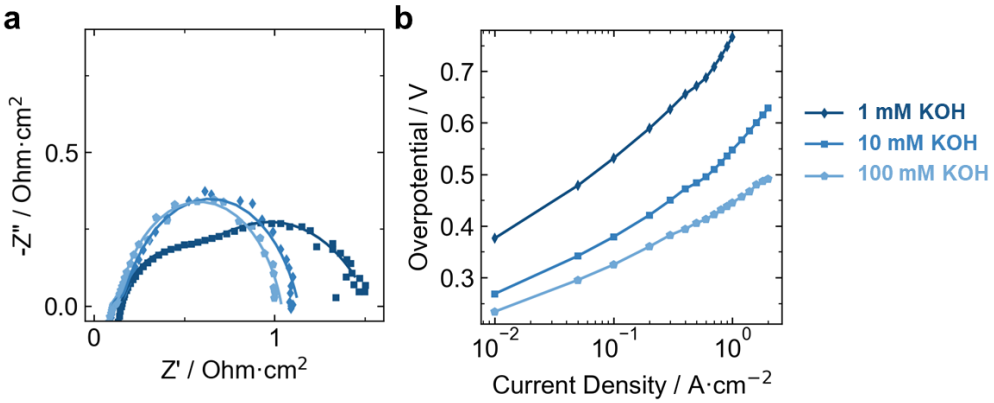

Figure A.16 Effect of KOH concentration on AEMWE devices

(a) EIS curves of AEMWE cells with *ionomer-free* $Co(OH)_x$ anodes with different concentration of KOH feed. **(b)** Plot of *iR-corrected* overpotential vs. current density in logarithm scale of the same anodes.

Table A.3 EIS fit results of KOH concentration dependence

KOH concentration	R_{Ohm} ($\Omega \cdot cm^2$)	R_{CT1} ($\Omega \cdot cm^2$)	Q_{CPE1} ($F \cdot s^{\alpha-1}$)	α_1	R_{CT2} ($\Omega \cdot cm^2$)	Q_{CPE2} ($F \cdot s^{\alpha-1}$)	α_2	Total R_{CT} ($\Omega \cdot cm^2$)
1 mM	0.146	1.033	0.044	0.60	0.350	0.002	0.75	1.383
10 mM	0.105	0.973	0.052	0.79	0.054	0.007	0.79	1.027
100 mM	0.105	0.904	0.129	0.82	0.028	0.074	0.68	0.932

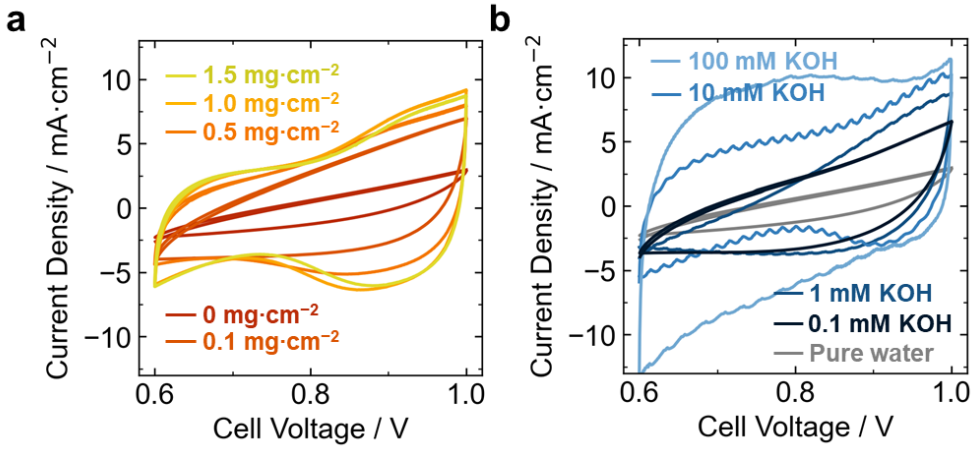

Figure A.17 ECSA estimation for with different ionomer loadings and KOH concentrations

Cyclic voltammograms of **(a)** *ionomer-coated* $Co(OH)_x$ anodes in pure water-fed AEMWE cells and **(b)** *ionomer-free* $Co(OH)_x$ anodes in AEMWE cells with different concentration of KOH feed at a scan rate of 100 $mV \cdot s^{-1}$.

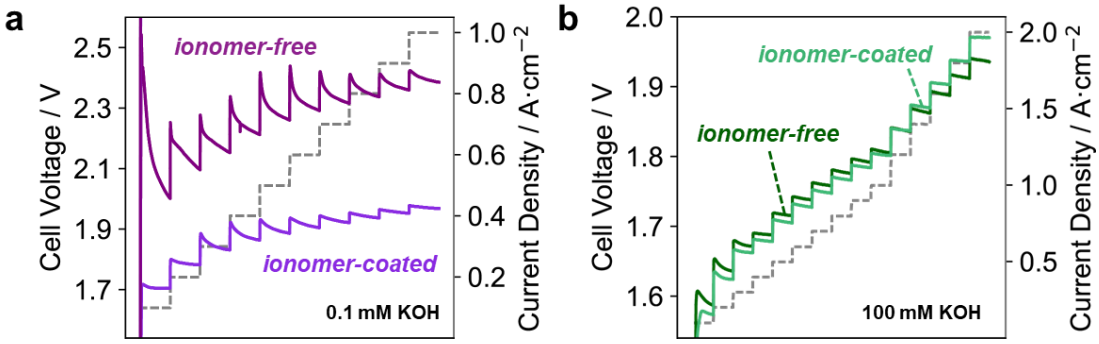

Figure A.18 Catalyst activation in AEMWE devices with KOH supporting electrolytes

(a) Break-in j-V curves of 0.1 mM KOH-fed AEMWE cells at 56 °C of $Co(OH)_x$ anodes with and without ionomer topcoat. **(b)** Break-in j-V curves of 100 mM KOH-fed AEMWE cells at 56 °C of $Co(OH)_x$ anodes with and without ionomer topcoat.

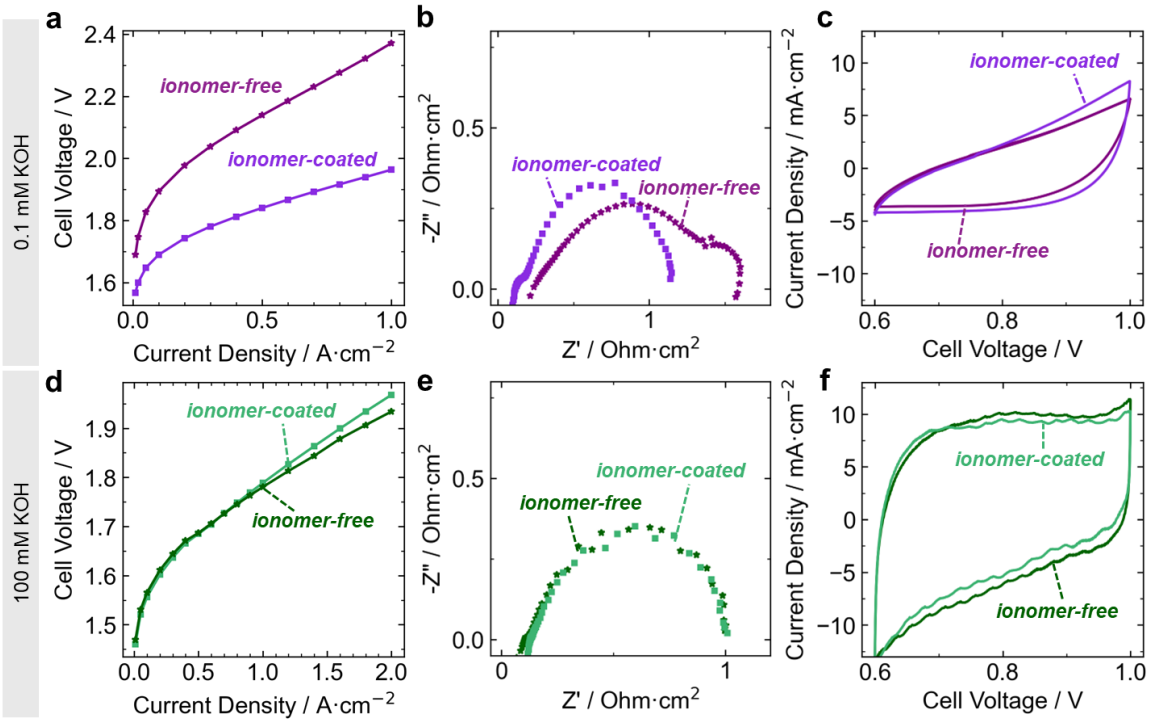

Figure A.19 AEMWE performance of ionomer-free and ionomer-coated anodes

(a) Polarization curves of 0.1 mM fed-AEMWE cells at 56 °C with $Co(OH)_x$ anodes with and without ionomer topcoat. Corresponding **(b)** EIS curves at 50 mA·cm^{-2} and **(c)** cyclic voltammograms at a scan rate of 100 mV·s^{-1} with a sweeping range of 0.6 to 1 V. **(d)** Polarization curves of 100 mM fed-AEMWE cells at 56 °C with $Co(OH)_x$ anodes with and without ionomer topcoat. Corresponding **(e)** EIS curves at 50 mA·cm^{-2} and **(f)** cyclic voltammograms at a scan rate of 100 mV·s^{-1} with a sweeping range of 0.6 to 1 V.

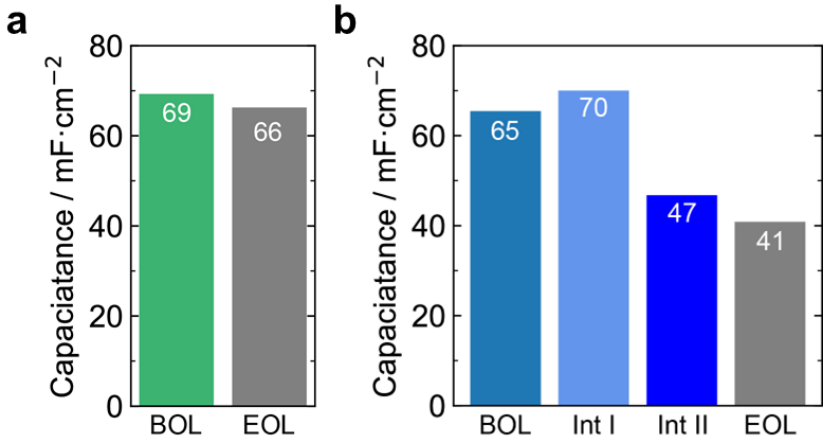

Figure A.20 Capacitance changes during AEMWE device operation

(a) The cell was operated in KOH. **(b)** The cell was initially activated with KOH, then switched to pure water.

Table A.4 EIS fit results of AEMWE device operation with various feed modes

KOH	R_{Ohm} ($\Omega \cdot cm^2$)	R_{CT1} ($\Omega \cdot cm^2$)	Q_{CPE1} ($F \cdot s^{\alpha-1}$)	α_1	R_{CT2} ($\Omega \cdot cm^2$)	Q_{CPE2} ($F \cdot s^{\alpha-1}$)	α_2	Total R_{CT} ($\Omega \cdot cm^2$)
BOL	0.127	0.809	0.115	0.87	0.076	0.480	0.61	0.885
EOL	0.091	0.919	0.188	0.86	0.049	0.516	0.50	0.968
KOH to pure water	R_{Ohm} ($\Omega \cdot cm^2$)	R_{CT1} ($\Omega \cdot cm^2$)	Q_{CPE1} ($F \cdot s^{\alpha-1}$)	α_1	R_{CT2} ($\Omega \cdot cm^2$)	Q_{CPE2} ($F \cdot s^{\alpha-1}$)	α_2	Total R_{CT} ($\Omega \cdot cm^2$)
BOL	0.129	0.833	0.106	0.87	0.106	0.963	0.44	0.939
Int I	0.094	0.907	0.109	0.88	0.080	0.796	0.54	0.987
Int II	0.097	0.976	0.090	0.80	0.028	0.018	0.77	1.004
EOL	0.101	1.188	0.084	0.61	0.104	0.002	0.92	1.292
Pure water	R_{Ohm} ($\Omega \cdot cm^2$)	R_{CT1} ($\Omega \cdot cm^2$)	Q_{CPE1} ($F \cdot s^{\alpha-1}$)	α_1	R_{CT2} ($\Omega \cdot cm^2$)	Q_{CPE2} ($F \cdot s^{\alpha-1}$)	α_2	Total R_{CT} ($\Omega \cdot cm^2$)
BOL	0.134	0.929	0.092	0.74	0.121	0.082	0.42	1.050
EOL	0.112	1.612	0.036	0.47	0.216	$1 \cdot 10^{-4}$	0.88	1.828

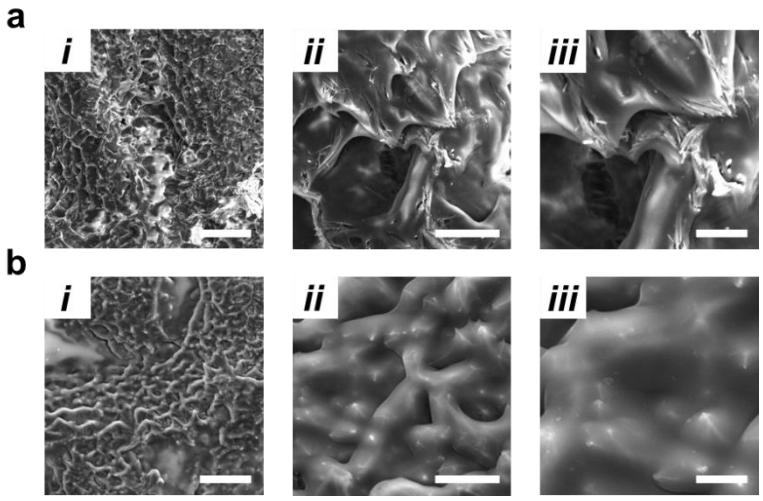

Figure A.21 SEM images of anode surfaces after cell operation

SEM images of $Co(OH)_x$ anodes after the durability test (1 $A \cdot cm^{-2}$ for 20 h) in **(a)** KOH-to-pure-water cell and **(b)** KOH only cell. Scale bars are set as (i) 20 μm, (ii) 5 μm, and (iii) 2 μm for each panel. Ionomer topcoats are still on top of the catalyst layers after cell operation and disassembly.

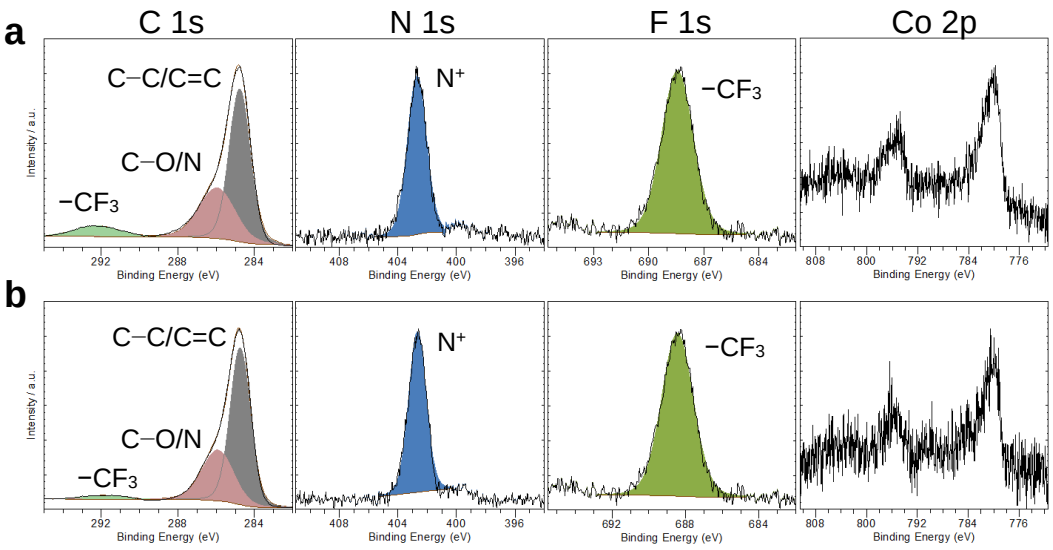

Figure A.22 SEM images of anode surfaces after cell operation

XP spectra of C 1s, N 1s, F 1s and Co 2p of $Co(OH)_x$ anodes after the durability test in **(a)** KOH-to-pure-water cell and **(b)** KOH only cell. Co 2p signals are noisy in both samples because of thick ionomer topcoats.

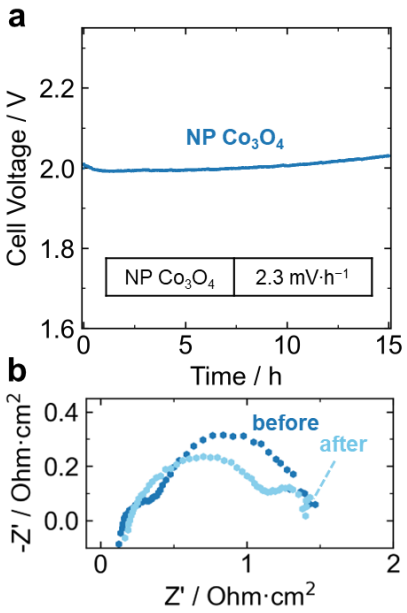

Figure A.23 Durability of NP-based anode in the AEMWE device

(a) Durability of NP Co_3O_4 anode in pure water-fed AEMWE cell at 56 °C at a constant current density of 500 mA·cm^{-2} and corresponding **(b)** EIS curves at 50 mA·cm^{-2} measured before and after the durability test.

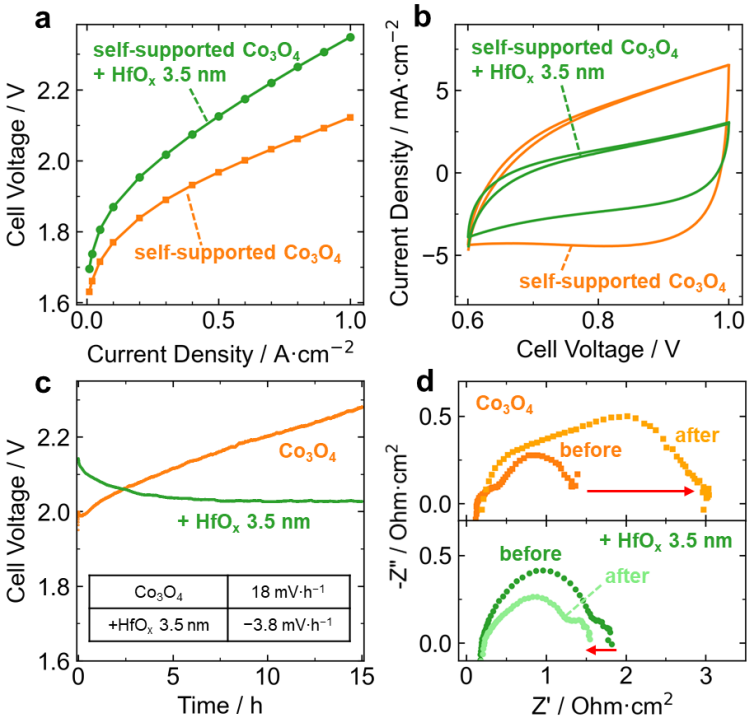

Figure A.24 Effect of HfO_x passivation layers in the AEMWE devices

(a) Polarization curves of pure water-fed AEMWE cells at 56 °C with a self-supported Co_3O_4 anode and 3.5 nm-thick-HfO_x-coated self-supported Co_3O_4 anode. Corresponding **(b)** cyclic voltammograms at a scan rate of 100 $mV \cdot s^{-1}$ with a sweeping range of 0.6 to 1 V, **(c)** durability test data at a constant current density of 500 $mA \cdot cm^{-2}$, and **(d)** EIS curves at 50 $mA \cdot cm^{-2}$ measured before and after the durability tests.

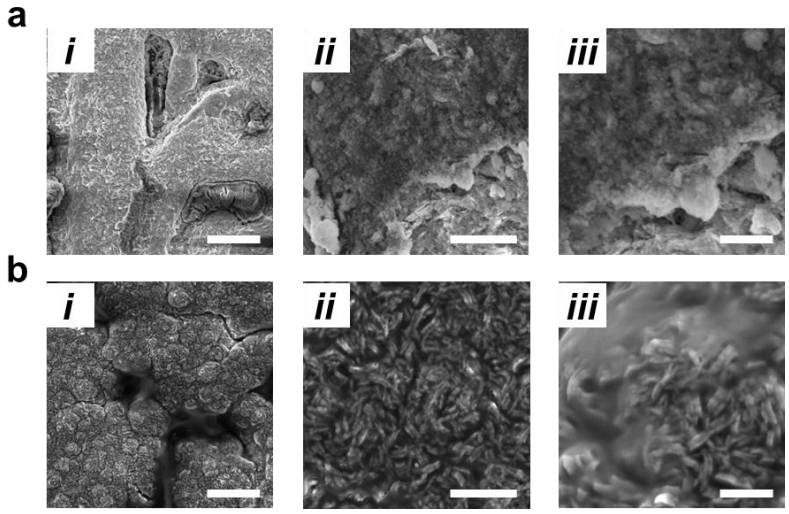

Figure A.25 HfO_x layer suppressing catalyst-ionomer degradation

SEM images of **(a)** Co_3O_4 anode and **(b)** 3.5 nm-thick-HfO_x-coated anode after the durability test (500 $mA \cdot cm^{-2}$ for 15 h). Scale bars are set as (i) 20 μm, (ii) 5 μm, and (iii) 2 μm for each panel.

REFERENCES

(1) Oqmhula, K.; Toma, T.; Maezono, R.; Hongo, K. First-Principles-Based Insight into Electrochemical Reactivity in a Cobalt-Carbonate-Hydroxide Pseudocapacitor. *ACS Omega* **2023**, *8* (7), 6743-6752.

(2) Momma, K.; Izumi, F. VESTA 3 for Three-Dimensional Visualization of Crystal, Volumetric and Morphology Data. *J. Appl. Crystallogr.* **2011**, *44* (6), 1272-1276.

APPENDIX B

CHAPTER III SUPPLEMENTARY INFORMATION

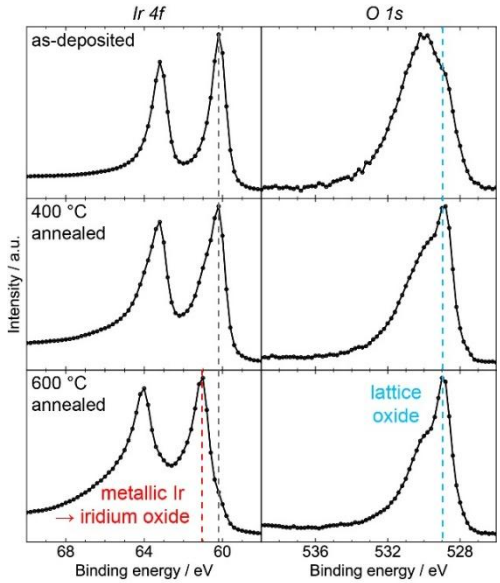

Figure B.1 XPS analysis of Ir-based anodes

Ir 4f and O 1s XP spectra of as-deposited metallic Ir on Ti/Si substrate, and 400 °C and 600 °C annealed samples showing the metallic Ir to iridium oxide transition requires high temperature.[1]

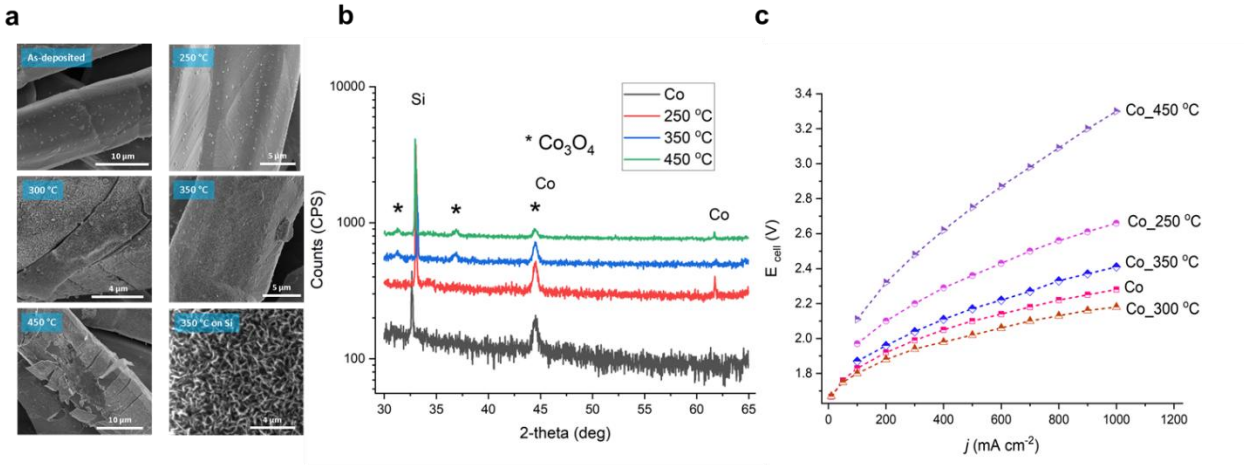

Figure B.2 Phase transformation and AEMWE cell performance of CoO_x-based anodes

(a) SEM images of as-deposited Co on SS PTL and samples annealed at different temperatures. **(b)** X-ray diffraction patterns of as-deposited Co on Ti/Si substrate and annealed samples. **(c)** Polarization curves of AEMWE single cell of metallic Co and cobalt oxide samples operated at 56 °C with pure water feed.

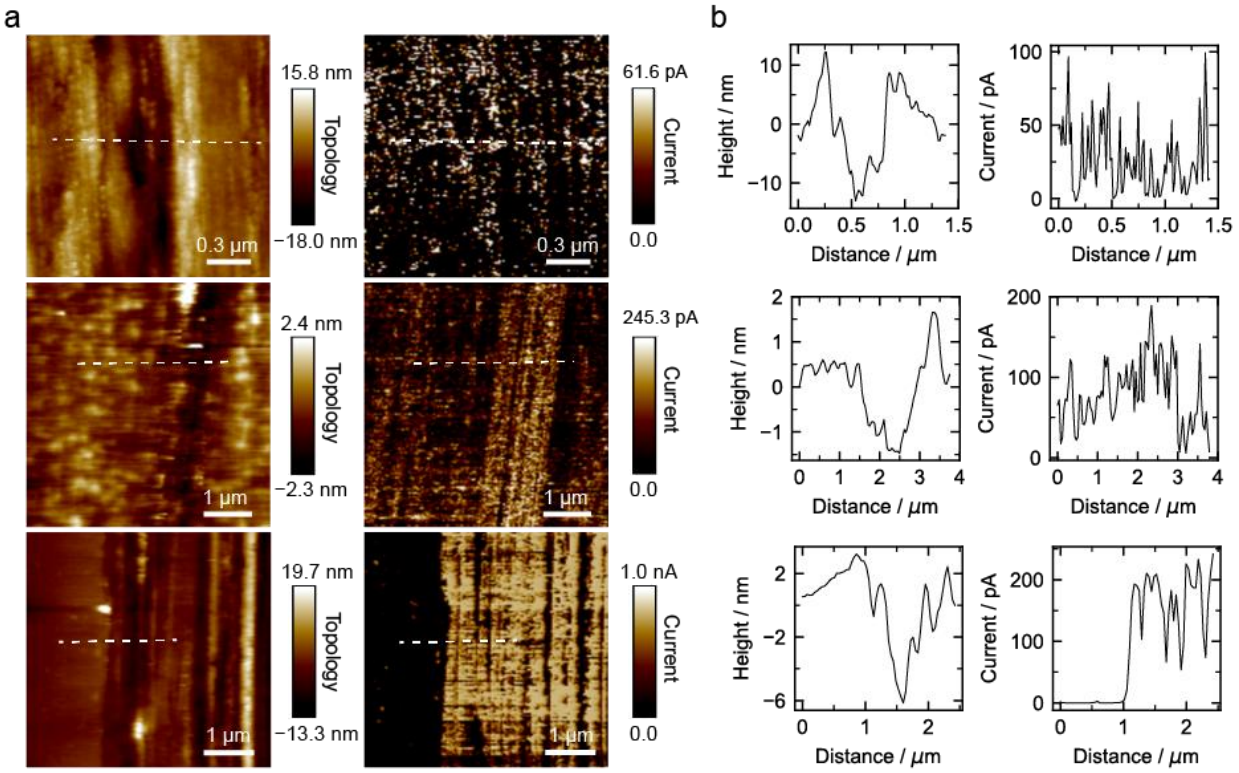

Figure B.3 AFM analysis of HfO_x coatings

(a) Height and current maps measured by c-AFM on HfO_x coatings on Pt/Ti on glass with a tip-substrate voltage bias of 1.0 V. No HfO_x coating (top), 0.8 nm HfO_x film (middle), and 3.5 nm HfO_x film (bottom). **(b)** Line scans of height and current of three samples. Without HfO_x coating, there is no dependence of height on the current at the surface, while 3.5 nm of HfO_x film shows electrically insulating behavior.

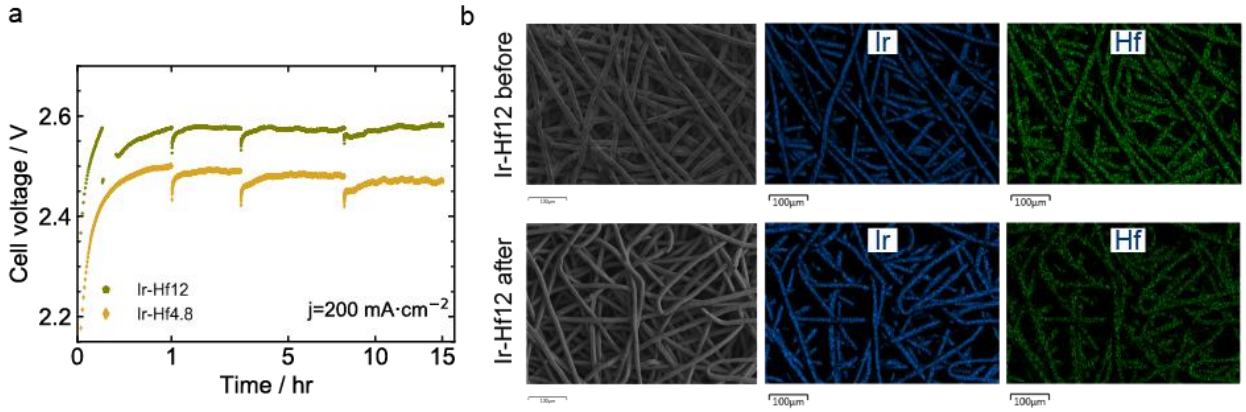

Figure B.4 Durability of HfO_x-coated Ir anodes

(a) Durability test of Ir-Hf4.8 and Ir-Hf12 samples with a current density of 200 $mA \cdot cm^{-2}$ applied at 56 °C with pure water feed. **(b)** SEM images and EDS maps of Ir-Hf12 sample before and after the durability test.

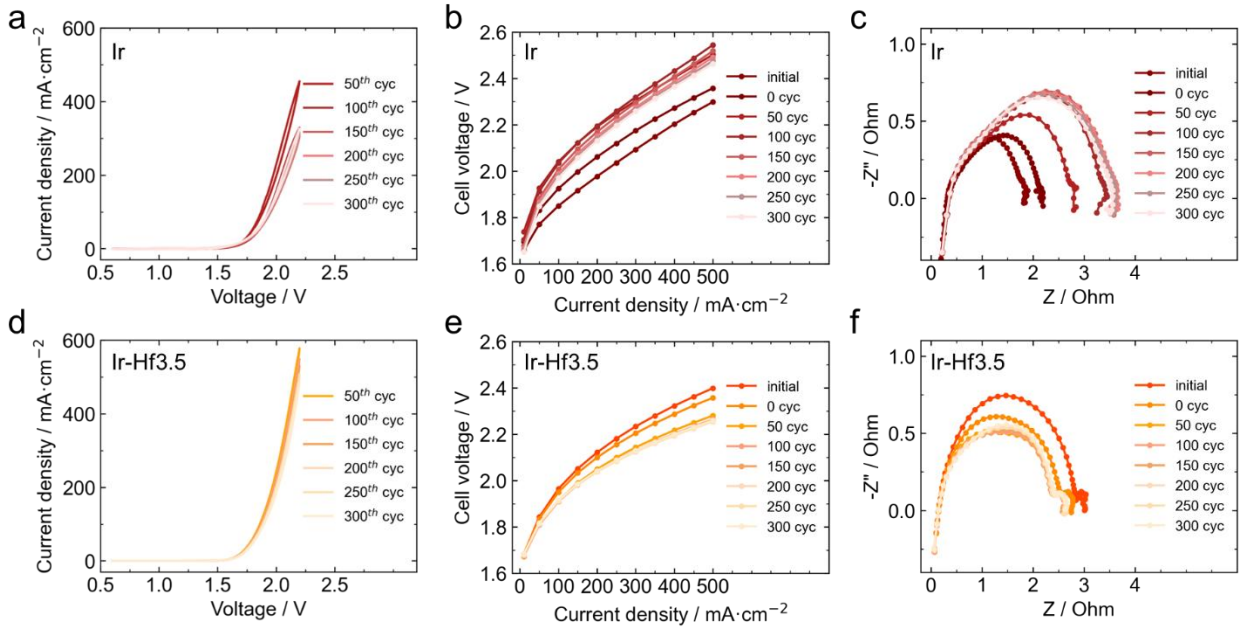

Figure B.5 Cyclic stability of Ir-based anodes

(a) Two-electrode cyclic voltammograms for the unpassivated Ir-anode AEMWE showing rapid degradation along with **(b)** associated polarization curves and **(c)** corresponding EIS curves at 50 mA·cm^{-2} and 56 °C with pure-water feed. **(d)-(f)** show the same data for the passivated Ir-Hf3.5 anode. The passivation layer in this cycling experiment is likely substantially stabilizing the interface and suppressing metal-oxide redox that may additionally contribute to interface morphological degradation on top of ionomer oxidation.

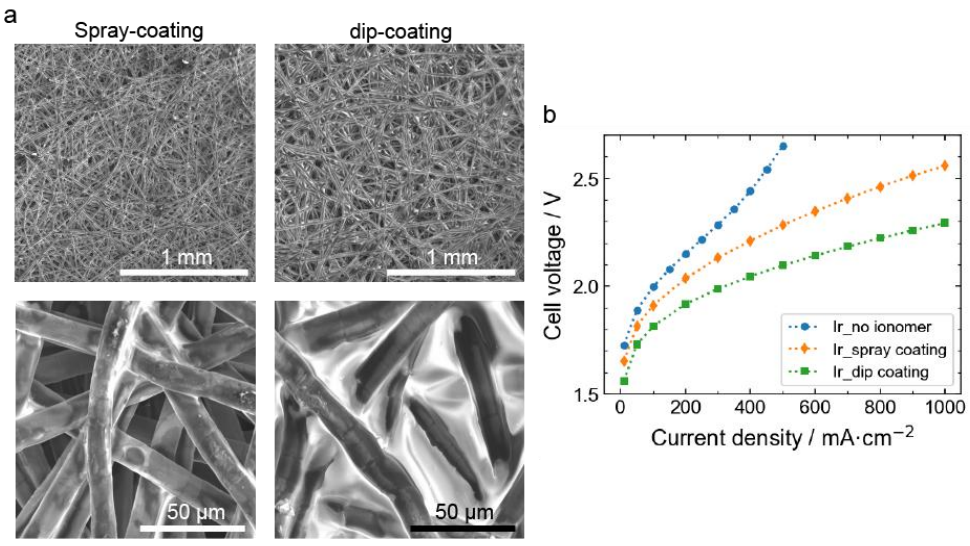

Figure B.6 Effect of ionomer coating method on cell performance

(a) SEM images of ionomer-coated stainless steel using spray-coating and dip-coating. **(b)** Polarization curves of the AEMWE cell using Ir-based PTLs with ionomer topcoats prepared with

different methods. The polarization curves indicate that dip-coated Ir electrode outperformed the spray-coated one as the ionomer loading was higher and ionomer smeared through pores of SS, likely improving the catalyst utilization. The cells were operated at 56 °C with pure-water feed.

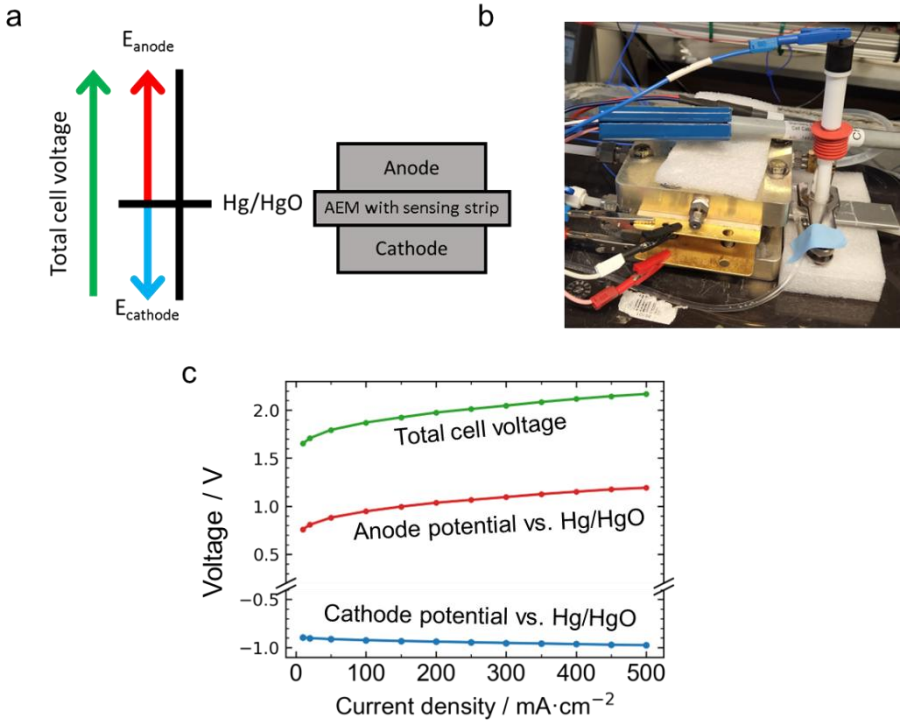

Figure B.7 Demonstration of membrane-sensing system

(a) Scheme of a membrane-sensing system coupled with AEMWE cell. The left potential diagram explains the total cell voltage, anode, cathode, and reference electrode potentials. **(b)** Picture of AEMWE single cell with the membrane sensing setup. **(c)** Exemplified voltage breakdown with a Hg/HgO reference electrode.

Table B.1 Degradation rates of Ir system

Anode	Initial cell voltage (V)	Final cell voltage (V)	Anode potential vs Hg/HgO (V)	Cathode potential vs Hg/HgO (V)	Cell voltage degradation rate (mV·h^{-1})	Anodic voltage degradation rate (mV·h^{-1})
Ir	2.17	2.53	1.56	−0.97	2.03	1.68
Ir-Hf0.8	2.22	2.43	1.43	−1.00	2.82	2.28
Ir-Hf3.5	2.33	2.37	1.38	−0.99	1.95	1.86

Table B.2 Degradation of CoO_x system

Anode	Initial cell voltage (V)	Final cell voltage (V)	Anode potential vs Hg/HgO (V)	Cathode potential vs Hg/HgO (V)	Cell voltage degradation rate ($mV \cdot h^{-1}$)	Anodic voltage degradation rate ($mV \cdot h^{-1}$)
CoO_x	2.18	2.15	1.13	−1.02	1.10	1.67
CoO_x-Hf0.6	2.31	2.29	1.29	−1.00	0.51	1.50
CoO_x-Hf1.1	2.52	2.40	1.40	−1.0	0.60	1.00
CoO_x-Hf2.5	2.66	2.47	1.49	−0.98	0.53	0.65
CoO_x-Hf4.5	3.06	2.58	1.56	−1.02	1.27	2.20

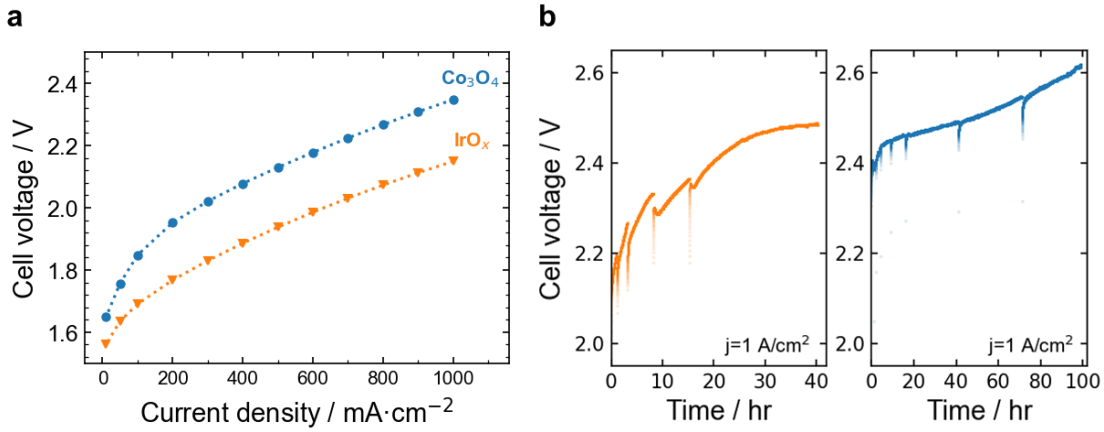

Figure B.8 AEMWE performance and durability of NP-based anodes

(a) Polarization curves of AEMWE cells with IrO_x NP/PiperION PTL and Co_3O_4 NP/PiperION PTL and **(b)** durability test with a current density of 1 $A \cdot cm^{-2}$ applied at 56 °C with pure water feed. The polarization curves show that IrO_x PTL performed better than Co_3O_4 PTL initially, with a 200 mV difference in the cell voltage at 1 $A \cdot cm^{-2}$. However, the electrical contact between Ir and ionomer facilitates the ionomer degradation while the poor conductivity of cobalt oxide leads to less ionomer degradation and corresponding slower voltage degradation during initial 40 h similar to previous reports.[2]

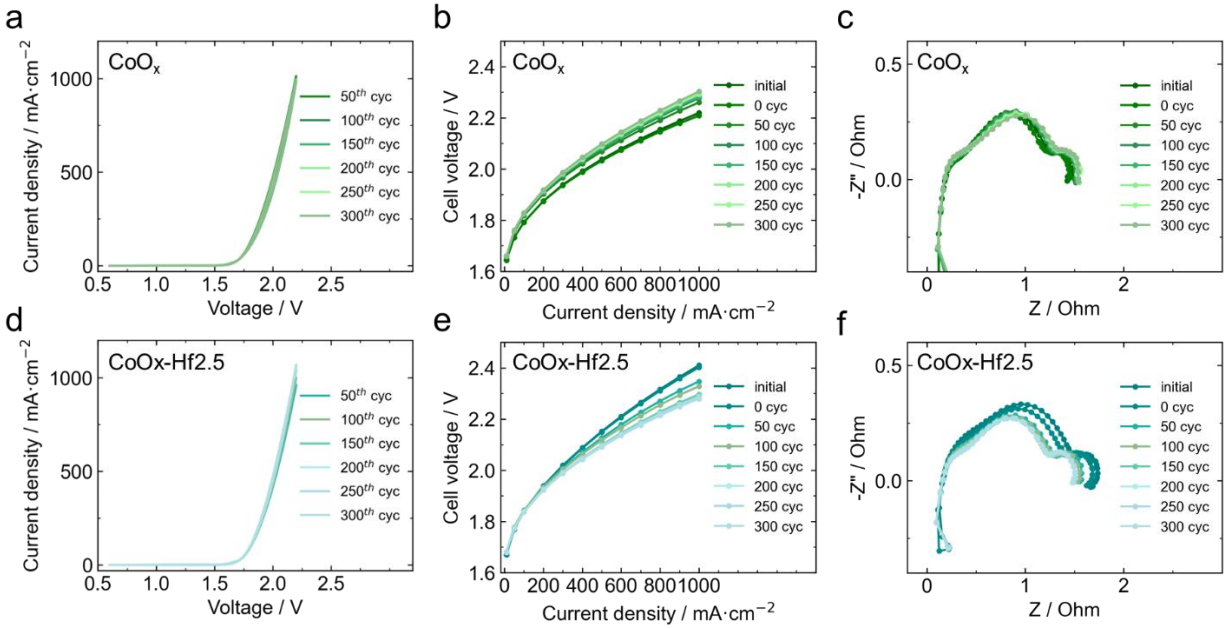

Figure B.9 Cyclic stability of CoO_x-based anodes

(a) Two-electrode cyclic voltammograms for the unpassivated CoO_x-anode AEMWE showing along with **(b)** associated polarization curves and **(c)** corresponding EIS data at 50 mA·cm^{-2} and 56 °C with pure-water feed. **(d)-(f)** show the same data for the passivated Ir-Hf3.5 anode. The passivation layer in this cycling experiment is likely stabilizing the interface and suppressing metal-oxide redox that may additionally contribute to interface morphological degradation on top of ionomer oxidation. The activation process with cycling is not fully understood.

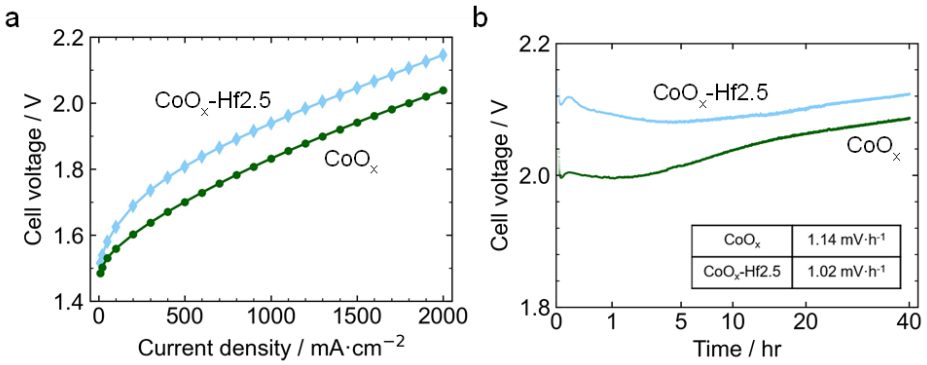

Figure B.10 AEMWE performance and durability with KOH feed

(a) Polarization curves of AEMWE cells with uncoated and HfO_x-coated CoO_x-based GDEs. **(b)** Durability test at a current density of 2 A·cm^{-2} at 75 °C with 0.10 M KOH feed. Both samples were dip-coated with ionomer (loading ~1 mg·cm^{-2}). The inset table summarizes cell voltage degradation rates from the last 20 h of the durability run. Under these conditions, it is probable that the degradation of the anode ionomer oxidation is not the only significant process. Other factors such as degradation of the cathode, membrane, catalyst, and so on, could also be contributing to the overall cell voltage degradation.

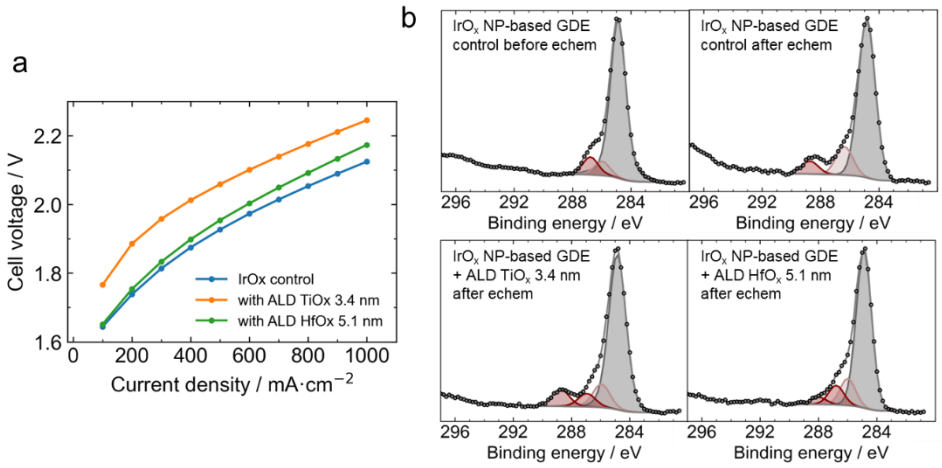

Figure B.11 Evaluating passivation coating chemistry

(a) Polarization curves of AEMWE cells with IrO_x-based electrodes with ALD TiO_x and HfO_x thin films at 56 °C using a pure-water feed. **(b)** XP spectra of C 1s of IrO_x NP-based electrode before and after constant current applied (500 $mA \cdot cm^{-2}$, 15 h) and electrodes coated with ALD TiO_x 3.4 nm and HfO_x 5.1 nm thin films after constant current is applied (500 $mA \cdot cm^{-2}$, 15 h). In this case, anodes were prepared from an ink solution without ionomer to observe the effect of the ALD coatings on ionomer degradation only with spray-coated ionomer over the catalyst layer. The TiO_x on IrO_x catalyst resulted in poor performance and XPS data showed no significant suppression of ionomer oxidation compared to the thicker HfO_x coating. This is likely due to hole conductivity through the defective TiO_x.

Table B.3 Ratios of functional groups of PiperION before and after the durability test

Anode	$C_{C=O}/C_{total}$	$N_{ammonium}/C_{total}$	F/C_{total}
Pristine PiperION	N.A.	3.76	3.46
Ir	11.36	0	0
Ir-Hf0.8	8.24	1.92	1.80
Ir-Hf3.5	0	2.73	1.44
CoO_x	12.88	1.51	2.55
CoO_x-Hf0.6	9.52	2.57	3.49
CoO_x-Hf1.1	6.82	2.32	3.25
CoO_x-Hf2.5	9.65	2.12	2.12
CoO_x-Hf4.5	6.40	2.92	3.44

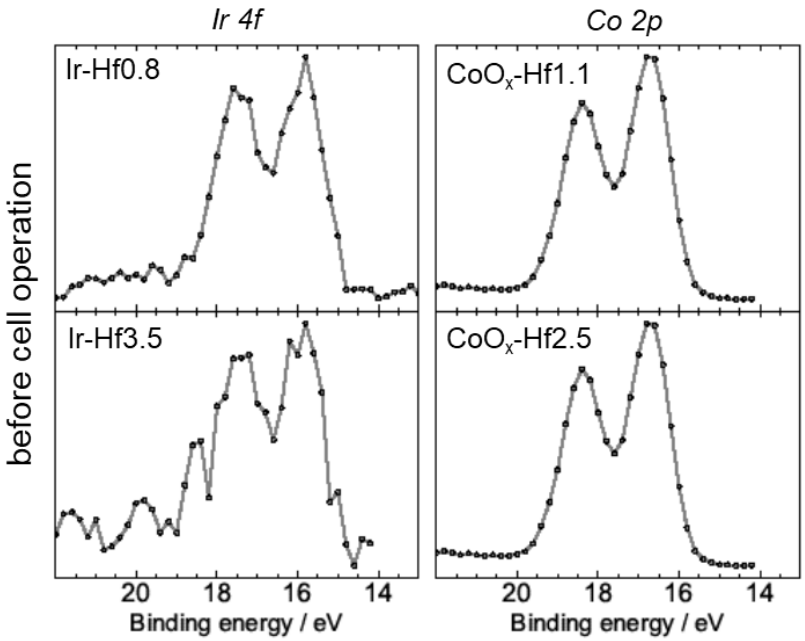

Figure B.12 XPS data of HfO_x coatings

Hf 4f XP spectra of Ir-Hf0.8, Ir-Hf3.5, CoO_x-Hf0.6, and CoO_x-Hf3.5 samples obtained before the AEMWE electrolyzer operation. CoO_x samples were measured without ionomer topcoats as those could block Hf XPS signals.

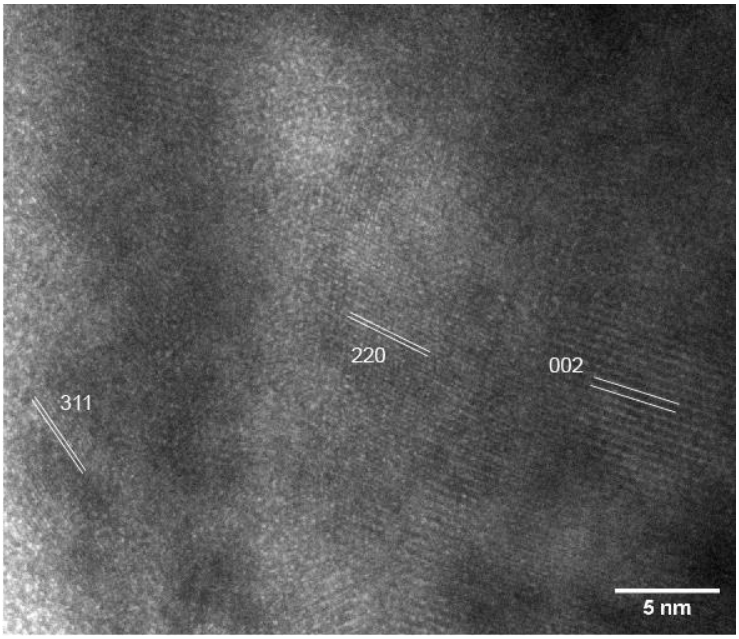

Figure B.13 TEM analysis of operated anode

TEM image showing lattice fringes of (311) and (220) planes of Co_3O_4, and (002) plane of CoO_2 obtained from CoO_x-Hf25 sample after the AEMWE electrolyzer operation.

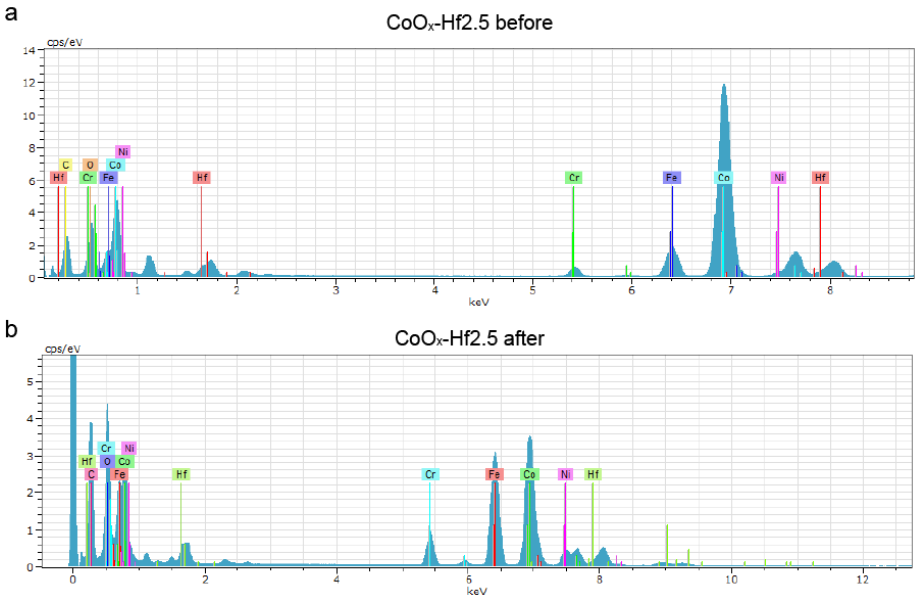

Figure B.14 Elemental analysis of HfO_x-coated CoO_x anode

EDS spectra of CoO_x-Hf2.5 sample (a) before and (b) after the AEMWE operation.

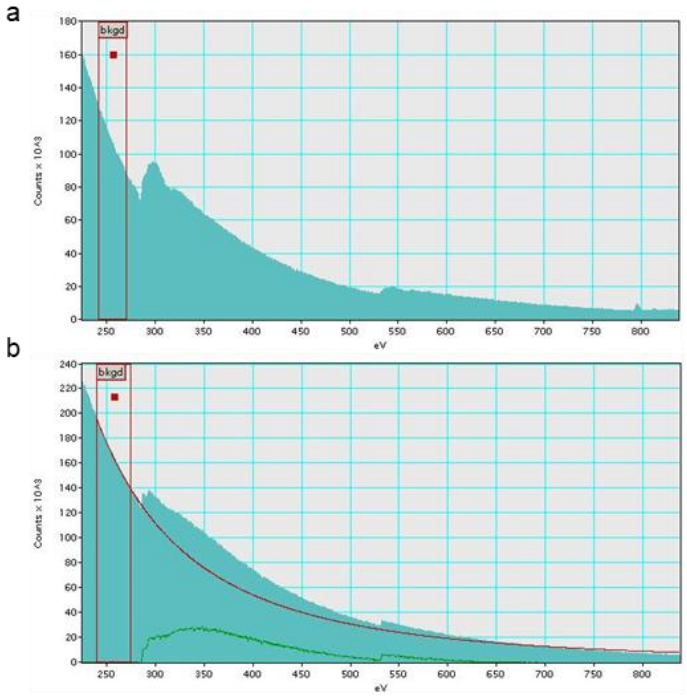

Figure B.15 EELS analysis of HfO_x-coated CoO_x anode

EELS spectra of AEMWE operated CoO_x-Hf2.5 sample of (a) region of PiperION (marked in Figure 6d) and (b) region of carbon coating deposited before FIB cross sectioning (above PiperION layer)

REFERENCES

(1) Geiger, S.; Kasian, O.; Shrestha, B. R.; Mingers, A. M.; Mayrhofer, K. J. J.; Cherevko, S. Activity and Stability of Electrochemically and Thermally Treated Iridium for the Oxygen Evolution Reaction. Journal of The Electrochemical Society 2016, 163 (11), F3132-F3138.

(2) Krivina, R. A.; Lindquist, G. A.; Beaudoin, S. R.; Stovall, T. N.; Thompson, W. L.; Twight, L. P.; Marsh, D.; Grzyb, J.; Fabrizio, K.; Hutchison, J. E.; et al. Anode Catalysts in Anion-Exchange-Membrane Electrolysis without Supporting Electrolyte: Conductivity, Dynamics, and Ionomer Degradation. *Adv. Mater.* **2022**, *34* (35).

APPENDIX C

CHAPTER IV SUPPLEMENTARY INFORMATION

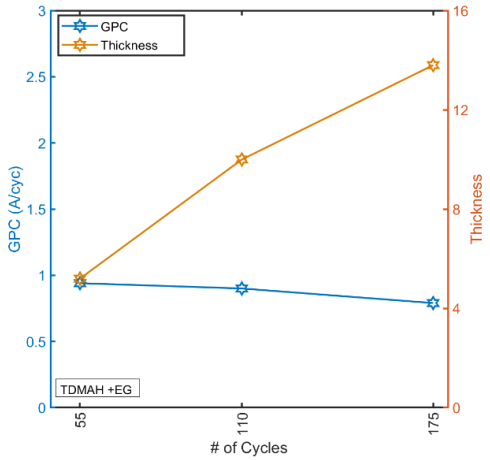

Figure C.1 Growth of Hf(EG) coatings on Si wafer

The growth rate per cycle was calculated as 0.78-0.94 Å per cycle using spectroscopic ellipsometry.

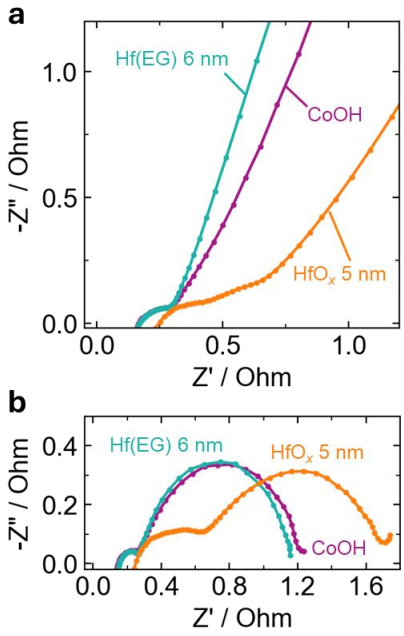

Figure C.2 Electrochemical impedance analysis of ALD and MLD coated anodes

(a) Potentio electrochemical impedance spectra obtained at 1.25 V in AEMWE cells with ALD and MLD coatings. The slope of HfO_x-coated anode is close to 45° compared to other anodes at low frequency region, which indicates that hydroxide transport to the catalyst surface is limited by

the interfacing compact HfO_x layer. **(b)** Galvano electrochemical impedance spectra obtained at 50 $mA \cdot cm^{-2}$ of same anodes in the cells. While adding 6 nm of Hf(EG) didn't affect either R_{ohm} and R_{CT}, the addition of 5 nm of HfO_x led to substantial deterioration in both. Lines are incorporated as visual guides and not fit with an equivalent circuit

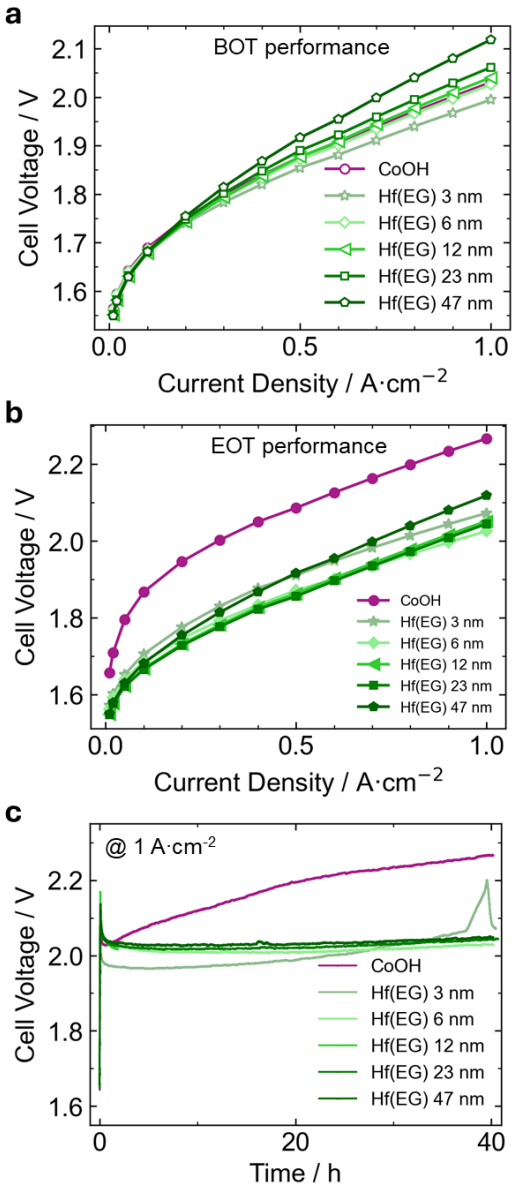

Figure C.3 Performance and durability of Co-based anodes with Hf(EG) coatings

Polarization curves of AEMWE cells with Hf(EG)-coated $Co(OH)_x$ anodes at **(a)** the beginning of the test **(b)** end of the test at the cell temperature of 56 °C with pure-water feed. **(c)** Durability test at 1 $A \cdot cm^{-2}$ applied for 40 h. The spike on the curve of Hf(EG) 3 nm was from the temperature control failure and was back to its transient voltage when the temperature was controlled back.

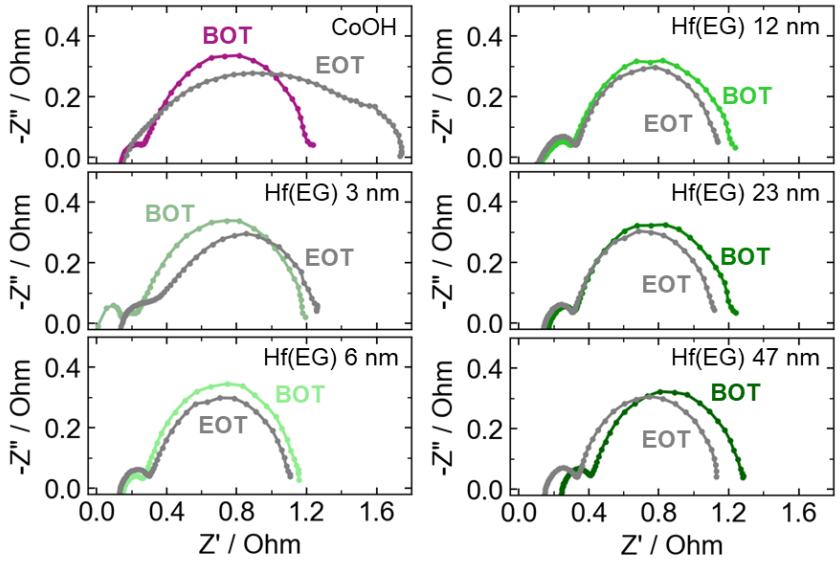

Figure C.4 GEIS analysis: investigating the impact of Hf(EG) coatings before and after the cell operation

GEIS comparisons at BOT and EOT of Co-based anodes with Hf(EG) coatings (50 mA·cm^{-2}). Lines are incorporated as visual guides and not fit with an equivalent circuit. The Co(OH)$_x$ anode showed significant degradation in total charge transfer resistance (R_{CT}) at the end of the test, while Hf(EG) coated anodes had improvements in R_{CT} in general.

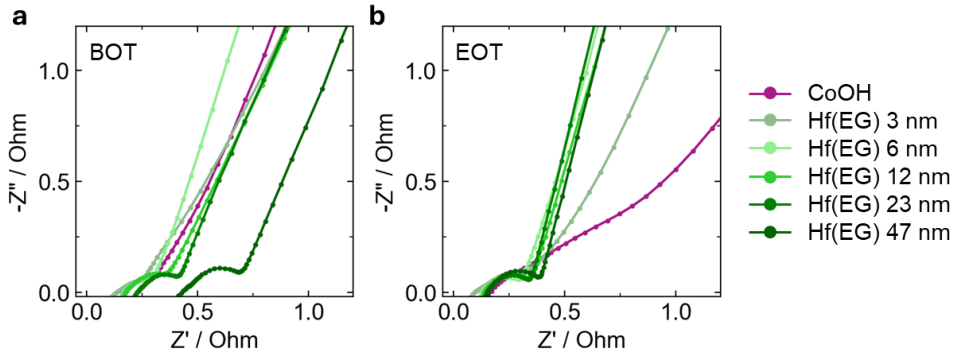

Figure C.5 PEIS analysis: investigating the impact of Hf(EG) coatings before and after the cell operation

PEIS comparisons at BOT and EOT of Co-based anodes with Hf(EG) coatings (1.25 V). Lines are incorporated as visual guides and not fit with an equivalent circuit. After 40 h of durability test, Co(OH)$_x$ anode showed larger electronic catalyst layer resistance (extension of knee size at high frequency region) along with limited ionic transport behavior at lower frequency region.

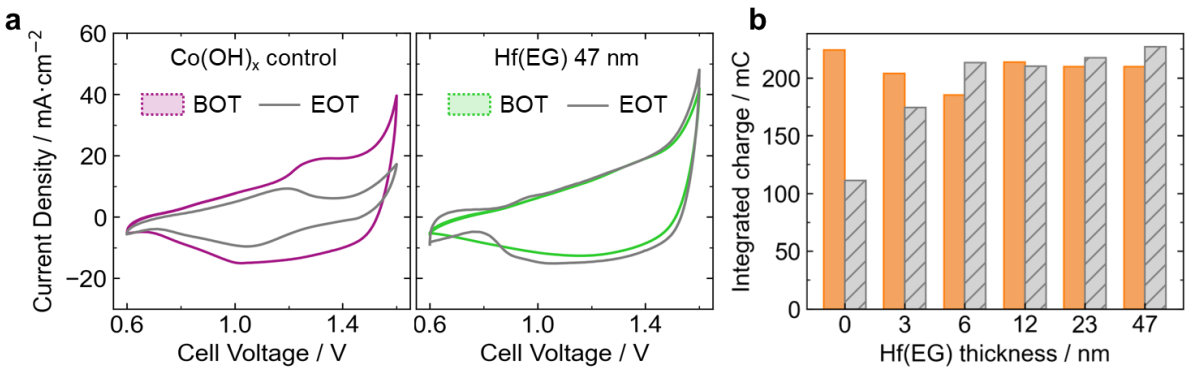

Figure C.6 CV analysis: investigating the impact of Hf(EG) coatings before and after the cell operation

Estimation of electroactive surface areas using a cyclic voltammetry technique. (a) CV of $Co(OH)_x$ control anode and 47-nm-thick-Hf(EG)-coated anode at the BOT and EOT. While the (pseudo)capacitive currents decreased for $Co(OH)_x$ after the durability test, Hf(EG) coated anode retained the currents. (b) Integrated charges of anodes with different Hf(EG) coatings at the BOT (orange color) and EOT (grey color with dashed fill).

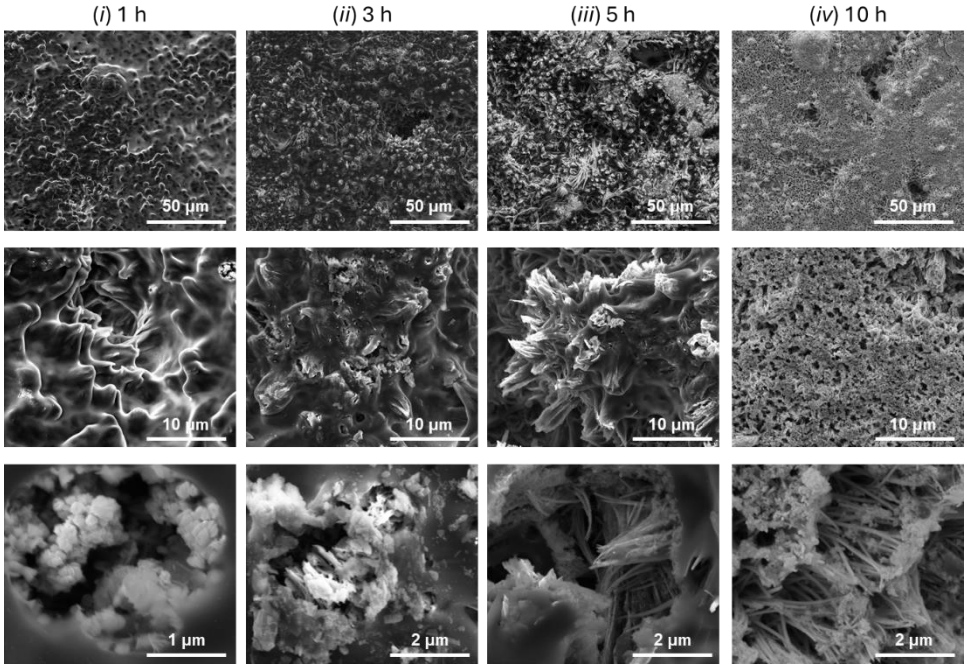

Figure C.7 Time-dependent degradation of $Co(OH)_x$ catalyst and ionomer in AEMWE devices

SEM images of $Co(OH)_x$ anodes operated at 2 $A \cdot cm^{-2}$ in AEMWE devices at 70 °C with pure-water feed for 1, 3, 5, and 10 hours. As the cell operation proceeded, $Co(OH)_x$ catalyst reconstructed to layered structured $CoO_x(OH)_y$ and fragmented, while ionomer topcoat were oxidized and removed from the catalyst surface.

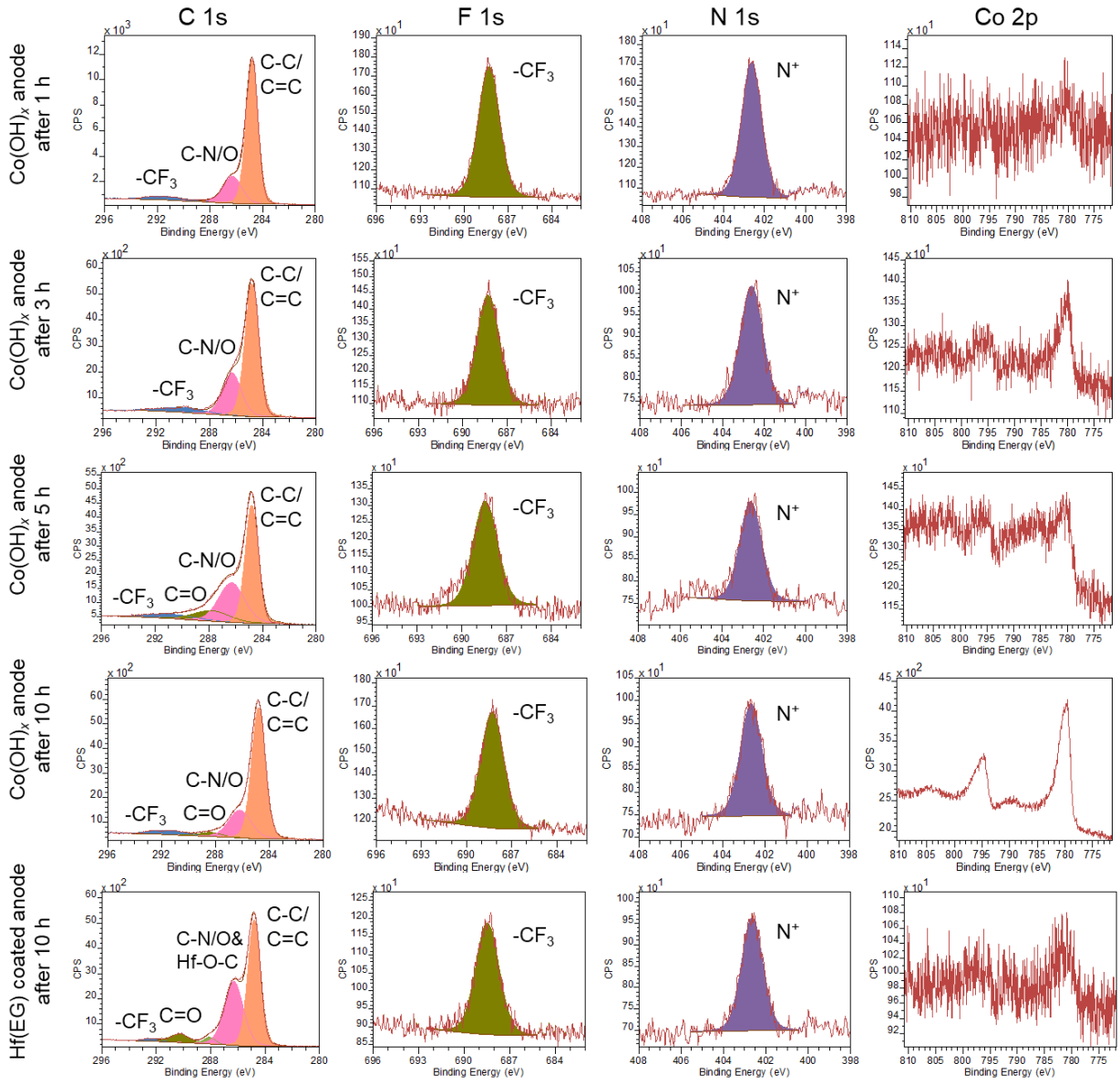

Figure C.8 XPS analysis of operated anodes

XP spectra of $Co(OH)_x$ anodes with and without 47 nm Hf(EG) coatings after the device operation. For Co(OH)x anodes, as the operation time increases, more intense Co 2p peaks appear, which is consistent with SEM analysis in Figure C.7. The chemical structure of PiperION is the same as that shown in Figure 3.5 and Figure A.12.

Table C.1 Summarized table of AEMWE degradation metrics

	$Co(OH)_x$				Hf(EG) 47 nm
AEMWE cell operation time	1 h	3 h	5 h	10 h	10 h
% change of cell voltage @ $2A \cdot cm^{-2}$	+4.3	+6.6	+7.3	+16	−2.2
% change of integrated charge	−12	−19	−26	−42	+4.9
% change of high frequence resistance	+4.3	+19	+30	+10	−22
Degradation rate ($mV \cdot h^{-1}$)	31	23	20	28	−7